



Universiteit
Antwerpen

Faculteit Farmaceutische, Biomedische en Diergeneeskundige
Wetenschappen

Departement Biomedische Wetenschappen

Dynamics of neuronal responses in silico and in vitro

De dynamische respons van neuronen in silico en in vitro

Proefschrift voorgelegd tot het behalen van de graad van doctor in de
biomedische wetenschappen aan de universiteit van Antwerpen te
verdedigen door

Christophe VERBIST

Prof. Michele Giugliano, Prof. Alain Labro
Antwerpen, 2020

Table of contents

Abbreviations	9
Samenvatting.....	11
Summary	17
CHAPTER 1: Introduction	21
1.1 The Axon Initial Segment.....	24
1.2 Theories about the “temporal sharpness” of AP generation.....	27
1.2.1 Cooperative Sodium channels	28
1.2.2 Active backpropagation.....	29
1.2.3 The critical resistive coupling theory	29
1.3 The morphological location of the AIS	30
1.4 The neuronal models of the Blue Brain Project.....	31
1.5 NEURON simulator.....	34
1.6 The Julia programming language	36
1.7 The <i>transfer function</i> of a neuron	37
1.8 References.....	43
CHAPTER 2: Research goals	55
2.1 What are the cellular correlates of IQ?	56
2.2 What influences the information capabilities of excitatory neurons? 56	
2.3 How do diverse layer 1 inhibitory neurons transfer information?..	57
CHAPTER 3: Large and fast human pyramidal neurons associate with intelligence.....	59
3.1 Chapter information.....	60
3.1.1 Publication.....	60
3.1.2 Author contribution	60
3.2 Abstract.....	61
3.3 Introduction.....	61
3.4 Results.....	66

3.4.1	IQ scores positively correlate with cortical thickness of the temporal lobe	66
3.4.2	IQ scores positively correlate with dendritic structure of temporal cortical pyramidal neurons	67
3.4.3	Larger dendrites lead to faster AP onset and improved encoding properties	69
3.4.4	Higher IQ scores associate with faster Aps.....	74
3.5	Discussion.....	78
3.6	Materials and methods	82
3.6.1	Human subjects and brain tissue	82
3.6.2	IQ scores.....	82
3.6.3	MRI data and cortical thickness estimation	83
3.6.4	Slice preparation.....	83
3.6.5	Electrophysiological recordings	84
3.6.6	Morphological analysis	84
3.6.7	NEURON modelling.....	85
3.6.8	Action Potential waveform analysis of electrophysiological recordings	87
3.6.9	Statistical analysis	88
3.7	Acknowledgements.....	88
3.8	Ethics	88
3.9	References.....	90
CHAPTER 4: The location of the axon initial segment affects the bandwidth of spike initiation dynamics		97
4.1	Chapter information.....	98
4.1.1	Publication.....	98
4.1.2	Author contribution	98
4.2	Abstract.....	99
4.3	Author summary	99
4.4	Introduction.....	100
4.5	Results.....	101
4.5.1	The AIS location alters neuronal responsiveness.....	104

4.5.2	Multicompartmental neuron models	106
4.5.3	Network simulations	113
4.6	Discussion.....	119
4.7	Materials and Methods	123
4.7.1	Conductance-based model neurons	123
4.7.2	Linear Dynamical Transfer Properties: Spike-Train Analysis in the Fourier Domain	124
4.7.3	Action Potential Trajectory and Transfer Gain profile	126
4.7.4	Reduction to the Integrate-and-Fire point neuron model	126
4.7.5	Liquid State Machine: the classification task.....	127
4.8	Data availability.....	131
4.9	Acknowledgments	131
CHAPTER 5: Homogeneous and narrow bandwidth of spike initiation in rat L1 cortical interneurons		137
5.1	Chapter Information.....	138
5.1.1	Publication.....	138
5.1.2	Author contribution.....	138
5.2	Abstract.....	139
5.3	Introduction.....	140
5.4	Materials and Methods	142
5.4.1	Brain tissue slice preparation	142
5.4.2	Electrophysiology.....	142
5.4.3	Electrical phenotype identification.....	144
5.4.4	Spike-triggered average and dynamical transfer function...	146
5.4.5	Rapidness of the action potential at its onset	148
5.4.6	Computer simulations	149
5.4.7	Statistical analysis	149
5.4.8	Data availability	150
5.5	Results.....	150
5.5.1	Encoding properties of L1 interneurons.....	150
5.5.2	Electrical classes and encoding properties	152

5.5.3	Dependency of <i>cutoff</i> on the mean firing rate	153
5.5.4	Action potential rapidity at onset	156
5.5.5	Transfer at high spectral frequencies	157
5.6	Discussion.....	159
5.7	Acknowledgements.....	162
5.8	References.....	163
CHAPTER 6: Conclusion.....		169
CHAPTER 7: Scientific curriculum vitae.....		175
CHAPTER 8: Acknowledgments		179

Abbreviations

AC – Accommodating
AD – Adapting
AP – Action Potential
b – bursting (combined with AC, AD, IR, NAC, STUT)
BAS – Ball And Stick
BBP – Blue Brain Project
c – continuous (combined with AC, AD, IR, NAC, STUT)
COF – Cut-Off Frequency
d – delayed (combined with AC, AD, IR, NAC, STUT)
EIF – Exponential Integrate and Fire
EPFL - École Polytechnique Fédérale de Lausanne
HH – Hodgkin and Huxley
IF – Integrate and fire
ISI – Inter Spike Interval
IR – Irregular
LIF – Leaky Integrate and Fire
LSM – Liquid State Machine
NAC – Non-Accommodating
ODE – Ordinary Differential Equation
QIF – Quadratic Integrate and Fire
STUT – Stuttering

Samenvatting

Het brein is een complex organisme, sommige noemen het begrijpen van het brein de laatste grens. Het is het belangrijkste verwerkingscentrum van informatie in het lichaam. Bijgevolg moet het capabel zijn om een enorme hoeveelheid signalen, die constant veranderen, te verwerken. Bijvoorbeeld als we de omgeving rondom ons waarnemen, deze verandert voortdurend. Het brein bestaat uit miljarden neuronen, het zijn deze neuronen die met elkaar communiceren met behulp van elektrische signalen. Deze neuronen moeten in staat zijn om deze snel variërende informatie van onze omgeving te verwerken en door te geven.

Computationale neurowetenschappen bevindt zich op de perfecte kruising om te onderzoeken of neuronen al dan niet deze snel variërende informatie kunnen verwerken. Het geeft de onderzoeker volledige controle over elk element van het neuron. De nauwkeurigheid van de neuron modellen is van uiterst belang, mits de resultaten afgeleid van deze modellen enkel zo goed zijn als de modellen de realiteit perfect kunnen simuleren. Dit creëert een symbiotische relatie tussen computationele en experimentele neurowetenschappen. Als modellen worden onderworpen aan een nieuwe input dan moet de output vergeleken worden met die van biologische neuronen. Enkel zo kan men verzekerd zijn dat de neuron modellen nauwkeurig zijn. Als er nieuwe eigenschappen worden ontdekt in biologische neuronen dan moeten modellen in staat zijn dit te repliceren. Er zijn veel verschillende soorten modellen, in dit werk zullen we ons focussen op één bepaald type, namelijk biofysische neuron modellen.

In 2015 heeft het Blue Brain Project, dat zich bevindt aan het École Polytechnique Fédérale de Lausanne, een corticale kolom van het ratbrein *in silico* gerecreëerd. Deze kolom was volledig gedetailleerd, dit betekent dat zowel de morfologie van de neuronen als de biofysische eigenschappen accuraat worden voorgesteld in het model. De corticale kolom bestaat uit miljoenen gemodelleerde neuronen, die geconnecteerd zijn met elkaar via synapsen. Het zijn sommige van deze neuron modellen dat gebruikt zullen worden in dit werk. Deze neuronen kunnen in twee verschillende klassen worden onderverdeeld: excitatorische neuronen, dit zijn neuronen die andere neuronen hun vuurfrequentie zullen vergrootten, en inhibitorische neuronen, deze zullen de vuurfrequentie van andere neuronen verlagen. De vuurfrequentie van neuronen wordt gedefinieerd als het aantal actie potentialen binnen een bepaalde tijdsduur. We zullen verschillende neuronen van beide klasse onderzoeken.

Naast de classificatie in excitatorisch en inhibitorisch, kunnen neuronen ook nog geclassificeerd worden op basis van de respons op een gelijkstroom puls, samen met de zogenaamde FI-curves. Deze curves worden opgesteld door de vuurfrequentie te meten bij bepaalde input stromen. Er zijn 10 verschillende vuurtypes: *classical accommodating*, *classical non accommodating*, *classical stuttering*, *classical irregular*, *bursting accommodating*, *bursting non accommodating*, *bursting stuttering*, *bursting irregular*, *direct non accommodating* and *direct stuttering*. Sommige van deze vuur types worden enkel teruggevonden in inhibitorische neuronen, terwijl andere terug gevonden worden in beide, inhibitorische en excitatorische, klasse. Niettemin worden deze vuurtypes niet vaak teruggevonden in reëel biologisch gedrag van neuronen, dit omdat deze vuurtypes gecreëerd zijn door een niet biofysische input, een gelijkstroom. Terwijl het handig is om neuronen te verdelen in deze verschillende vuurtypes blijft het onduidelijk of er enig biofysische belang zit achter deze types. Dit is één van de redenen waarom wij hebben gekozen om geen gelijkstroom te gebruiken om neuronen te onderzoeken maar eerder een onregelmatige stroom, een stroom die zeer gelijkaardig is aan diegene die in een actief brein wordt terug gevonden. Deze stroom bootst de synaptische activiteit van geconnecteerde neuronen na. Wanneer een neuron met dit soort stroom wordt geïnjecteerd is de output meer biofysisch dan wanneer een gelijkstroom wordt gebruikt. Niettemin moet er een signaal aan de onregelmatige stroom worden toegevoegd om neuronen goed te kunnen classificeren. Het signaal dat wordt toegevoegd is een mathematische sinus met een bepaalde frequentie. Neuronen hebben het vermogen om de actie potentialen die ze vuren gelijk te richten met de frequentie van de sinus. Hoe goed ze dit kunnen doen voor een bepaalde frequentie bepaald de transfer sterkte van die frequentie. Uit simulatie volgt dat neuronen een laagdoorlaatfilter. Dit wil zeggen dat de neuronen lage frequenties goed zullen doorlaten tot een bepaalde frequentie. Na deze frequentie, die vaak de cutoff frequentie wordt genoemd, zullen neuronen hun actie potentialen niet meer kunnen gelijk richten met de frequentie van de sinus en dus het signaal niet meer doorgeven. Het frequentiedomein kan dus in twee regio's worden opgedeeld, een eerste regio van 0 Hz tot de cutoff frequentie en een tweede regio vanaf deze frequentie tot oneindig. In de eerste regio zal het signaal goed doorgegeven worden tussen twee neuronen, echter in de tweede regio zal het signaal sterk verzwakt worden en niet meer waarheidsgetrouw worden doorgegeven. Deze methode wordt ook wel de *transfer functie* genoemd, het geeft ons het perfecte gereedschap om te onderzoeken hoe goed een neuron informatie kan verwerken en doorgeven.

Dit werk is voornamelijk gefocust op de eigenschappen dat de exciteerbaarheid van een neuron beïnvloed. De hypothese is dat als de exciteerbaarheid van een neuron veranderd dan zal ook de capaciteit van informatie die verwerkt kan worden door het neuron veranderen. Intuïtief kan er geredeneerd worden dat als een neuron exciteerbaarder wordt dat het eenvoudiger kan reageren op snelle veranderingen in het input signaal en zo kan het neuron beter informatie verwerken. In dit werk focus ik voornamelijk op het effect dat het axon initieel segment heeft op de exciteerbaarheid en de informatie verwerkingscapaciteiten van het neuron. Het axon initieel segment is een uniek segment in de axon, het is in dit segment dat actie potentialen voor het eerst worden gegenereerd in het neuron en zo door het neuron verspreiden. In computer simulatie kan dit segment verplaatst worden doorheen de axon. Zo kan het effect van waar dat actie potentialen worden gegenereerd op zowel de exciteerbaarheid als de informatie verwerkingscapaciteit onderzocht worden. Uit onze simulaties en wiskundige theorieën kan afgeleid worden dat als het axon initieel segment, de locatie waar actie potentialen initieel gegenereerd worden, verder weg van de soma wordt geplaatst het neuron exciteerbaarder wordt en dit op wel twee manieren. De stroom die nodig is om actie potentialen te genereren wordt verlaagd. Echter belangrijker bij aanvang zijn actie potentialen scherper. De membraan spanning van het neuron zal dus sneller stijgen bij aanvang van actie potentialen. Verder linken we in dit werk de verandering in exciteerbaarheid aan de bekwaamheid van het neuron om snel variërende informatie te verwerken. Als het axon initieel segment zich verder weg van de soma bevindt, dan zal het neuron beter geschikt zijn om snel variërende informatie verwerken. Dit vertaalt zich in een grotere cutoff frequentie. Er bestaat dus een directe relatie tussen hoe exciteerbaar een neuron is, oftewel de eigenschappen van actie potentialen, tot zijn informatie verwerkingscapaciteiten. Verder wordt er in de literatuur beschreven hoe het axon initieel segment onderhevig kan zijn aan homeostatische plasticiteit, dit zorgt er voor dat het neuron zijn eigen bandbreedte kan beheersen.

Verder zullen ook netwerk modellen worden gebruikt om de invloed van de locatie van het axon initieel segment te onderzoeken op de prestatie van het netwerk terwijl het een taak uitvoert. Verscheidene, aparte, netwerken werden bevolkt met een welbepaalde afstand tussen soma en axon initieel segment, deze netwerken werden dan een simpele classificatie taak gegeven. De resultaten liggen in lijn met die van de vorige simulaties, netwerken met een grotere afstand tussen soma en axon initieel segment waren beter uitgerust om deze eenvoudige classificatie taak uit te voeren.

Als laatste werd de invloed van de grootte van de dendrieten onderzocht met betrekking tot de neuronale bandbreedte. Uit ons onderzoek blijkt dat is de grootte van de dendrieten niet alleen positief gecorreleerd met hoe snel actie potentialen stijgen bij het begin maar ook met de neuronale bandbreedte, m.a.w. steilere actie potentialen leiden tot een grotere cutoff frequentie. Sterker nog dit alles blijkt ook nog eens positief gecorreleerd te zijn met IQ.

Ter conclusie, ik was in staat om één van de factoren te bepalen die de neuronale bandbreedte beïnvloeden, namelijk de steilheid van de actie potentialen. Verder wordt doorheen dit werk getoond dat de transfer functie een meer fysiologische manier is om neuronen te classificeren en hun eigenschappen te bepalen dan de standaard gelijkstroom pulsen en de bijhorende frequentie-stroom curves.

Summary

The brain is a complex system that some consider as the final frontier in understanding the human body. It is the main processing unit of the body and thus it needs to be able to cope with a vast amount of sensory signals, for example, when perceiving our surroundings that vary constantly. The brain is constructed out of billions of neurons, communicating with each other through electrical signals. Somehow these neurons successfully transmit and process the signals of our surroundings.

With computational neuroscience one can investigate how neurons process the constantly varying signals. It gives the researcher total control over each element of a neuron. The accuracy of the model neurons is of utmost importance as any results derived from these models will only be as good as how well the models reproduce the behaviour of real neurons. This creates a tight relationship between computational neuroscience and experimental neuroscience. Whenever models are subjected to a new kind of input, the output needs to be compared with real biological neurons to see if they behave the same way. If a new behaviour is found in biological neurons, the models need to be able to replicate this. There are a lot of types of different models, in this work we will focus us on only one type, namely single cell biophysical neuron models.

In 2005 the Blue Brain Project situated at the École Polytechnique Fédérale de Lausanne, took on the gargantuan task of recreating a cortical column of a rat brain *in silico*, fully detailed. This means including both an accurate cellular morphology and accurate biophysical properties. The cortical column consists out of millions of single cell neuron models, carefully connected via their synapses. Some of these single cell neuron models have been used in this thesis. These neurons can be divided into two main classes: excitatory and inhibitory neurons. The former can make other cells increase their firing rate, the firing rate of a neuron is defined as the number of action potentials in a given time. While the latter promote a decrease in the firing rate of other cells. I have investigated different model neurons from both types.

Besides being excitatory and inhibitory, neurons can be classified according to their firing response, train of action potentials, in reaction to a constant input current, together with their FI-curves. These curves are obtained by injecting different strengths of constant current in the neuron and recording the corresponding firing rate, plotting out the injected current with the recorded firing rate. There are 10 different firing types: classical accommodating, classical non accommodating, classical stuttering, classical irregular, bursting accommodating, bursting non accommodating, bursting stuttering, bursting irregular, direct non accommodating and direct stuttering. Some of these firing types are only found in inhibitory cells while others are

found across inhibitory and excitatory cell types. Note, that these firing types are obtained by using a non-biophysical input, i.e. a constant current, neurons rarely experience this kind of input. So while it is a helpful way of separating neurons into classes it remains unclear whether there is biophysical truth in these subclasses or not. This is one of the reasons that made us choose to not use a direct current to investigate neurons, instead we used a random fluctuating current. This current mimics the synaptic activation from connected neurons. When injecting a neuron with this current the output is supposed to be more biophysical than when using a direct current. However, to properly be able to classify the neurons a relevant signal needs to be added to the stochastic current. This signal is a sinusoidal wave of a certain frequency. Neurons can *phase lock* their action potentials to the frequency of the input sine. *Phase locking* action potentials means that statistically more action potentials will be fired at the crest of the sine than at the trough. How well they can do this for a certain frequency will determine how well they can transfer fast-varying information. Neurons act as low pass filters, they will transfer input signals with a low frequency, or slow-varying information, well but only up to a certain frequency, after this frequency, which is called the *cut-off frequency*, neurons will no longer be able to *phase lock* their action potentials to the high frequency, or fast-varying information, of the input sine. Thus no longer transmitting the incoming information down the line. The frequency domain of the incoming signal can be split into two regions, a first region ranging from 0 Hz to the *cut-off frequency* and a second region ranging from the *cut-off frequency* to an infinite frequency. In the first region, signals will be transferred well between neurons, in the second region the signals will be heavily attenuated, resulting in virtual no transmittance of the signal. This method results in a *transfer function*. This gives us the perfect tool to estimate the information processing capabilities of a neuron.

This work mainly focusses on the properties that influence the excitability of a neuron and the transfer of information. The hypothesis is that if the excitability of a neuron changes the information processing capabilities of that neuron also change. Intuitively this could be explained by assuming that when a neuron increases its excitability it becomes more sensitive to rapid changes in the input signal and thus would perform better at processing fast-varying information. Partly, we focus on the effect of the location of action potential initiation. There is a special section in the axon, called the axon initial segment, in this segment action potentials are initiated and propagated throughout the neuron. *In silico*, we can move this segment along the axon and record the effect on both the excitability of the neuron and its information processing capabilities. From our simulations it follows that

when the axon initial segment, thus the location of action potential initiation, is moved further away from the soma the neuron becomes more excitable. The excitability changes in two ways. First, less current is necessary to elicit spike generation, this implies a lower spike generation threshold. Second, action potentials are steeper at their onset. In other words, action potentials rise faster when they cross the threshold for spike generation. We relate these changes in excitable properties to how well a neuron can handle fast varying information. When the axon initial segment is moved further away from the soma the neuron can transfer information that varies faster. This translates into a higher *cut-off frequency*. There exists a direct relationship between the excitability of a neuron and the information processing capabilities.

Additionally, network models were employed to investigate whether the axon initial segment distance to the soma affects the performance of the network. Separate networks were populated with a specific axon initial segment distance to the soma and were given a simple classification task. Networks that have a bigger distance between soma and axon initial segment perform the classification task better.

Lastly, the influence of the size of the dendritic tree on the *cut-off frequency* was investigated in human neurons. The size of the dendritic tree is positively correlated with the rising speed of the onset of action potentials and with the *cut-off frequency*. Thus, a bigger dendritic tree leads to a neuron with better information processing capabilities. Moreover, the size of the dendritic tree is positively correlated with the IQ of the individual. This indicates that the *cut-off frequency* is a measure for intelligence.

To conclude, I was able to determine one of the factors that influence the information process capabilities of the neuron, namely the steepness of action potentials. Furthermore, throughout this work it is shown that the *transfer function* is a more physiological way to estimate the properties and function of a neuron than the standard constant current pulses and FI-curves.

CHAPTER 1

Introduction

Models and simulations have always been at the center of the scientific method. This not only allows scientists to investigate phenomena that are otherwise inaccessible but also facilitates the building of theories and their validation. While this concept has been very well incorporated into other branches of science, i.e. physics, engineering, etc., in neuroscience it is a relatively new concept that is not yet fully incorporated into the community (Kaplan, 2011).

Neuron models can be separated into two categories. On the one hand there are *multi-compartmental* models, on the other hand there are *point* neuron models.

A *multi-compartmental* model consists out of several physical compartments, each modeling for example a distinct portion of a dendrite or of an axon. In this way, a long dendrite is divided up into smaller pieces. In these small pieces, called compartments, all biophysical parameters are kept constant, as well as the membrane potential. This is referred to as iso-potential compartments. Dividing a dendrite in these compartments is useful to precisely vary the density of certain ion channels, present in only some parts of the dendrite. Cellular somata are generally modeled as a single compartment in multi-compartmental models.

These models differ in a very fundamental way from *point* neuron models. On one side we have a set of differential equations for each compartment, combined to simulate the entire neuron. However, in point neuron models there is only one compartment that represents the whole neuron, i.e. soma, dendrites and axon. This means that in *point* neuron models there is only one set of differential equations.

It was in the early fifties that Hodgkin and Huxley described quantitatively the mechanisms underlying the ionic currents in a neuron by means of a mathematical model. Their model of the squid giant axon is considered the first real attempt to model, hence also simulate on a computer, the electrical activity in a neuron and by extension also the brain. Their model was the first to accurately describe ionic currents flowing through the membrane at any given time in a neuron. Therefore it is still one of the most important neuron models used today in computational neuroscience. A good model has different requirements, the most evident one is that it needs to predict experimental data nicely. For the model Hodgkin and Huxley (HH) proposed in 1952 this was the case, and for the first time scientists could

mechanistically explain the neuron activity (Hodgkin et al., 1952; Hodgkin and Huxley, 1952a, 1952b, 1952c, 1952d; Hodgkin and Katz, 1949). A model should adhere to two main principles. On the one hand, it should be possible to simplify the model, for example when one is calculating the trajectory of earth around the sun, in principle one should take into account the mass and distance of other solar systems and galaxy but their influence is so negligible that it can be neglected in our calculations. On the other hand, a model should also be able to be extended. If one would for example calculate how fast an object is falling according to Newton's laws, it is not always necessary to incorporate drag forces into the calculation, but it is possible. In the very same way the HH model can be extended to make it more accurate, by adding in different ion channels. We will discuss later how this is done. In *point* neuron models we can make a distinction between two classes. On the one hand there are the HH-based single compartmental models. On the other hand there is the integrate-and-fire family (IF). This model was first put forward by Louis Lapicque in 1907, a good fifty years before HH proposed their model (Abbott, 1999; Brunel and Van Rossum, 2007). The IF model was then expanded into the leaky-IF (LIF) model, which has been used a lot in network simulations and in the theoretical study of biological neural network properties. In 2003, almost 100 years after the original introduction of the IF model, Fourcaud-Trocmé introduced the exponential integrate-and-fire model (EIF), together with the quadratic integrate-and-fire model (QIF) (Fourcaud-Trocmé et al., 2003). It turns out that the EIF model very accurately can predict neuronal sub-threshold voltage fluctuations and on top of that also timings of action potentials (AP) (Badel et al., 2008a, 2008b).

However, in these days of artificial intelligence and deep learning, one shouldn't forget about network models, the third class of models, though it will not be discussed at great length in this work since it is not the main focus here. The largest difference with the models discussed above is that these network models, mostly, consist out of non-spiking neuron models. These models only capture the summation and threshold dynamics of biological neurons. These model will not exhibit spiking behavior. Recurrent neural networks, convolutional neural network or liquid state machines (LSM) are just a few examples of such possible networks (Maass et al., 2002; Maass and Markram, 2002).

1.1 The Axon Initial Segment

We will start by describing a very specific section in the axon. It is this particular section, the axon initial segment (AIS), that is at the center of my research. We will go over the particular properties of this section, why and how it is important in action potential (AP) initiation. This section is largely based on the review of (Kole and Stuart, 2012).

It has been understood for a long time that AP initiated at the AIS for a long time. This stems from a collection of landmark experiment performed in the 50's (Araki and Otani, 1955; Coombs et al., 1957; Fatt, 1957; Fuortes et al., 1957). However, finding the biophysical reasons for AP initiation in the AIS proved to be more difficult. In the 70's computational studies showed that a high concentration of Na^+ channels is necessary for AP initiation in the AIS (Dodge and Cooley, 1973). In line with this, early binding studies showed a high concentration of Na^+ channels in the AIS in cultured spinal cord neuron and retinal ganglion cells (Catterall, 1981; Wollner and Catterall, 1986). Surprisingly, functional patch clamp experiments showed a density of Na^+ channels in the AIS that was similar to that of the soma (Colbert and Johnston, 1996; Colbert and Pan, 2002). These estimates, however, are countered by more recent experiments and can be explained by the following effect. The Na^+ channels are tightly coupled with the actin cytoskeleton which makes it harder to draw them into the recording pipette, hence underestimating the density of Na^+ channels. This is further confirmed when the actin cytoskeleton is chemically disrupted, which results in a much larger Na^+ current in patch clamp experiments (Kole et al., 2008). These electrophysiological experiments show that there is a higher density of Na^+ channels present in the AIS with respect to the soma. Recently this was confirmed by (Lorincz and Nusser, 2010), using quantitative freeze fracture immunogold labeling they showed that in the AIS of hippocampal pyramidal neurons the density of $\text{Na}_v 1.6$ channels is around 40 times higher than in the soma. However, another study using Na^+ dye imaging showed only a 3 times higher concentration of Na^+ channels in the AIS versus the soma, in cortical neurons, this is a prediction that is obtained from combining the dye imaging with modeling (Fleidervish et al., 2010). It is highly likely that this high difference is due to methodological differences. Nevertheless, it shouldn't be overlooked that there can be large difference between Na^+ channel densities

across cells; due to axonal morphology, neuronal activity, variability in the electrical load of the somato-dendritic compartment. Together with the fact that immunocytochemical studies do not give any information about functional channels, in contrast channel density estimates, based on Na⁺ imaging, rely heavily on accurate modelling of Na⁺ diffusion. In morphological realistic models one can use the unbiased matching of a large range of AP properties to determine the amount of Na⁺ channels in the AIS. This approach showed that in large cortical pyramidal neurons a ratio of 50 to 1 exists for Na⁺ channels between AIS and soma (Kole et al., 2008). In contrast, in the much more electronically compact dentate granule cell only a 5 to 1 ratio exists (Schmidt-Hieber and Bischofberger, 2010). The AIS is not only unique because of its density of Na⁺ channels but also because of the properties of these channels. The most notably different properties are a lower threshold for activation and inactivation, a difference of around 10 mV compared to Na⁺ channels in the soma (Colbert and Pan, 2002; Hu et al., 2009; Kole et al., 2008), and faster kinetics of the Na⁺ channels in the AIS than in the soma (Schmidt-Hieber and Bischofberger, 2010), around twice as fast (in)activation in the AIS.

The repolarization of AP are mainly governed by K⁺ channels. Additionally, these channels also contribute to determining the AP threshold, inter spike interval and firing frequency. In the AIS the most predominant K⁺ channel is the K_v 1 subtype (Dodson et al., 2003; Goldberg et al., 2008). In cortical pyramidal neurons a high density of dendrotoxin-sensitive, fast-activating and slowly inactivating K⁺ current is present. At the end of the AIS, in pyramidal neurons, antibody staining show a large presence of K_v 7.2 and K_v 7.3 channels (Devaux et al., 2004; Pan et al., 2006). In contrast to the K_v 1 subtype, these channels have a slow activating and noninactivating M-type current. (Brown and Passmore, 2009)

All these factors make the AIS the place for AP initiation, without answering the question on why the AIS evolved to be the location of AP initiation. In other words what is the benefit of having a very precise location, more specifically the AIS, as the AP initiation site? Different neuronal cell types have a wide range of different voltage-gated ion channel expression in the AIS, as discussed in this section. This will result in a very specific transformation of the synaptic inputs into output signals, depending heavily on the type of neuron that is processing the inputs. Both voltage sensitive

dye imaging and electrophysiological recordings confirmed that the AP initiation occurs at the distal end of the AIS (Atherton et al., 2008; Foust et al., 2010; Kole et al., 2007; Meeks and Mennerick, 2007; Palmer et al., 2010; Palmer and Stuart, 2006; Popovic et al., 2011; Schmidt-hieber et al., 2008; Shu et al., 2007a). The diameter of the AIS is habitually an order of magnitude smaller than the rest of the neuron, giving the AIS a very small capacitance. Consequently, it requires less inward current to reach the threshold for spiking in contrast to larger elements of the cell, such as the soma or dendrites, making the AIS an energy advantageous location for AP generation. An additional benefit of having a single location for AP initiation, is that only this one location needs to be inhibited to gate AP generation.

Another benefit of initiating APs in the AIS is temporal coding. Because the AP backpropagates from the AIS to the soma there is a temporal shift between the synaptic input and AP initiation. This causes the threshold for AP generation at the soma to be more depolarized with respect to that of the AIS (Kole and Stuart, 2008). On top of this the threshold at the soma exhibits much more variability than that of the AIS (Yu et al., 2008). It has been shown that in nucleus laminaris neurons, in birds, properties of the AIS, such as the distance to the soma, the length of the AIS, is dependent on the presynaptic firing rate. For example, neurons that are tuned to a high characteristic frequency (> 2 kHz) have Na^+ channels in the AIS located further away from the soma, in contrast to neurons tuned to lower frequencies (< 1 kHz) that have those respective channels in the AIS closer to the soma. Furthermore it was shown that neurons that have these Na^+ channels further away in the AIS are better suited to determine interaural timing differences (Kuba et al., 2006; Kuba and Ohmori, 2009).

Lastly, I shortly comment on the relation between the AIS and diseases. Since the AIS controls excitability it is apparent that the smallest change in the properties can contribute to a pathogenesis of neurological disorders, because of failure in protein expression or trafficking. It was already realized very early on that the AIS could play a role in epilepsy. This was concluded from observations of anatomical GABA-ergic synapses targeting the AIS of cortical pyramidal neurons (Ribak, 1985). These neurons are in an utmost strategic location to synchronize a neural network since they only receive inputs from five axo-axonic cells but they project to anywhere between 250

and 1000 different hippocampal neurons. It has been hypothesized that for temporal lobe epilepsy the loss of inhibition at the AIS could contribute to the etiology of epilepsy (DeFelipe, 1999). Since recent work showed that these axo-axonic neurons can also be excitatory. Fujiwara-Tsukamoto and co-workers showed that in in vitro models of seizures these cells can create a positive feedback loop during epileptic events (Fujiwara-Tsukamoto et al., 2004). However, it is not established yet whether these effects are causal to epilepsy or rather consequential.

1.2 Theories about the “temporal sharpness” of AP generation

Through recent years it has been found that AP initiation at the soma doesn't correspond to the standard HH equations. Briefly, sodium channels in the soma open in an all or none fashion. This is in contrast with the standard definition of sodium channels in the soma, where sodium channels have a finite Boltzmann slope factor of Sodium activation. So to have AP initiation that is fast at the onset the Boltzmann slope would go to 0. In the last decade a few theories to elucidate this discrepancy were formed. While the purpose of a sharp onset of APs intuitively can be interpreted to facilitate faster reaction times and shorter APs, the purpose for a high variability in somatic spike threshold is a bit more elusive and might even seem counter intuitive. Nonetheless it has been shown that this high variability is a necessary element for information processing in the cortex (Azouz and Gray, 2003, 2000, 1999; Wilent and Contreras, 2005). It can both limit the reliability of information transfer as well as serving as a coincidence detector. This high variability has two main contributors, on the one hand this variability is influenced by variations in the rate of change of the membrane potential while approaching the onset of the AP, on the other hand it depends on the history of the AP generation (Azouz and Gray, 2000, 1999; Henze and Buzsáki, 2001; Shu et al., 2003). Surprisingly enough this only accounts for roughly sixty percent of the variability that is found in experiments, clearly an important factor to this variability still needs to be elucidated. Together with this, there doesn't seem to be a clear explanation for the sharp onset of APs either, this leaves two phenomena that seemingly can't be described by iso-potential HH-models.

1.2.1 Cooperative Sodium channels

This was the problem that (Naundorf et al., 2006) were facing. On closer investigation of the equation of Hodgkin and Huxley, it turns out that there is a limit on the rate of depolarization. This limit is determined by

$$\frac{g_{Na}h_0m_{\infty}^3(V)(V_{Na} - V)}{C} + \frac{I_0}{C}$$

Where g_{Na} represents the peak sodium conductance, h_0 the fraction of sodium channels that can be activated, $m_{\infty}^3(V)$ the activation curve, C the membrane capacitance and I_0 current carried by other channels. After careful manipulation of all these variables Naundorf and colleagues found it impossible to retrieve the behavior they had found in vivo and in vitro. From the sharp onset they concluded that many sodium channels should open simultaneously.

Looking at other body parts and channels, (Dekker and Yellen, 2006; Marx et al., 1995; Molina et al., 2006), they proposed the theory of cooperative sodium channels, which claims that as a sodium channel opens it recruits neighboring sodium channels to open as well.

A lot of criticism was voiced on this theory, mainly claiming that in their model and theory they didn't account for the AIS, which is the location where APs are initiated in most neurons. As a rebuttal however they claimed that cooperative sodium channels could also be present in the AIS, (Öz et al., 2015). This seems rather unlikely, mostly since the APs in the AIS don't show a very steep onset speed but rather a shallow rising speed, more comparable to the standard HH-equations. Moreover it was shown experimentally that cooperative sodium channels in the AIS aren't required for a fast onset of APs, (Hu et al., 2009).

1.2.2 Active backpropagation

The theory of active backpropagation, first proposed in (Yu et al., 2008), came as a reaction on the cooperative theory, discussed in the previous paragraph. The most striking difference with the previous theory is that Yu et al. considered a more detailed, thus realistic, neuronal model. They included not only an axon but also, more importantly, an AIS in their model. This section in the axon seems to be of utmost importance in trying to explain the higher variance of spike threshold and the sharp onset of APs, mainly because of the fact that in this section the AP is initiated. It is at this location in the neuron that an AP will be measured first and then propagate through the whole neuron. Moreover, it is imperative that this location is separated from the soma by some distance, since at the AIS the generated APs are less sharp at onset than the ones recorded at the soma. These properties are the chief pillars the backpropagation theory is built on. Yu et al. claim that it is because of this distance between AIS and soma together with the higher concentration of Na^+ channels present in the AIS that while the AP is back propagating to the soma and dendrites it is sharpening the onset of the AP while moving through the axon, resulting in a sharp onset of the spike. Additionally, it also increases the variability of the voltage threshold for spike generation. Nonetheless while it is a simple and straightforward theory the main argument that can be made against it, is that the distance between soma and AIS necessary to create the sharpening of the onset of AP solely due to active backpropagation would be unrealistically large.

1.2.3 The critical resistive coupling theory

The last theory we will discuss was first proposed by (Brette, 2013) and later corroborated by his colleagues (Telenczuk et al., 2017). Their theory is called critical resistive coupling and it states that because of the noticeable size difference between the soma, together with the dendrites, versus the AIS and the relatively close proximity of one to the other the soma will act as a

current sink. Furthermore, they claim that instead of spike initiation through a local axonal current loop, spike initiation happens with a global current loop including the soma. Subsequently the sodium currents are counteracted by the resistive axial current flowing to the soma rather than the local transmembrane currents. So the soma and AIS, at spike initiation, form a dipole and so it is not sensible to speak about wave propagation, i.e. backpropagation, since the wavelength would include both soma and AIS. They prove, in several ways, that when the capacitance of the soma is big enough sodium channels in the soma will open in an all-or-none fashion, resulting in a very sharp onset of APs. Furthermore, they show, by simulations, that there is no need for a back propagating AP to generate sharp potentials at the soma. In silico this is can be checked by disabling any active channels between the soma and AIS, disabling in this way active backpropagation. To further underline that backpropagation is not necessary for a sharp onset of the AP, a two compartmental model was used, connecting a soma and AIS via a resistance so there is no effect of propagation through space at all, in which they showed the same effect as previously described. It is this theory that shows the most credibility and hasn't been disproved in any way up to today. Therefore, it is this theory that will be used throughout this work as a guideline.

1.3 The morphological location of the AIS

It follows from the critical resistive theory (Brette, 2013; Telenczuk et al., 2017) that the location of the AIS in the axon with respect to the soma has an influence on the properties of the neuron. So it is not only the biophysical properties of the AIS, as discussed in 1.1, that are important with regards to AP generation but also the three dimensional location with respect to the soma that is of importance.

If one looks at a simple ball and stick model, where the ball represents the soma and the stick would represent the axon, one can create an AIS segment by increasing the density of sodium and potassium channels in that specific part of the axon. If the AIS is moved inside the axon further away from the soma, this can be achieved by moving the concentration of sodium and

potassium channels as described before, the neuron is found to be more excitable, i.e. the neuron has a lower threshold to fire APs. It is mainly this effect that spurred this research, if the location of the AIS has an influence on APs parameters, such as threshold to fire, it is reasonable to hypothesize that it also has an influence on input-output transfer properties of the neuron. Even more so when one considers that AP properties are a very big influencer on these transfer properties.

1.4 The neuronal models of the Blue Brain Project

Since it is impractical to investigate the effect of the location of the AIS on the general excitability of the cell and on the ability of the cell to transfer information, see later, we chose a modelling approach. To examine single cell properties a multi-compartmental model is the best approach. This is why we chose for the multi-compartmental models of the Blue Brain Project (BBP), which are arguably the most complex and accurate multi-compartmental models to date.

In 2005 the Blue Brain Project, at the École Polytechnique Federale de Lausanne (EPFL), made a huge contribution to the computational neuroscientific field (Markram et al., 2015). In this work the experimentalists replicated a neocortical column into an *in silico* column, consisting out of thousands of individual multi-compartmental models. These individual HH neuron models are the most realistic representations of real neurons in two aspects.

The first part is the morphology of the neuron. Neurons from the six layers in the somatosensory cortex were recorded, this in P14 male Wistar rats, by using the well-established technique of patch-clamping in vitro slices. A total of 1009 neurons were successfully stained, recorded and labeled. These were first separated in so-called m-types, these morphological types or m-types are well defined by some of the first neuroanatomists (Karagiannis et al., 2009; Karube et al., 2004; Kawaguchi and Kubota, 1997; Kisvárdy et al., 1985; Larkman, 1991; Perrenoud et al., 2013; Peters and Kaiserman-Abramof, 1970; Ramón y Cajal; Somogyi et al., 1998, 1982; Wang et al., 2004; Yuste, 2005). These classifications are based on characteristic features of axon, dendrites and somatic shape. This resulted in 55 distinct m-types,

acquired from clustering characteristic features. Some interesting facts can be noted once these m-types have been constructed. Namely, that the biggest difference among inhibitory morphologies appear to be the axon features, for the excitatory cells however these are the dendritic features; furthermore it can be noted that layer 1 is the only layer that has unique morphological types; while pyramidal cells are more numerous the deeper one goes in the cortical layers. While this is still the most accepted view in the community, recent research in axon modelling and morphology reconstruction of excitatory neurons has shown that there is also a larger diversity in axon morphology for these excitatory neurons. (Winnubst et al., 2019).

This is only one part of the figurative equation to get a realistic, functioning neuron model. Besides a detailed morphology one also needs a detailed description of the electrical properties of the neuron. The firing responses are described in the so-called *Petilla* convention (Ascoli et al., 2008). This convention makes a separation based on two aspects of a train of APs. The first aspect describes whether the train is: continuous (c), bursting (b), or delayed (d). A continuous train means that AP start firing at the onset of a depolarizing current, sufficiently large to elicit AP, bursting is characterized by multiple APs in a very short time at the onset of the depolarizing current and lastly a delayed train will have a significant silent period in the beginning of a depolarizing current after which an AP will start.

The second part of the *Petilla* terminology is based on how the AP train evolves in time. The options here are: accommodating (AC), non-accommodating (NAC), irregular (IR), stuttering (STUT). For AC AP trains the inter spike interval (ISI) will become longer as the train evolves through time, NAC trains will have a constant ISI during their whole AP train, IR neurons will have variable ISI while STUT have quiescent periods with short AP trains in between that have almost constant ISIs. By combining these two characterizations the firing type of the neuron can be described, i.e. cAC which then stands for continuous accommodating. Note that not all combinations are found in neocortical cells. For excitatory cells, the only combination that is perceived is cAD, continuous adapting which is the same as continuous accommodating but for excitatory cells the term adapting is used. For the inhibitory cells there are 10 different types that are observed: cAC, cNAC, cSTUT, cIR, bAC, bNAC, bSTUT, bIR, dNAC, dSTUT. It is

by a series of different stimulation paradigms that all the recorded neurons, in the work of Markram et al. 2015, were investigated and classified as one of these types based on their firing pattern. It also verifies the work done by (Khazen et al., 2012) that distinct e-types have specific ion channel profiles. These e-types can now be combined with the distinct morphologies, m-types, to create the so called me-types. Note that a morphology can have different e-types. This results in a total of 207 distinct me-type neurons (morphological electrophysical type), fig 1.1.

The ion channels are the last piece of the puzzle to create realistic neuron models. To create these models the authors took a reconstructed morphology into a simulator, NEURON (Carnevale and Hines, 2006; Hines and Carnevale, 2001). The morphology was divided into iso-potential compartments with a maximal length of 20 μm . Passive properties of all of these compartments were set to values agreed upon in literature, not mentioned here for the sake of brevity. For the active components the 13 most important ionic current known in cortical neurons were added, together with Ca currents. These 13 ionic channels included the following: transient sodium, persistent sodium, transient potassium, persistent potassium, m-current, h-current, high voltage-activated calcium, low voltage-activated calcium, Kv3.1, d-type potassium, stochastic potassium, SK calcium-activated potassium. All channel kinetics were obtained from published model or experimental data (Adams et al., 1982; Avery and Johnston, 1996; Colbert and Pan, 2002; Diba et al., 2006; Köhler et al., 1996; Kole et al., 2006; Korngreen and Sakmann, 2000; Magistretti and Alonso, 1999; Rettig et al., 1992; Reuveni et al., 1993; Shu et al., 2007b). All ionic currents were modeled with the classic HH equations:

$$I = \bar{g}m^xh^y(V - E)$$

Where \bar{g} stand for the maximal conductance of a specific channel, x and y respectively the number of gates of activation and inactivation, E the reversal potential of the ion and V the membrane voltage. All ion channels were distributed in an uniform way across the whole neuron, except for I_H which has an exponential distribution in the apical dendrites for excitatory cells, (Kole et al., 2006), and in the dendrites for inhibitory cells. To determine actual densities of all these channels a feature-based multi-objective optimization method was used, as described in (Druckmann et al., 2007). Within this optimization, the free parameters are the channel conductances in

the neuron model. In this way a total of 1035 distinct neuron models were created, for every me-type there are 5 different instances to capture nature’s variability. In this paragraph only the relevant information for this work was discussed from (Markram et al., 2015). The work they performed went much further than presented here, the end goal of that work was to recreate a full cortical column in silico, with functional synapses and correct connectivity between cells and layers. While their work is more focused on the network in full, our work is more focused on the role of an individual neuron.

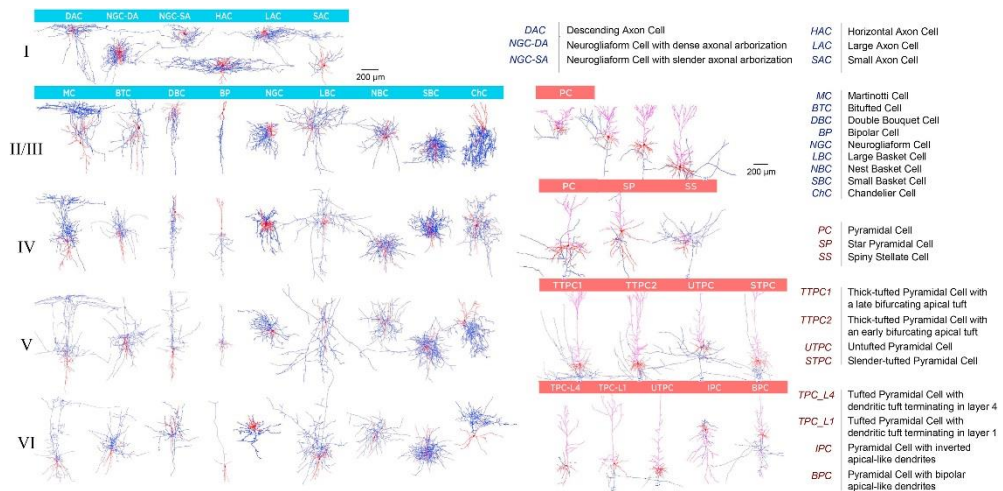


Figure 1.1 Overview of the different morphologies available in the BBP repository. Horizontally organized by layer and vertically by morphology type. The blue bar indicates inhibitory cells, the red bar excitatory cells.

1.5 NEURON simulator

At this point we have the models but a simulation environment is still needed. The decision was partly made for us by the choice of the models, the BBP models were developed for use in the NEURON simulator (Carnevale and Hines, 2006; Hines and Carnevale, 2001) although they can be used in other simulators as well. Since the models were optimized for the NEURON simulator, we decided to use it, as briefly described below.

Simple single compartment HH-models can be simulated “manually” in almost any programming language, from Python, C++, java to MATLAB or Julia, by using Euler’s method to solve the ordinary differential equation (ODE) iteratively. However, once a multi-compartmental HH model is required it becomes a bit more difficult, at this point it is wise to make use of

one of the many available simulators. The NEURON simulator can be used in several ways, through different programming languages or through a visual interface. The native language of NEURON is called HOC, this is loosely based on C/C++. However, in the beginning of this project it was decided that the python interface would be used. This interface makes it possible for the user to circumvent the HOC-side of NEURON for the biggest part. In this way you can use python functions to invoke HOC routines. This choice was made to decrease the number of different languages needed to complete any simulation, visualization, storing and analysis. In this way simulation of the models and visualization could both be handled very easily within python, as well as data storage for further analysis in Julia later.

Much like the creation of the neuron models by Markram and coworkers was a two-step process, i.e., the morphology and the ion channels, initializing simulations in NEURON is as well. The first thing one needs to do for simulating a single neuron model, is loading in the morphology. The neuron's morphology can be loaded into the simulator as a text file. In this text file coordinates are specified of soma, dendrite and axon together with the diameter of each section. At this point the simulator contain an empty shell of the neuron, the exact morphology is present but no ionic channels are present yet, this is the last step before one can simulate the neuron.

Inserting ionic channels can be done in several ways, either completely through python by using the python defined functions or completely in HOC, only using the HOC language and syntax. However, a third option was used in our particular case, when we are using the BBP models. The models of the BBP are published in a very structured way, with a lot of functionalities present in the downloaded repository. For every model there is a so-called "*biophysics.hoc*" file. In this file the distribution of all the ionic channels, together with local densities, are described for every segment of that specific neuron model. Through the python interface it is possible to import these pre-made HOC files directly into your already existing morphology. At this point the model is ready to be simulated.

Now the model can be stimulated, this can be done in several ways. Either by the standard in vitro technique of voltage or current clamp or by creating synaptic activity. In this work the current clamp technique will be exclusively used. Membrane voltages can be measured anywhere in the

neuron, in practice of the whole neuron at the same time, at every simulation time step, even so it is only measured at the center of the soma, in most cases.

1.6 The Julia programming language

Once the models are simulated, their output consists of some form of data that we have to analyze. To do this one can use many tools that are freely available to analyze scientific data. However we choose a relatively new software which works very efficiently, namely Julia (Bezanson et al., 2017). Most of our data is analyzed in this software. This section serves as an introduction of Julia to the larger public, since it is such a young programming language, yet it could eventually replace commercial software such as MATLAB

Analysis of all kinds of data, from in vitro or in vivo recordings of neuronal activity to results of physics experiments, are being analyzed by what are called dynamical languages, or dynamically typed languages, such as MATLAB or python. The disadvantage of these languages is that they're often much slower than the statically typed languages, C or Fortran. This is partly because of the simplicity and versatility of MATLAB or python at the user level. The competition of these high-level languages, i.e., MATLAB and python versus the low-level languages, i.e., C and Fortran, is one of productivity versus performance. In the former languages it is much easier to write complex equation and find their solution, the latter however will produce results much faster once the complex equations are programmed. So it is rather a question of what the scientist is interested in, speed in production or speed in execution. In the scientific community, the former is often preferred since it is easier for the user.

There seems to be a void in the cross section between performant languages and easy-to-use language. It is this void that Julia tried to fill a few years ago, by being as efficient as Fortran but as easy to use as MATLAB. Julia lets the user write high-level abstract code, closely resembling mathematical formulas, but it produces efficient and fast low-level machine code that can generally only be obtained by static languages.

It was for these reasons that Julia was chosen as the preferred language for

processing the data obtained from neuronal simulation. Note that the relevant data for most of our calculation is very sparse, i.e. the APs, within a large amount of data points, i.e. subthreshold voltage fluctuations.

1.7 The *transfer function* of a neuron

To systematically investigate the models in the chosen simulator we need a certain *in silico* experimental protocol. Since we are interested in how the models transfer information, we will be using the so-called *transfer function*. This protocol characterizes neuronal firing behavior in more biophysical way rather than the classic static FI curves that are more conventional. The transfer function will not only allow us to characterize the neuronal firing behavior but will also inform us about the information transfer capabilities of the neuron. It are these capabilities that we are the most interested in, combined with how they are correlated with the location of the AIS and its excitability.

Since the time of Hodgkin and Huxley, an injection of block pulses has been used to characterize neuronal firing behavior and activity. While these block pulses give rise to distinct firing patterns of the neuron, as is discussed in section 1.4, they hardly represent any realistic, biophysical input to the neuron. This is why a lot of researches in the neuroscientific community (Boucsein et al., 2009; Brunel et al., 2001; Eyal et al., 2014; Fourcaud-Trocme et al., 2003; Ilin et al., 2013; Köndgen et al., 2008; Linaro et al., 2018; Naundorf et al., 2005) have started to use a dynamical estimator of neuronal activity. This is what is often called dynamical response or frequency response of a spiking neuron. The difference with, what we will from now on call, the static response are the features of the input current that is used to estimate the output of the neuron. In the dynamical response one aims to mimic more accurately the summation of inputs a neuron would receive at the soma from the entire somatodendritic compartments, i.e. all the synaptic activity passed to the dendrites, resulting in a colored noisy current. In practice there are two different ways to approach investigating the dynamical response, in the end both approaches lead to a so-called transfer curve. It is this transfer curve that is the equivalent output from the

dynamical response to the FI-curve that one generally obtains from the static response paradigm. However, the dynamical response reflects more accurately how the neuron would respond in an in vivo situation, making it possible to make better estimations about the functionality of certain neurons.

The first method, which was proposed by (Higgs and Spain, 2009) and adapted by (Ilin et al., 2013), to obtain a transfer function is illustrated in *Figure 1.2*. In this protocol one injects a neuron, be it in a patch-clamp setup in vitro or in a simulation in silico, with a noisy current. This current is based on the following equation:

$$I(t) = I_0 + \sigma_{noise}\eta(t)$$

Where η is an Ornstein-Uhlenbeck process, with zero mean and a unitary variance. The correlation time of the noise is typically set within a range of 5 to 20 ms. The standard deviation of the background noise is determined by σ_{noise} . It was shown by (Destexhe et al., 2003) that this Ornstein-Uhlenbeck process mimics the effect identified in the soma by balanced excitatory and inhibitory synaptic events. The direct current I_0 is added to create an offset and ensure that the neuron fires around a stable non zero firing rate, typically in the range of 3 to 10 Hz. Then from this injected current and from the resulting spike train, recorded at the soma, the input current autocorrelation, c_{ss} , and spike triggered average, c_{sr} , respectively are calculated. According to the following formulas, note that $s(t)$ only consist out of the noise part of the injected current and the offset is neglected in any further calculation, also that $r(t)$ consist out of a vector the same length as $s(t)$ with ones at every spike time and zeros everywhere else:

$$\begin{aligned} c_{ss}(\tau) &= \langle s(t)s(t + \tau) \rangle \\ c_{sr}(\tau) &= \langle s(t)r(t + \tau) \rangle \end{aligned}$$

To reduce the effect of noise after performing a Fourier transformation a gaussian filter will be applied on the input correlation and spike triggered average, this filter is frequency dependent.

$$\begin{aligned} w(f, \tau) &= \exp\left(-\frac{\tau^2 f^2}{2}\right) \\ C_{ss}(f) &= \sum(c_{ss}(\tau)w(f, \tau)e^{-i2\pi f\tau} d\tau) \\ C_{sr}(f) &= \sum(c_{sr}(\tau)w(f, \tau)e^{-i2\pi f\tau} d\tau) \end{aligned}$$

This can be calculated for any range of f that is desirable. The ratio of the absolute values of these Fourier transforms then gives us the transfer function:

$$TF = \frac{|C_{sr}(f)|}{|C_{ss}(f)|}$$

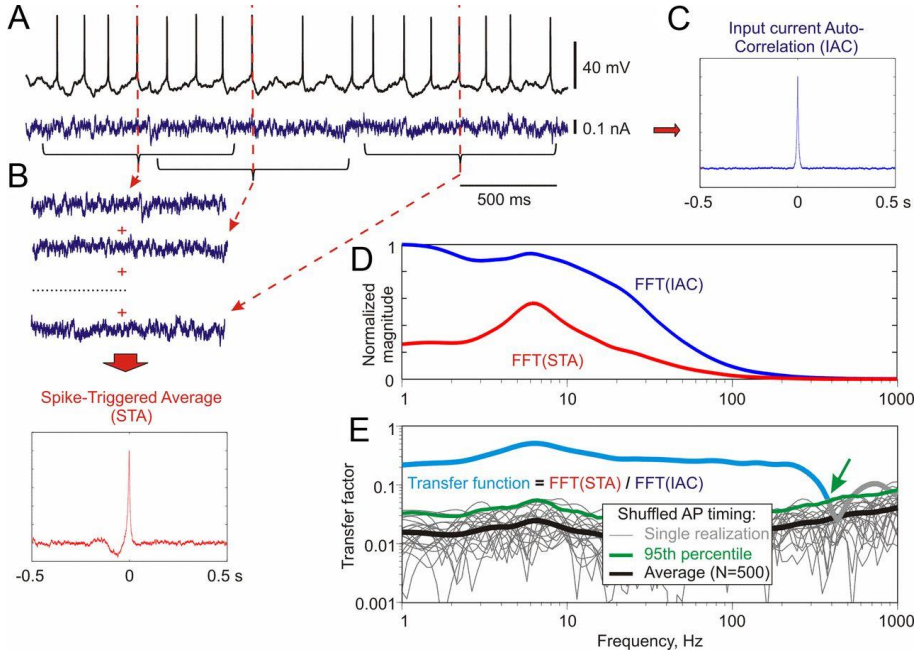


Figure 1.2. Panel A shows respectively the output membrane voltage recorded at the soma and the injected randomly fluctuating current. Panels B shows the spike-triggered averaged as described in the text, whereas C shows the autocorrelation of the input with only a peak at the 0 time delay. In panel D, one can see the Fourier transforms of both correlations, in E the division of both is made resulting in the actual transfer function, blue line. Significant levels can be obtained by a circularly shifting ISI and recalculating the transfer function, denoted in black and green lines in panel E. From Ilin et al. (2013).

While the first paradigm focused only on injecting a noisy current, the second will add a small sinusoidal component in the input current, closely following a protocol used by (Boucsein et al., 2009; Köndgen et al., 2008; Tchumatchenko et al., 2011).

$$I(t) = I_0 + \sigma_{noise}\eta(t) + \epsilon \sin(2\pi ft) \quad (1.1)$$

Where the first two terms are the same as in the first paradigm, ϵ is roughly a third of σ_{noise} . From the recorded membrane voltage, spike timings are taken and mapped onto the input sine to get a phase delay corresponding to a

certain spike. These phase delays are used to put every spike on a unitary circle, with their angle between the positive x-axis and the resulting vector equal to the phase delay of the recorded spike. All of these unitary vectors are then averaged to result in one vector, no longer with unitary length, depicted as a red arrow in *Figure 1.3-C*. The length of this vector now represents the phase-locking ability of the firing neuron. Thus also the ability to encode the frequency of the stimulus. This protocol can be repeated for different frequencies and in a such a way the same transfer curve can be obtained as with the first protocol. However this procedure has an additional benefit, the resulting vector, the red arrow in *Figure 1.3-C*, has an intrinsic phase delay as well, representing the phase delay between the output of the neuron versus the input. As will be discussed later this phase delay will increase for higher frequencies of the input sine. There is an additional method to analyze the recorded membrane voltage from this kind of input, as shown in eq 1.1. One can cut the recorded membrane voltage according to the period of the injected sine and then bin spikes from the whole trace together within a certain small time interval, resulting in a histogram. This histogram can then be fitted with a sine of the same frequency as the input sine. The amplitude of this fitted sine represents the phase-locking ability of the neuron for that specific frequency. In this way the same transfer curve can be established. However this method suffers a bit when high frequencies are injected. At this point sinusoidal curves become hardly detectable in the output, which makes fitting the resulting histograms very difficult and inaccurate.

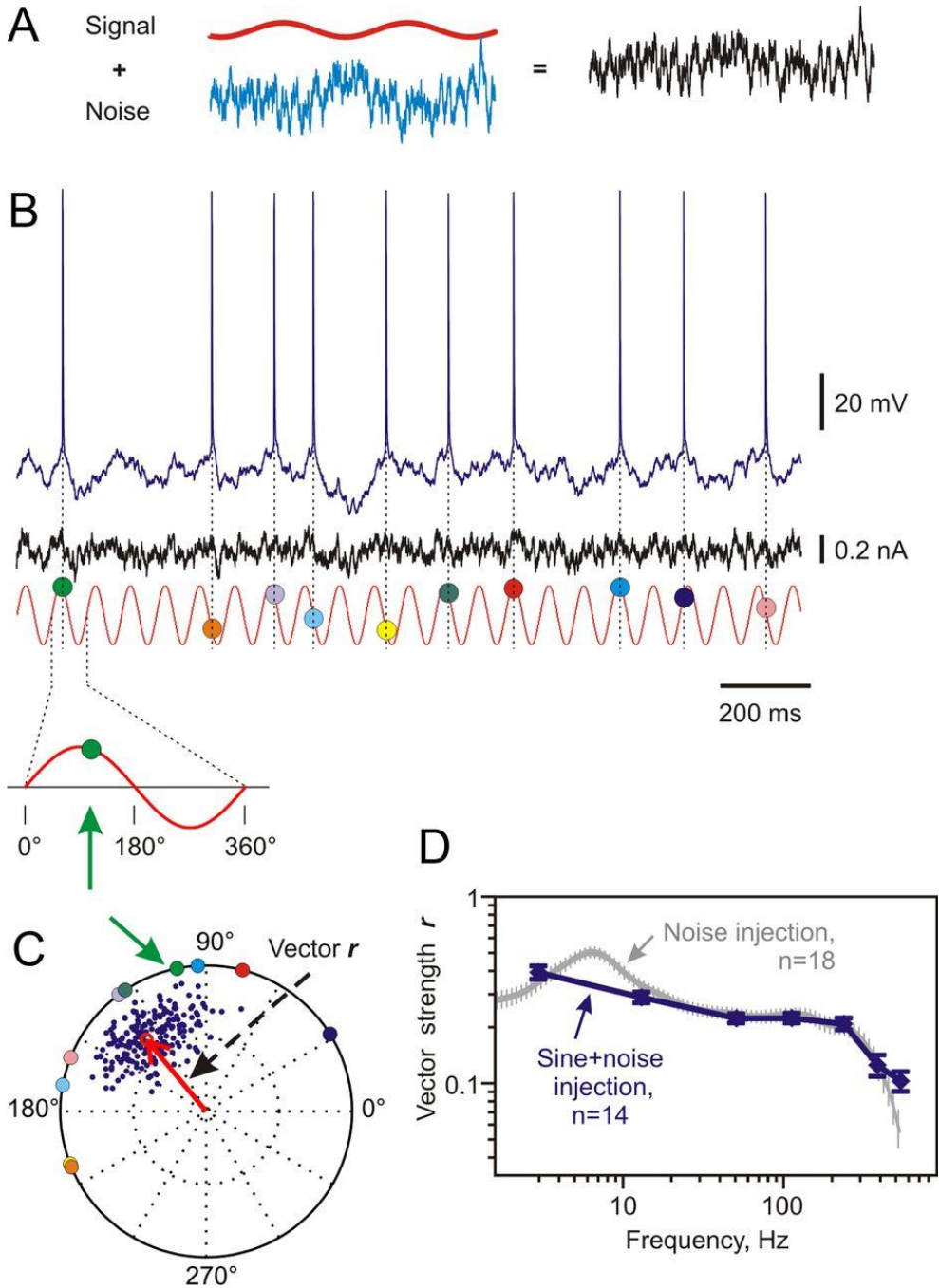


Figure 1.3. Panel A shows that the input into the neuron is a summation of a noisy current together with a sinusoidal current. In panel B one can see the recorded membrane voltage at the soma, where spike times are mapped onto the sinusoidal part of the input current. To each of these time a phase lag can be attributed and put on a unitary circle as shown in panel C. When one takes the average of all these filled markers it results in the red open circle. The length of this vector is then the strength in the transfer function, which is plotted in panel D. Resulting in a similar graph as in Figure 1.2-E. From Ilin et al. 2013.

Once the transfer curve is obtained a cut-off frequency (COF) can be defined. In this work the definition was chosen to be 70.07 % of the strength of the phase locking for an input frequency of 1 Hz. It is this cut-off frequency that can be used to compare the input-output properties of a neuron. A neuron that has a high COF will be more adept at transferring signals with a high frequency than a neuron with a low COF, since neurons act fundamentally as low pass filters. An additional benefit of a high COF is that these neuron can respond, with their mean output firing rate, much faster to sudden step changes in the input current, as described in (Brunel et al., 2001; Linaro et al., 2018).

1.8 References

- Abbott LF. 1999. Lapicque's introduction of the integrate-and-fire model neuron (1907), *Brain Research Bulletin*.
- Adams PR, Brown DA, Constanti A. 1982. M-currents and other potassium currents in bullfrog sympathetic neurones. *J Physiol* **330**:537–72. doi:10.1113/jphysiol.1982.sp014357
- Araki T, Otani T. 1955. Response of single motoneurons to direct stimulation in toad's spinal cord. *J Neurophysiol* **18**:472–485. doi:10.1152/jn.1955.18.5.472
- Ascoli GA, Alonso-Nanclares L, Anderson SA, Barrionuevo G, Benavides-Piccione R, Burkhalter A, Buzsáki G, Cauli B, DeFelipe J, Fairén A, Feldmeyer D, Fishell G, Fregnac Y, Freund TF, Gardner D, Gardner EP, Goldberg JH, Helmstaedter M, Hestrin S, Karube F, Kisvárdy ZF, Lambolez B, Lewis DA, Marin O, Markram H, Muñoz A, Packer A, Petersen CCH, Rockland KS, Rossier J, Rudy B, Somogyi P, Staiger JF, Tamas G, Thomson AM, Toledo-Rodriguez M, Wang Y, West DC, Yuste R. 2008. Petilla terminology: Nomenclature of features of GABAergic interneurons of the cerebral cortex. *Nat Rev Neurosci*. doi:10.1038/nrn2402
- Atherton JF, Wokosin DL, Ramanathan S, Bevan MD. 2008. Autonomous initiation and propagation of action potentials in neurons of the subthalamic nucleus. *J Physiol* **586**:5679–5700. doi:10.1113/jphysiol.2008.155861
- Avery RB, Johnston D. 1996. Multiple channel types contribute to the low-voltage-activated calcium current in hippocampal CA3 pyramidal neurons. *J Neurosci* **16**:5567–5582. doi:10.1523/jneurosci.16-18-05567.1996
- Azouz R, Gray CM. 2003. Adaptive coincidence detection and dynamic gain control in visual cortical neurons in vivo. *Neuron* **37**:513–523. doi:10.1016/S0896-6273(02)01186-8
- Azouz R, Gray CM. 2000. Dynamic spike threshold reveals a mechanism for synaptic coincidence detection in cortical neurons in vivo. *Proc Natl Acad Sci U S A* **97**:8110–8115. doi:10.1073/pnas.130200797
- Azouz R, Gray CM. 1999. Cellular mechanisms contributing to response

variability of cortical neurons in vivo. *J Neurosci* **19**:2209–2223.
doi:10.1523/jneurosci.19-06-02209.1999

Badel L, Lefort S, Brette R, Petersen CCH, Gerstner W, Richardson MJE. 2008a. Dynamic I-V Curves Are Reliable Predictors of Naturalistic Pyramidal-Neuron Voltage Traces. *J Neurophysiol* **99**:656–666.
doi:10.1152/jn.01107.2007

Badel Laurent, Lefort Sandrine, Berger Thomas K, Carl ·, Petersen CH, Gerstner W, Richardson Magnus J E, Badel L, Gerstner · W, Berger T K, Lefort S, Petersen · C C H, Richardson M J E. 2008b. Extracting non-linear integrate-and-fire models from experimental data using dynamic I-V curves. *Biol Cybern* **99**:361–370. doi:10.1007/s00422-008-0259-4

Bezanson J, Edelman A, Karpinski S, Shah VB. 2017. Julia: A Fresh Approach to Numerical Computing *. *Soc Ind Appl Math* **59**.
doi:10.1137/141000671

Boucsein C, Tetzlaff T, Meier R, Aertsen A, Naundorf B. 2009. Brief Communications Dynamical Response Properties of Neocortical Neuron Ensembles: Multiplicative versus Additive Noise.
doi:10.1523/JNEUROSCI.3424-08.2009

Brette R. 2013. Sharpness of Spike Initiation in Neurons Explained by Compartmentalization. *PLoS Comput Biol* **9**.
doi:10.1371/journal.pcbi.1003338

Brown DA, Passmore GM. 2009. Neural KCNQ (Kv7) channels. *Br J Pharmacol*. doi:10.1111/j.1476-5381.2009.00111.x

Brunel N, Chance FS, Fourcaud N, Abbott LF. 2001. Effects of synaptic noise and filtering on the frequency response of spiking neurons. *Phys Rev Lett* **86**:2186–2189. doi:10.1103/PhysRevLett.86.2186

Brunel N, Van Rossum MCW. 2007. Lapicque's 1907 paper: From frogs to integrate-and-fire. *Biol Cybern* **97**:337–339. doi:10.1007/s00422-007-0190-0

Carnevale NT, Hines ML. 2006. The NEURON Book. Cambridge University Press. doi:10.1017/CBO9780511541612

Catterall WA. 1981. Localization of sodium channels in cultured neural

- cells. *J Neurosci* **1**:777–783. doi:10.1523/jneurosci.01-07-00777.1981
- Colbert CM, Johnston D. 1996. Axonal action-potential initiation and Na⁺ channel densities in the soma and axon initial segment of subicular pyramidal neurons. *J Neurosci* **16**:6676–86. doi:10.1523/jneurosci.4812-05.2006
- Colbert CM, Pan E. 2002. Ion channel properties underlying axonal action potential initiation in pyramidal neurons. *Nat Neurosci* **5**:533–538. doi:10.1038/nn857
- Coombs JS, Curtis DR, Eccles JC. 1957. The interpretation of spike potentials of motoneurons. *J Physiol* **139**:198–231. doi:10.1113/jphysiol.1957.sp005887
- DeFelipe J. 1999. Chandelier cells and epilepsy. *Brain* **122**:1807–1822. doi:10.1093/brain/122.10.1807
- Dekker JP, Yellen G. 2006. Cooperative Gating between Single HCN Pacemaker Channels. *J Gen Physiol J Gen Physiol* © **128**:561–567. doi:10.1085/jgp.200609599
- Destexhe A, Rudolph M, Paré D. 2003. The high-conductance state of neocortical neurons in vivo. *Nat Rev Neurosci* **4**:739–751. doi:10.1038/nrn1198
- Devaux JJ, Kleopa KA, Cooper EC, Scherer SS. 2004. KCNQ2 Is a Nodal K⁺ Channel. *J Neurosci* **24**:1236–1244. doi:10.1523/JNEUROSCI.4512-03.2004
- Diba K, Koch C, Segev I. 2006. Spike propagation in dendrites with stochastic ion channels. *J Comput Neurosci* **20**:77–84. doi:10.1007/s10870-006-4770-0
- Dodge FA, Cooley JW. 1973. Action potential of the motorneuron. *IBM J Res Dev* **17**:219–229. doi:10.1147/rd.173.0219
- Dodson PD, Barker MC, Forsythe ID. 2002. Two heteromeric Kv1 potassium channels differentially regulate action potential firing. *J Neurosci* **22**:6953–6961. doi:10.1523/jneurosci.22-16-06953.2002
- Druckmann S, Banitt Y, Gidon A, Schürmann F, Markram H, Segev I. 2007. A novel multiple objective optimization framework for constraining conductance-based neuron models by experimental data. *Front*

- Neurosci* **1**:7–18. doi:10.3389/neuro.01.1.1.001.2007
- Eyal G, Mansvelder HD, de Kock CPJ, Segev I. 2014. Dendrites Impact the Encoding Capabilities of the Axon. *J Neurosci* **34**:8063–8071. doi:10.1523/jneurosci.5431-13.2014
- Fatt P. 1957. Sequence of events in synaptic activation of a motoneurone. *J Neurophysiol* **20**:61–80. doi:10.1152/jn.1957.20.1.61
- Fleidervish IA, Lasser-Ross N, Gutnick MJ, Ross WN. 2010. Na⁺ imaging reveals little difference in action potential-evoked Na⁺ influx between axon and soma. *Nat Neurosci* **13**:852–860. doi:10.1038/nn.2574
- Fourcaud-Trocmé N, Hansel D, van Vreeswijk C, Brunel N. 2003. How spike generation mechanisms determine the neuronal response to fluctuating inputs. *J Neurosci* **23**:11628–11640. doi:23/37/11628 [pii]
- Foust A, Popovic M, Zecevic D, McCormick DA. 2010. Action potentials initiate in the axon initial segment and propagate through axon collaterals reliably in cerebellar purkinje neurons. *J Neurosci* **30**:6891–6902. doi:10.1523/JNEUROSCI.0552-10.2010
- Fujiwara-Tsukamoto Y, Isomura Y, Kaneda K, Takada M. 2004. Synaptic interactions between pyramidal cells and interneurone subtypes during seizure-like activity in the rat hippocampus. *J Physiol* **557**:961–979. doi:10.1113/jphysiol.2003.059915
- Fuortes MG, Frank K, Becker MC. 1957. Steps in the production of motoneuron spikes. *J Gen Physiol* **40**:735–752. doi:10.1085/jgp.40.5.735
- Goldberg EM, Clark BD, Zagha E, Nahmani M, Erisir A, Rudy B. 2008. K⁺ Channels at the Axon Initial Segment Dampen Near-Threshold Excitability of Neocortical Fast-Spiking GABAergic Interneurons. *Neuron* **58**:387–400. doi:10.1016/j.neuron.2008.03.003
- Henze DA, Buzsáki G. 2001. Action potential threshold of hippocampal pyramidal cells in vivo is increased by recent spiking activity. *Neuroscience* **105**:121–130. doi:10.1016/S0306-4522(01)00167-1
- Higgs MH, Spain WJ. 2009. Conditional bursting enhances resonant firing in neocortical layer 2-3 pyramidal neurons. *J Neurosci* **29**:1285–1299. doi:10.1523/JNEUROSCI.3728-08.2009

- Hines ML, Carnevale NT. 2001. NEURON: a tool for neuroscientists. *Neuroscientist* **7**:123–35. doi:10.1177/107385840100700207
- Hodgkin AL, Huxley AF. 1952a. The dual effect of membrane potential on sodium conductance in the giant axon of *Loligo*. *J Physiol* **116**:497–506. doi:10.1113/jphysiol.1952.sp004719
- Hodgkin AL, Huxley AF. 1952b. Currents carried by sodium and potassium ions through the membrane of the giant axon of *Loligo*. *J Physiol* **116**:449–472. doi:10.1113/jphysiol.1952.sp004717
- Hodgkin AL, Huxley AF. 1952c. The components of membrane conductance in the giant axon of *Loligo*. *J Physiol* **116**:473–496. doi:10.1113/jphysiol.1952.sp004718
- Hodgkin AL, Huxley AF. 1952d. A quantitative description of membrane current and its application to conduction and excitation in nerve. *J Physiol* **117**:500–544. doi:10.1113/jphysiol.1952.sp004764
- Hodgkin AL, Huxley AF, Katz B. 1952. Measurement of current-voltage relations in the membrane of the giant axon of *Loligo*. *J Physiol* **116**:424–448. doi:10.1113/jphysiol.1952.sp004716
- Hodgkin AL, Katz B. 1949. The effect of temperature on the electrical activity of the giant axon of the squid. *J Physiol* **109**:240–249. doi:10.1113/jphysiol.1949.sp004388
- Hu W, Tian C, Li T, Yang M, Hou H, Shu Y. 2009. Distinct contributions of Nav1.6 and Nav1.2 in action potential initiation and backpropagation. *Nat Neurosci* **12**:996–1002. doi:10.1038/nn.2359
- Ilin V, Malyshev A, Wolf F, Volgushev M. 2013. Fast computations in cortical ensembles require rapid initiation of action potentials. *J Neurosci* **33**:2281–2292. doi:10.1523/JNEUROSCI.0771-12.2013
- Kaplan DM. 2011. Explanation and description in computational neuroscience. *Synthese* **183**:339–373. doi:10.1007/s11229-011-9970-0
- Karagiannis A, Gallopin T, Dávid C, Battaglia D, Geoffroy H, Rossier J, Hillman EMC, Staiger JF, Cauli B. 2009. Classification of NPY-expressing neocortical interneurons. *J Neurosci* **29**:3642–3659. doi:10.1523/JNEUROSCI.0058-09.2009
- Karube F, Kubota Y, Kawaguchi Y. 2004. Axon Branching and Synaptic

- Bouton Phenotypes in GABAergic Nonpyramidal Cell Subtypes. *J Neurosci* **24**:2853–2865. doi:10.1523/JNEUROSCI.4814-03.2004
- Kawaguchi Y, Kubota Y. 1997. GABAergic cell subtypes and their synaptic connections in rat frontal cortex. *Cereb Cortex* **7**:476–486. doi:10.1093/cercor/7.6.476
- Khazen G, Hill SL, Schü Rmann F, Markram H. 2012. Combinatorial Expression Rules of Ion Channel Genes in Juvenile Rat (*Rattus norvegicus*) Neocortical Neurons. *PLoS One* **7**:34786. doi:10.1371/journal.pone.0034786
- Kisvárdy ZF, Martin KA, Whitteridge D, Somogyi P. 1985. Synaptic connections of intracellularly filled clutch cells: a type of small basket cell in the visual cortex of the cat. *J Comp Neurol* **241**:111–37. doi:10.1002/cne.902410202
- Köhler M, Hirschberg B, Bond CT, Kinzie JM, Marrion N V., Maylie J, Adelman JP. 1996. Small-conductance, calcium-activated potassium channels from mammalian brain. *Science (80-)* **273**:1709–1714. doi:10.1126/science.273.5282.1709
- Kole MHP, Hallermann S, Stuart GJ. 2006. Single Ih channels in pyramidal neuron dendrites: Properties, distribution, and impact on action potential output. *J Neurosci* **26**:1677–1687. doi:10.1523/JNEUROSCI.3664-05.2006
- Kole MHP, Ilshner SU, Kampa BM, Williams SR, Ruben PC, Stuart GJ. 2008. Action potential generation requires a high sodium channel density in the axon initial segment. *Nat Neurosci* **11**:178–186. doi:10.1038/nn2040
- Kole MHP, Letzkus JJ, Stuart GJ. 2007. Axon Initial Segment Kv1 Channels Control Axonal Action Potential Waveform and Synaptic Efficacy. *Neuron* **55**:633–647. doi:10.1016/j.neuron.2007.07.031
- Kole MHP, Stuart GJ. 2012. Review Signal Processing in the Axon Initial Segment. doi:10.1016/j.neuron.2012.01.007
- Kole MHP, Stuart GJ. 2008. Is action potential threshold lowest in the axon? *Nat Neurosci* **11**:1253–1255. doi:10.1038/nn.2203
- Köndgen H, Geisler C, Fusi S, Wang XJ, Lüscher HR, Giugliano M. 2008.

The dynamical response properties of neocortical neurons to temporally modulated noisy inputs in vitro. *Cereb Cortex* **18**:2086–2097. doi:10.1093/cercor/bhm235

- Korngreen A, Sakmann B. 2000. Voltage-gated K⁺ channels in layer 5 neocortical pyramidal neurones from young rats: Subtypes and gradients. *J Physiol* **525**:621–639. doi:10.1111/j.1469-7793.2000.00621.x
- Kuba H, Ishii TM, Ohmori H. 2006. Axonal site of spike initiation enhances auditory coincidence detection. *Nature* **444**:1069–1072. doi:10.1038/nature05347
- Kuba H, Ohmori H. 2009. Roles of axonal sodium channels in precise auditory time coding at nucleus magnocellularis of the chick. *J Physiol* **587**:87–100. doi:10.1113/jphysiol.2008.162651
- Larkman AU. 1991. Dendritic morphology of pyramidal neurones of the visual cortex of the rat: I. Branching patterns. *J Comp Neurol* **306**:307–19. doi:10.1002/cne.903060207
- Linaro D, Biró I, Giugliano M. 2018. Dynamical response properties of neocortical neurons to conductance-driven time-varying inputs. *Eur J Neurosci* **47**:17–32. doi:10.1111/ejn.13761
- Lorincz A, Nusser Z. 2010. Molecular identity of dendritic voltage-gated sodium channels. *Science (80-)* **328**:906–909. doi:10.1126/science.1187958
- Maass W, Markram H. 2002. Synapses as dynamic memory buffers. *Neural Networks* **15**:155–161. doi:10.1016/S0893-6080(01)00144-7
- Maass W, Natschläger T, Markram H. 2002. Real-time computing without stable states: A new framework for neural computation based on perturbations. *Neural Comput* **14**:2531–2560. doi:10.1162/089976602760407955
- Magistretti J, Alonso A. 1999. Biophysical properties and slow voltage-dependent inactivation of a sustained sodium current in entorhinal cortex layer-II principal neurons: a whole-cell and single-channel study. *J Gen Physiol* **114**:491–509. doi:10.1085/jgp.114.4.491
- Markram H, Muller E, Ramaswamy S, Reimann MW, Abdellah M, Sanchez

CA, Ailamaki A, Alonso-Nanclares L, Antille N, Arsever S, Kahou GAA, Berger TK, Bilgili A, Buncic N, Chalimourda A, Chindemi G, Courcol JD, Delalondre F, Delattre V, Druckmann S, Dumusc R, Dynes J, Eilemann S, Gal E, Gevaert ME, Ghobril JP, Gidon A, Graham JW, Gupta A, Haenel V, Hay E, Heinis T, Hernando JB, Hines M, Kanari L, Keller D, Kenyon J, Khazen G, Kim Y, King JG, Kisvarday Z, Kumbhar P, Lasserre S, Le Bé JV, Magalhães BRC, Merchán-Pérez A, Meystre J, Morrice BR, Muller J, Muñoz-Céspedes A, Muralidhar S, Muthurasa K, Nachbaur D, Newton TH, Nolte M, Ovcharenko A, Palacios J, Pastor L, Perin R, Ranjan R, Riachi I, Rodríguez JR, Riquelme JL, Rössert C, Sfyarakis K, Shi Y, Shillcock JC, Silberberg G, Silva R, Tauheed F, Telefont M, Toledo-Rodriguez M, Tränkler T, Van Geit W, Díaz JV, Walker R, Wang Y, Zaninetta SM, Defelipe J, Hill SL, Segev I, Schürmann F. 2015. Reconstruction and Simulation of Neocortical Microcircuitry. *Cell* **163**:456–492.
doi:10.1016/j.cell.2015.09.029

Marx SO, Ondrias K, Marks AR. 1995. Coupled Gating Between Individual Skeletal Muscle Ca²⁺ Release Channels (Ryanodine Receptors), Proc. Natl. Acad. Sci. U.S.A.

Meeks JP, Mennerick S. 2007. Action potential initiation and propagation in CA3 pyramidal axons. *J Neurophysiol* **97**:3460–3472.
doi:10.1152/jn.01288.2006

Molina ML, Barrera FN, Ferná Ndez AM, Poveda JA, Renart ML, Encinar JA, Riquelme G, Gonzá Lez-Ros JM. 2006. Clustering and Coupled Gating Modulate the Activity in KcsA, a Potassium Channel Model *.
doi:10.1074/jbc.M600342200

Naundorf B, Geisel T, Wolf F. 2005. Action Potential Onset Dynamics and the Response Speed of Neuronal Populations, *Journal of Computational Neuroscience*.

Naundorf B, Wolf F, Volgushev M. 2006. Unique features of action potential initiation in cortical neurons. *Nature* **440**:1060–1063.
doi:10.1038/nature04610

Öz P, Huang M, Wolf F. 2015. Action potential initiation in a multi-compartmental model with cooperatively gating Na channels in the axon initial segment. *J Comput Neurosci* **39**:63–75.
doi:10.1007/s10827-015-0561-9

- Palmer LM, Clark BA, Gründemann J, Roth A, Stuart GJ, Häusser M. 2010. Initiation of simple and complex spikes in cerebellar Purkinje cells. *J Physiol* **588**:1709–1717. doi:10.1113/jphysiol.2010.188300
- Palmer LM, Stuart GJ. 2006. Site of action potential initiation in layer 5 pyramidal neurons. *J Neurosci* **26**:1854–1863. doi:10.1523/JNEUROSCI.4812-05.2006
- Pan Z, Kao T, Horvath Z, Lemos J, Sul JY, Cranstoun SD, Bennett V, Scherer SS, Cooper EC. 2006. A common ankyrin-G-based mechanism retains KCNQ and Na V channels at electrically active domains of the axon. *J Neurosci* **26**:2599–2613. doi:10.1523/JNEUROSCI.4314-05.2006
- Perrenoud Q, Rossier J, Geoffroy H, Vitalis T, Gallopin T. 2013. Diversity of GABAergic interneurons in layer VIa and VIb of mouse barrel cortex. *Cereb Cortex* **23**:423–41. doi:10.1093/cercor/bhs032
- Peters A, Kaiserman-Abramof IR. 1970. The small pyramidal neuron of the rat cerebral cortex. The perikaryon, dendrites and spines. *Am J Anat* **127**:321–355. doi:10.1002/aja.1001270402
- Popovic MA, Foust AJ, McCormick DA, Zecevic D. 2011. The spatio-temporal characteristics of action potential initiation in layer 5 pyramidal neurons: A voltage imaging study. *J Physiol* **589**:4167–4187. doi:10.1113/jphysiol.2011.209015
- Ramón y Cajal S. Histologie du système nerveux de l’homme & des vertébrés., Histologie du système nerveux de l’homme & des vertébrés. Maloine,. doi:10.5962/bhl.title.48637
- Rettig J, Wunder F, Stocker M, Lichtinghagen R, Mastiaux F, Beckh S, Kues W, Pedarzani P, Schröter KH, Ruppersberg JP. 1992. Characterization of a Shaw-related potassium channel family in rat brain. *EMBO J* **11**:2473–86.
- Reuveni I, Friedman A, Amitai Y, Gutnick MJ. 1993. Stepwise repolarization from Ca²⁺ plateaus in neocortical pyramidal cells: Evidence for nonhomogeneous distribution of HVA Ca²⁺ channels in dendrites. *J Neurosci* **13**:4609–4621. doi:10.1523/jneurosci.13-11-04609.1993
- Ribak CE. 1985. Axon terminals of GABAergic chandelier cells are lost at

epileptic foci. *Brain Res* **326**:251–260. doi:10.1016/0006-8993(85)90034-4

- Schmidt-Hieber C, Bischofberger J. 2010. Fast sodium channel gating supports localized and efficient axonal action potential initiation. *J Neurosci* **30**:10233–10242. doi:10.1523/JNEUROSCI.6335-09.2010
- Schmidt-hieber C, Jonas P, Bischofberger J. 2008. Action potential initiation and propagation in hippocampal mossy fibre axons. *J Physiol* **586**:1849–1857. doi:10.1113/jphysiol.2007.150151
- Shu Y, Duque A, Yu G, Haider B, McCormick DA. 2007a. Properties of action-potential initiation in neocortical pyramidal cells: Evidence from whole cell axon recordings. *J Neurophysiol* **97**:746–760. doi:10.1152/jn.00922.2006
- Shu Y, Hasenstaub A, Badoual M, Bal T, McCormick DA. 2003. Barrages of Synaptic Activity Control the Gain and Sensitivity of Cortical Neurons. *J Neurosci* **23**:10388–10401. doi:10.1523/jneurosci.23-32-10388.2003
- Shu Y, Yu G, Yang J, McCormick DA. 2007b. Selective control of cortical axonal spikes by a slowly inactivating K⁺ current. *Proc Natl Acad Sci U S A* **104**:11453–11458. doi:10.1073/pnas.0702041104
- Somogyi P, Freund TF, Cowey A. 1982. The axo-axonic interneuron in the cerebral cortex of the rat, cat and monkey. *Neuroscience* **7**:2577–2607. doi:10.1016/0306-4522(82)90086-0
- Somogyi P, Tamás G, Lujan R, Buhl EH. 1998. Salient features of synaptic organisation in the cerebral cortex. *Brain Research Reviews*. pp. 113–135. doi:10.1016/S0165-0173(97)00061-1
- Tchumatchenko T, Malyshev A, Wolf F, Volgushev M. 2011. Ultrafast population encoding by cortical neurons. *J Neurosci* **31**:12171–12179. doi:10.1523/JNEUROSCI.2182-11.2011
- Telenczuk M, Fontaine B, Brette R. 2017. The basis of sharp spike onset in standard biophysical models. *PLoS One* **12**:e0175362. doi:10.1371/journal.pone.0175362
- Wang Y, Toledo-Rodriguez M, Gupta A, Wu C, Silberberg G, Luo J, Markram H. 2004. Anatomical, physiological and molecular properties

of Martinotti cells in the somatosensory cortex of the juvenile rat. *J Physiol* **561**:65–90. doi:10.1113/jphysiol.2004.073353

Winnubst J, Bas E, Ferreira TA, Wu Z, Economo MN, Edson P, Arthur BJ, Bruns C, Rokicki K, Schauder D, Olbris DJ, Murphy SD, Ackerman DG, Arshadi C, Baldwin P, Blake R, Elsayed A, Hasan M, Ramirez D, Dos Santos B, Weldon M, Zafar A, Dudman JT, Gerfen CR, Hantman AW, Korff W, Sternson SM, Spruston N, Svoboda K, Chandrashekar J. 2019. Reconstruction of 1,000 Projection Neurons Reveals New Cell Types and Organization of Long-Range Connectivity in the Mouse Brain. *Cell* **179**:268–281.e13. doi:10.1016/j.cell.2019.07.042

Wilent WB, Contreras D. 2005. Stimulus-dependent changes in spike threshold enhance feature selectivity in rat barrel cortex neurons. *J Neurosci* **25**:2983–2991. doi:10.1523/JNEUROSCI.4906-04.2005

Wollner DA, Catterall WA. 1986. Localization of sodium channels in axon hillocks and initial segments of retinal ganglion cells. *Proc Natl Acad Sci U S A* **83**:8424–8428. doi:10.1073/pnas.83.21.8424

Yu Y, Shu Y, McCormick DA. 2008. Cortical Action Potential Backpropagation Explains Spike Threshold Variability and Rapid-Onset Kinetics. *J Neurosci* **28**:7260–7272. doi:10.1523/JNEUROSCI.1613-08.2008

Yuste R. 2005. Origin and classification of neocortical interneurons. *Neuron* **48**:524–7. doi:10.1016/j.neuron.2005.11.012

CHAPTER 2

Research goals

This thesis is focused on single cell computer models. First, I will investigate human neurons with respect to their information transfer properties. Second, I investigate a large public repository of model rat neocortex neurons. I will use this repository to investigate the excitability and transfer properties of these neurons. Lastly, I investigate layer 1 inhibitory neurons, comparing experimental results with computer simulations. Not only validating a public repository of modelled neurons but also gathering new insights on the information processing capabilities of layer 1 interneurons.

2.1 What are the cellular correlates of IQ?

Human intelligence is often linked to the ability to process information, how efficiently this is done and how well fast varying information can be processed. It is important to understand where our intelligence originates from. As it could help not only to remedy cognitive diseases but also to provide a better understanding of how a neuronal network can perform certain tasks. In chapter 3, “Large and fast human pyramidal neurons associate with intelligence”, we investigate human neurons, using the patch clamp technique on slices to characterize the properties of action potentials. Furthermore, computer models are constructed from the original neuronal cells. These models are used to investigate, *in silico*, the transfer properties of the neuron. All obtained parameters, the action potential parameters and transfer properties, are linked to the IQ of the individual.

My contribution for this paper has been single cell simulation and the analysis of this data.

2.2 What influences the information capabilities of excitatory neurons?

Recently a new method of probing neurons has been introduced. Classically neurons are probed by constant current pulses injected into the soma,

resulting in a frequency versus current curve. This new protocol is based on a random fluctuating current to probe the neuronal response, not a constant current. The benefit of this is that the response of the neuron is biologically more realistic than when it is probed by a constant current waveform. Additionally, on top of the random fluctuating current there is a signal, typically a sine. With this method it is possible to probe the neuron's ability to process and transfer information. In chapter 4, "The location of the axon initial segment affects the bandwidth of spike initiation dynamics", we combine this novel probing method together with a new theory about the sharpness of action potentials at the soma. We perform a very detailed study on how this theory can affect the information flow from neuron to neuron. I am a first author for this paper, performing all the single cell simulations, analysing the data and writing the manuscript.

2.3 How do diverse layer 1 inhibitory neurons transfer information?

When neurons are injected, at their soma, with a constant current, it is known that they respond by diverse firing patterns, as discussed in the introduction. However, the purpose of this diversity still needs to be elucidated. Layer 1 inhibitory neurons are underrepresented in both *in vitro* and *in silico* studies. Transfer and information processing properties of these neurons still has to be investigated. Determining how L1 interneurons process information is vital, since they play a crucial role in the top-down information pipeline. Thus, their behaviour determines the performance of the layer 5 pyramidal neurons that receive their input from these L1 interneurons. It is known that these L1 inhibitory neurons exhibit a broad range of firing types. In chapter 5, "Homogeneous and narrow bandwidth of spike initiation in rat L1 cortical interneurons", we investigated whether it is possible to cluster these L1 inhibitory neurons according to their action potential properties with respect to the firing patterns they exhibit. Furthermore, we investigate the transfer properties of these L1 neurons, to determine whether they're significantly different from for example the L5 excitatory neurons they direct their output towards. By combining both *in vitro* experiments and *in silico* simulations we perform a one of a kind study of the properties of L1 interneurons, not

only confirming the model's validity against these novel protocols but also increasing the knowledge of how information integration and processing is performed by L1 interneurons. I am a shared first author for this paper. I performed the single cell simulations, analysed the data and wrote the manuscript.

CHAPTER 3

Large and fast human pyramidal neurons
associate with intelligence

eLife, 2018

3.1 Chapter information

3.1.1 Publication

Natalia A Goriounova, Djai B Heyer, René Wilbers, Matthijs B Verhoog, Michele Giugliano, **Christophe Verbist**, Joshua Obermayer, Amber Kerkhofs, Harriët Smeding, Maaïke Verberne, Sander Idema, Johannes C Baayen, Anton W Pieneman, Christiaan PJ de Kock, Martin Klein, Huibert D Mansvelder, eLife 2018;7:e41714.

3.1.2 Author contribution

Natalia A Goriounova, Conceptualization, Formal analysis, Funding acquisition, Investigation, Visualization, Methodology, Writing—original draft, Writing—review and editing; Djai B Heyer, René Wilbers, Christophe Verbist, Software, Formal analysis; Matthijs B Verhoog, Software, Investigation; Michele Giugliano, Conceptualization, Software, Formal analysis, Methodology; Joshua Obermayer, Amber Kerkhofs, Harriët Smeding, Maaïke Verberne, Sander Idema, Johannes C Baayen, Anton W Pieneman, Investigation; Christiaan PJ de Kock, Formal analysis, Investigation; Martin Klein, Conceptualization, Investigation; Huibert D Mansvelder, Conceptualization, Supervision, Funding acquisition, Writing—original draft, Project administration, Writing—review and editing

3.2 Abstract

It is generally assumed that human intelligence relies on efficient processing by neurons in our brain. Although grey matter thickness and activity of temporal and frontal cortical areas correlate with IQ scores, no direct evidence exists that links structural and physiological properties of neurons to human intelligence. Here, we find that high IQ scores and large temporal cortical thickness associate with larger, more complex dendrites of human pyramidal neurons. We show *in silico* that larger dendritic trees enable pyramidal neurons to track activity of synaptic inputs with higher temporal precision, due to fast action potential kinetics. Indeed, we find that human pyramidal neurons of individuals with higher IQ scores sustain fast action potential kinetics during repeated firing. These findings provide the first evidence that human intelligence is associated with neuronal complexity, action potential kinetics and efficient information transfer from inputs to output within cortical neurons.

3.3 Introduction

A fundamental question in neuroscience is what properties of neurons lie at the heart of human intelligence and underlie individual differences in mental ability. Thus far, experimental research on the neurobiological basis of intelligence has largely ignored the neuronal level and has not directly tested what role human neurons play in cognitive ability, mainly due to the inaccessibility of human neurons. Instead, research has either been focused on finding genetic loci that can explain part of the variance in intelligence (Spearman's g) in large cohorts (Coleman et al., 2019; Lam et al., 2017; Sniekers et al., 2017; Trampush et al., 2017) or on identifying brain regions in whole brain imaging studies of which structure or function correlate with IQ scores (Deary et al., 2010; Karama et al., 2009; McDaniel, 2005; Narr et al., 2007; Pol et al., 2006). Some studies have highlighted that variability in brain volume and intelligence may share a common genetic origin (Pol et al., 2006; Posthuma et al., 2002; Sniekers et al., 2017), and individual genes that were identified as associated with IQ scores might aid intelligence by facilitating neuron growth (Coleman et al., 2019; Sniekers et al., 2017) and directly influencing neuronal firing (Lam et al., 2017).

Intelligence is a distributed function that depends on activity of multiple brain regions (Deary et al., 2010). Structural and functional magnetic resonance imaging studies in hundreds of healthy subjects revealed that cortical volume and function of specific areas correlate with g (Choi et al., 2008; Karama et al., 2009; Narr et al., 2007). In particular, areas located in the frontal and temporal cortices show multiple correlations of grey matter thickness and functional activation with IQ scores: individuals with high IQ show larger grey matter volume of, for instance, Brodmann areas 21 and 38 (Choi et al., 2008; Deary et al., 2010; Karama et al., 2009; Narr et al., 2007). Cortical grey matter consists for a substantial part of dendrites (Chklovskii et al., 2002; Ikari and Hayashi, 1981), which receive and integrate synaptic information and strongly affect functional properties of neurons (Bekkers and Häusser, 2007; G. Eyal et al., 2014; Vetter et al., 2001). Especially higher order association areas in temporal and frontal lobes in humans harbor pyramidal neurons of extraordinary dendritic size and complexity (Elston, 2003; Mohan et al., 2015) that may constitute variation in cortical thickness, neuronal function, and ultimately IQ. These neurons and their connections form the principal building blocks for coding, processing, and information storage in the brain and give rise to cognition (Salinas and Sejnowski, 2001). Given their vast number in the human neocortex, even the slightest change in efficiency of information transfer by neurons may translate into large differences in mental ability. However, whether and how the activity and dendritic structure of single human neurons support human intelligence has not been tested.

To investigate whether structural and functional properties of neurons of the human temporal cortex associate with general intelligence, we collected a unique multimodal data set from 46 human subjects containing single cell physiology (31 subjects, 129 neurons), neuronal morphology (25 subjects, 72 neurons), pre-surgical MRI scans and IQ test scores (35 subjects, Figure 3.1, data available at the Dryad Digital Repository:

<https://doi.org/10.5061/dryad.83dv5j7>).

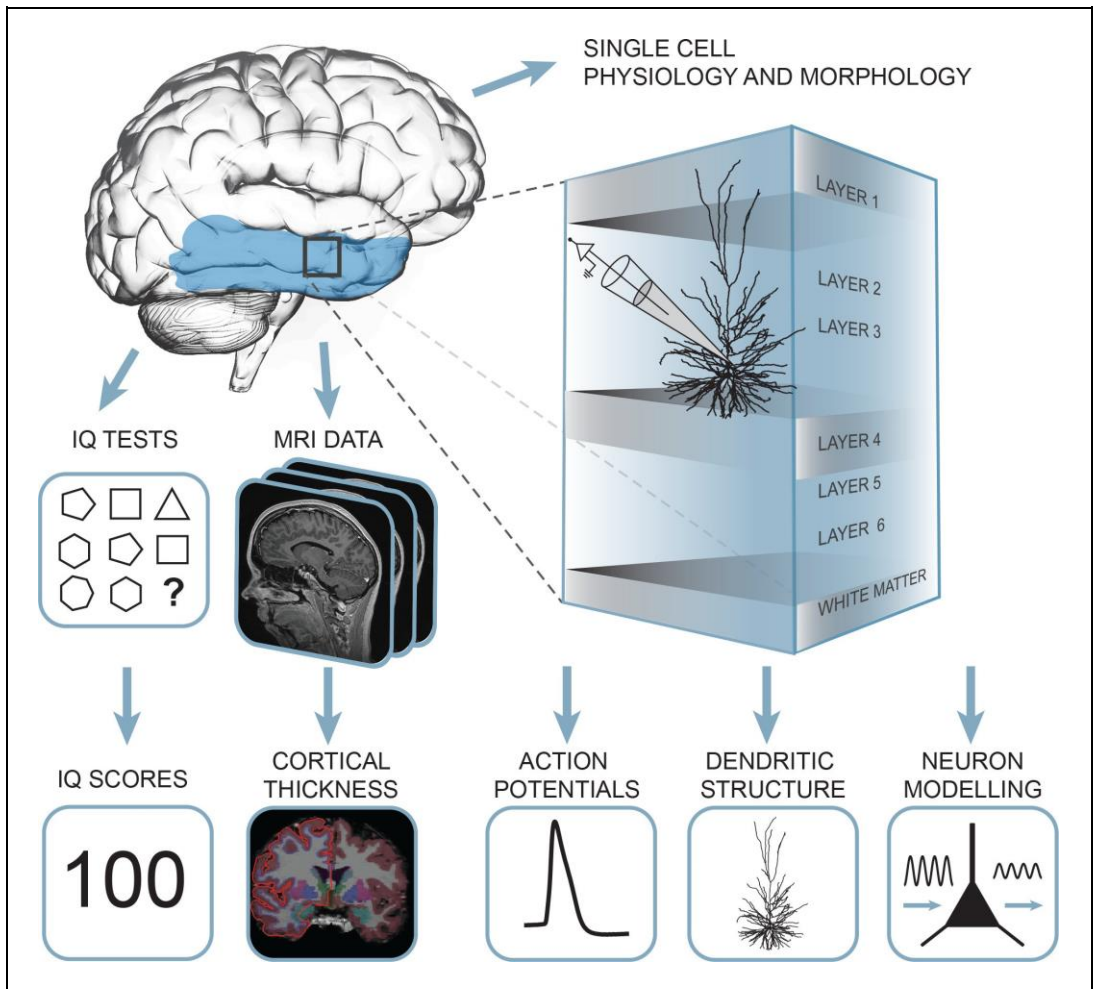


Figure 3.1. Summary of the approach: multidimensional data set from human subjects contained single cell physiology, neuronal morphology, MRI and IQ test scores (WAIS FSIQ). The area of the brain highlighted in blue indicates the location of cortical thickness measurements, black square indicates the typical origin of resected cortical tissue. DOI: <https://doi.org/10.7554/eLife.41714.003> The following figure supplements are available for figure 1: Figure supplement 1. Subject disease history and age do not correlate with IQ and neuronal morphology. DOI: <https://doi.org/10.7554/eLife.41714.004> Figure supplement 2. Neuronal morphology, IQ or AP rise speed are not different across patient groups. DOI: <https://doi.org/10.7554/eLife.41714.005>

Human cortical brain tissue was removed as a part of surgical treatment for epilepsy or tumor (Table 3.1). The tissue almost exclusively originated from middle temporal gyrus, approximately 4 cm posterior to the temporal pole (Figure 3.2b) as a block of ~1–1.5 cm in diameter and was removed to gain

access to the disease focus in deeper lying structures such as hippocampus or amygdala. In all patients, the resected neocortical tissue was not part of the epileptic focus or tumor and displayed no structural/functional abnormalities in preoperative MRI investigation, electrophysiological whole cell recordings or microscopic investigation of histochemically stained tissue (Mohan et al., 2015; Testa-Silva, 2010; Testa-Silva et al., 2014; Verhoog et al., 2016, 2013). In line with the non-pathological status of tissue, we observed no correlations of cellular parameters or IQ scores with the subject’s disease history and age (Figure 3.1—figure supplements 1–2). After resection the tissue was immediately placed in ice-cold artificial cerebro-spinal fluid (aCSF) and within 15 min transported to the lab, sliced and maintained to enable single cell physiological recordings and biocytin filling.

We recorded action potentials (APs) from human pyramidal neurons in superficial layers of temporal cortex and digitally reconstructed their complete dendritic structures. We tested the hypothesis that variation in neuronal morphology can lead to functional differences in AP speed and information transfer and explain variation in IQ scores. In addition to our experimental results, we used computational modelling to understand underlying principles of efficient information transfer in human cortical neurons.

Patient number	IQ	Age	Diagnosis	Gender	Antiepileptic drugs
1	88	41	Tumor	M	CBZ
2	78	21	Other	F	LEV; VPA
3	119	66	Tumor	F	None
4	88	31	Tumor	F	CBZ; LEV
5	81	51	Other	F	CLB; LTG; OXC
6	69	58	MTS	F	CZP
7	107	28	Tumor	M	LTG; LEV
8	115	29	MTS	F	LTG; TPM
9	125	20	Tumor	M	CBZ; LEV
10	84	27	Tumor	F	CBZ; LTG
11	110	41	Tumor	M	CBZ; LTG
12	87	18	MTS	M	OXC
13	67	23	MTS	F	LEV; OXC

14	72	53	MTS	M	CBZ; CLB
15	97	25	Tumor	M	None
16	104	19	Other	M	CLB; OXC
17	88	48	Other	F	CBZ
18	65	38	MTS	F	CBZ; LEV
19	62	40	Other	F	None
20	84.5	31	Other	F	None
21	88	35	Other	F	CZP; LCS; LTG; LEV
22	77	54	Tumor	M	VPA
23	91	25	Other	M	CLB; LCS; LEV
24	70	31	MTS	F	CBZ; CLB
25	114	49	Other	M	CLB; LCS; LEV
26	83	25	Tumor	M	None
27	109	45	Other	F	CBW; CLB; LTG
28	102	47	Tumor	F	CBZ
29	67	22	Other	M	CLB; LTG; LEV
30	97	38	MTS	M	CBZ
31	79	40	MTS	F	CBZ; CLB; LTG; LEV
32	117	44	Other	M	LCS; VPA
33	99	30	Tumor	F	CLB; OXC
34	72	44	MTS	M	LTG; LEV
35	82	41	Other	F	CBZ; LEV; TPM
36	95	29	Other	M	CBP; PB
37	91	20	Other	F	CBZ; LEV
38	82	21	Tumor	M	CBZ; LCS; LTG; LEV
39	115	40	MTS	M	CBZ; LEV
40	97	48	MTS	F	CBZ; ZNS
41	94	40	MTS	F	CBZ; LTG; ZNS
42	81	44	MTS	M	CBZ; LTG
43	70	33	MTS	F	CBZ; CLB; LEV
44	82	51	Other	M	CBZ
45	114	18	Tumor	F	OXC
46	90	23	Other	M	OXC

Table 3.1. Subject details.

M = male; F = female;

Antiepileptic drugs specified: Carbamazepine (CBZ); Lamotrigine (LTG); Levetiracetam (LEV); Topiramate (TPM); Clobazam (CLB); Oxcarbazepine (OXC); Clonazepam (CZP); Phenobarbital (PB); Phenytoin (PHT); Lacosamide (LCS); Sodium valproate (VPA); Zonisamide (ZNS)

DOI: <https://doi.org/10.7554/eLife.41714.007>

3.4 Results

3.4.1 IQ scores positively correlate with cortical thickness of the temporal lobe

Cortical thickness of the temporal lobe has been associated with IQ scores in hundreds of healthy subjects (Choi et al., 2008; Deary et al., 2010; Karama et al., 2009; Narr et al., 2007; Pol et al., 2006), and we first asked whether this applies to the subjects in our study as well. From T1-weighted MRI scans obtained prior to surgery, we determined temporal cortical thickness in 35 subjects using voxel-based morphometry of temporal cortical areas. These areas included the surgically resected cortical tissue (Figure 3.2b) used for cellular recordings and neuronal reconstructions, which typically came from locations at 4 cm from temporal pole and was 1–1.5 cm in diameter (black circle in Figure 3.2b). The total resected cortical area varied for each patient, but consisted of a larger part of the temporal lobe (Figure 3.2b; average resected area in red, maximum in orange). The mean distance of resection boundaries from temporal pole was 4.2 ± 1.7 cm on superior temporal gyrus, 4.8 ± 1.5 cm on middle temporal gyrus, and 4.9 ± 1.5 cm on inferior temporal gyrus for the 46 subjects in this study. In MRI images, cortical thickness was measured in temporal lobe that included the resection areas and corresponded to the areas identified to associate with IQ in healthy subjects (Choi et al., 2008; Deary et al., 2010; Karama et al., 2009; Narr et al., 2007; Pol et al., 2006) (Figure 3.2c; in red). The superior temporal gyrus was excluded from this analysis as it contains areas for auditory, gustatory and language processing that are spared during resection. Cortical thickness measurements were collapsed to one mean value for cortical thickness for each subject. In line with findings in healthy subjects (Choi et al., 2008; Deary et al., 2010; Karama et al., 2009; Narr et al., 2007; Pol et al., 2006) mean cortical thickness in temporal lobes positively correlated with IQ scores of the subjects (Figure 3.2d).

3.4.2 IQ scores positively correlate with dendritic structure of temporal cortical pyramidal neurons

Cortical association areas in temporal lobes play a key role in high-level integrative neuronal processes and its superficial layers harbor neurons of increased neuronal complexity (DeFelipe et al., 2002; Elston, 2003; Scholtens et al., 2014; van den Heuvel et al., 2015). In rodents, the neuropil of cortical association areas consists for over 30% of dendritic structures (Ikari and Hayashi, 1981). To test the hypothesis that human temporal cortical thickness is associated with dendrite size, we used 72 full reconstructions of biocytin-labelled temporal cortical pyramidal neurons from layers 2, 3 and 4 (median number of neurons per subject = 2; average 2.8; ranging from 1 to 10) part of which was previously reported (Mohan et al., 2015). We calculated total dendritic length (TDL) that included all basal and apical dendrites without apparent slice artifacts for each neuron. We computed TDL from multiple neurons for each subject and correlated these mean TDL values to mean temporal cortical thickness from the same subject.

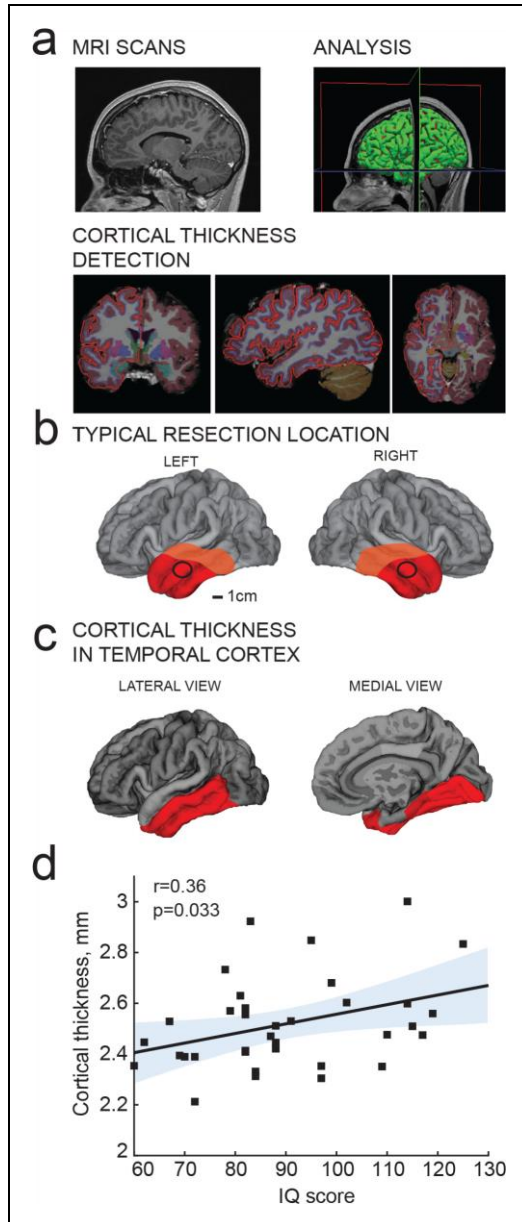


Figure 3.2. IQ scores positively correlate with cortical thickness of the temporal lobe. (a) MRI analysis pipeline: (1) Presurgical MRI T1-weighted scans; (2) Morphometric analysis; (3) Detection of cortical thickness from pial and white-grey matter boundaries; (b) Typical resection location for tissue used in this study is marked by a black circle; average total resected area from the patient is shown in red and maximum resected area in orange; (c) selection of temporal cortical area for correlations with IQ in b (red). (d) Average cortical thickness in temporal lobe (from area highlighted in red in c) positively correlates with IQ scores from the same subjects (n subjects = 35). Here and in figures below, Pearson correlation coefficients and p-values are reported in graph insets, the solid line represents linear regression ($R^2 = 0.13$), shaded area indicates 95% confidence bounds of the fit. DOI: <https://doi.org/10.7554/eLife.41714.006>

We found that dendritic length positively correlated with mean temporal lobe cortical thickness (Pearson correlation coefficient $r = 0.5$, explained variance $R^2 = 0.25$), indicating that dendritic structure of individual neurons contributes to the overall cytoarchitecture of temporal cortex (Figure 3.3a). TDL is in part determined by the soma location within cortical layers: cell bodies of pyramidal neurons with larger dendrites typically lie deeper, at larger distance from pia (Mohan et al., 2015). To exclude a systematic bias in sampling, we determined the cortical depth of each neuron relative to the subject's temporal cortical thickness in the same hemisphere. There was no correlation between IQ score and relative cortical depth of pyramidal neurons indicating that we sampled neurons at similar depths across subjects (Figure 3.3b). Finally, we tested whether mean TDL and complexity of pyramidal neurons relates to subjects' IQ scores. We found a strong positive correlation between individual's pyramidal neuron TDL and IQ scores (Pearson correlation coefficient $r = 0.51$, explained variance $R^2 = 0.26$; Figure 3.3c) as well as between number of dendritic branch points and IQ scores ($r = 0.46$, $R^2 = 0.22$; Figure 3.3d). Thus, larger and more complex pyramidal neurons in temporal association area may partly contribute to thicker cortex and link to higher intelligence.

3.4.3 Larger dendrites lead to faster AP onset and improved encoding properties

Dendrites not only receive most synapses in neurons, but dendritic morphology and ionic conductances act in concert to regulate neuronal excitability (Bekkers and Häusser, 2007; Guy Eyal et al., 2014; Vetter et al., 2001). In model simulations where neurons are reduced to balls and sticks, increasing the dendritic membrane surface area, that is the dendritic impedance load, speeds up the onset phase of APs. This is a consequence of the decrease in the effective time constants of the neuron with increasing dendritic size and dendritic impedance load (Guy Eyal et al., 2014). Larger dendrites act as a larger sink for currents generated in the axon initial segment during AP onset and result in faster membrane potential changes. Furthermore, we found previously that human neocortical pyramidal neurons, which are three times larger than rodent pyramidal neurons (Mohan

et al., 2015), have faster AP onsets compared to rodent neurons and are able to track and encode fast synaptic inputs and sub-threshold changes in membrane potential with high temporal precision (Testa-Silva et al., 2014). We asked whether the observed differences in TDL between human pyramidal neurons affected their encoding properties and ability to transfer information. To this end, we incorporated the 3-dimensional dendritic reconstructions of the 72 human pyramidal neurons into *in silico* models, equipped them with excitable properties (see Materials and methods) and tested whether their APs have faster onset. We found that TDL of model neurons with realistic dendritic trees positively correlated with the steepness of AP onsets ($r = 0.4$, $R^2 = 0.16$; Figure 3.4a,b) and larger dendrites enabled neurons to generate faster APs.

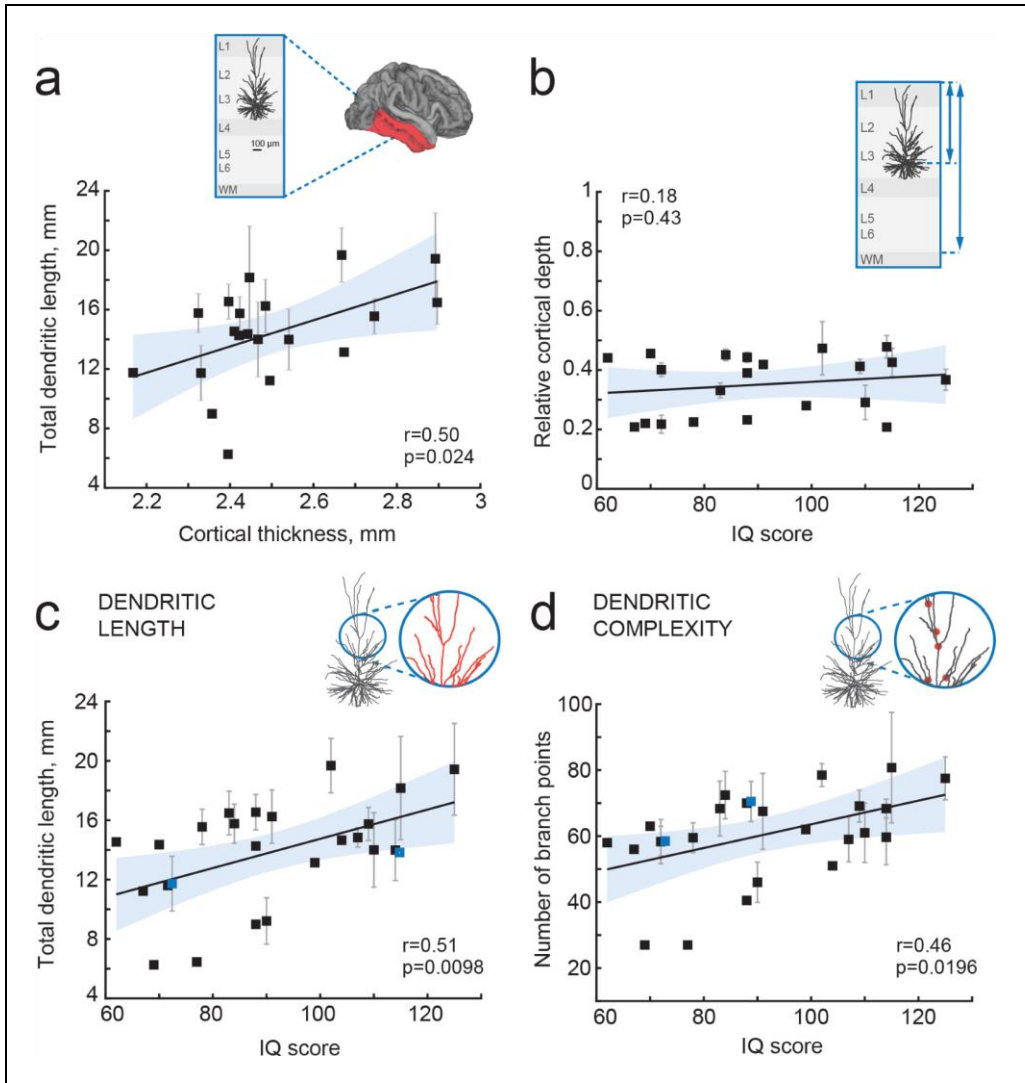


Figure 3.3. IQ scores positively correlate with dendritic structure of temporal cortical pyramidal cells. (a) Average total dendritic length in pyramidal cells in superficial layers of temporal cortex positively correlates with cortical thickness in temporal lobe from the same hemisphere (area shaded in a, n subjects = 20; n neurons = 57, $R^2 = 0.25$). Inset shows a scheme of cortical tissue with a digitally reconstructed neuron and the brain area for cortical thickness estimation (red) (b) Cortical depth of pyramidal neurons, relative to cortical thickness in temporal cortex from the same hemisphere, does not correlate with IQ score (n subjects = 21, $R^2 = 0.03$). Inset represents the cortical tissue, blue lines indicate the depth of neuron and cortical thickness (c) Total dendritic length (TDL) and (d) number of dendritic branches positively correlate with IQ scores from the same individuals (n subjects = 25, n neurons = 72, TDL $R^2 = 0.26$, Branch points $R^2 = 0.22$). Symbols highlighted in blue were shifted along the x axis for display purposes. Data are mean per subject \pm standard deviation. DOI: <https://doi.org/10.7554/eLife.41714.008>

The exact timing of action potential firing allows cortical neurons to pass on temporal information provided by synaptic inputs (Ilin et al., 2013; Köndgen et al., 2008; Linaro et al., 2018; Testa-Silva et al., 2014). Single pyramidal neurons do not sustain high frequency firing and generally do not encode high frequency synaptic input content in rate coding. Instead, the precision in timing of AP initiation does allow these neurons to encode incoming high frequency information in their output. In contrast to rodent neurons, human neurons can encode sub-threshold membrane potential changes on a sub-millisecond timescale by timing of APs (Testa-Silva et al., 2014). This synaptic input tracking capacity strongly relies on the rapidity of AP onset (Ilin et al., 2013). Faster APs allow neurons to respond to fast synaptic inputs, which will be missed if AP generation is too slow. Thereby, neurons with faster APs can translate higher frequencies of synaptic membrane potential fluctuations into AP timing and ultimately encode more information.

The aforementioned theoretical work (Guy Eyal et al., 2014) using ‘ball-and-stick’ neuron models showed that neurons with larger dendritic compartments not only have faster AP onset rapidity, but could also time AP generation to faster changes in membrane potentials, increasing the frequency tracking capabilities of input modulations, and augmenting the input frequency bandwidth of information encoding about three times. However, it is not known whether the same effect holds true for the human cortical pyramidal neurons we recorded from, and whether the range of dendritic compartment sizes we examined might lead to significant quantitative biophysical differences. We tested this by simulating sinusoidal current inputs of increasing frequencies into *in silico* representations of the neurons we recorded and reconstructed, and studied how the timing of AP firing of these neurons followed sub-threshold membrane potential changes. We find that human neurons with larger TDL can reliably time their APs to faster membrane potential changes, with cut-off frequencies up to 400–500 Hz, while smaller neurons had their cut-off frequencies already at 200 Hz (Figure 3.4c,d). Furthermore, there was a significant positive correlation between the dendritic length and the cut-off frequency (Figure 3.4d). Finally, given the same input - composed of the sum of three sinusoids of increasing frequencies - larger neurons were able to better encode rapidly changing temporal information into timing of AP firing, compared to smaller neurons

(Figure 3.4e). Thus, we find that differences in dendritic length of human neurons lead to faster APs and thereby to wider frequency bandwidths of encoding synaptic inputs into timing of AP output.

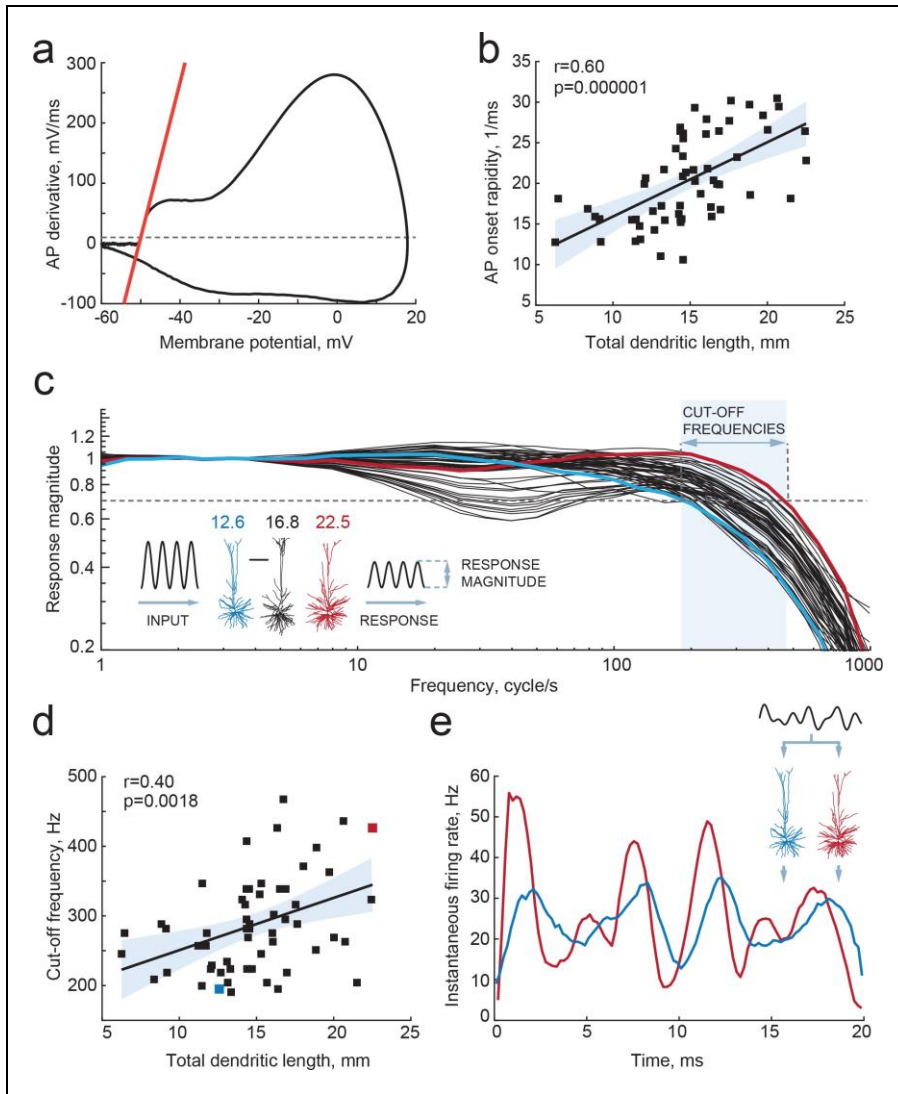


Figure 3.4. Larger dendrites lead to faster AP onset and improved encoding properties. (a-b) Higher TDL results in faster onsets of model-generated APs: (a) example phase plot of an AP is shown with a red line representing onset rapidity - slope of AP derivative at 10 mV/ms (grey dashed line); (b) onset rapidity values of simulated APs positively correlate with TDL ($R^2 = 0.36$). (c) Model neurons received simulated sinusoidal current-clamp inputs and generated spiking responses of different magnitudes and frequencies. Red and blue traces are response magnitudes of example neurons with low (blue) and large (red) TDLs; inset shows examples of morphological reconstructions with their TDLs in mm shown above. Cut-off frequencies are defined within the frequency range (shaded area) at which the model neuron can still track the inputs reliably (produce response of 0.7 response

magnitude, dashed line). (d) Cut-off frequencies positively correlate with TDL ($R^2 = 0.16$; example neurons from panel (c) are highlighted by the same colors). (e) Responses to the same input in two example neurons from panels (b) and (c): instantaneous firing frequency of the model neuron with large TDL (red) follows the input with higher temporal precision than the model neuron with smaller TDL (blue). DOI: <https://doi.org/10.7554/eLife.41714.009>

3.4.4 Higher IQ scores associate with faster Aps

Since cortical pyramidal neurons with large dendrites have faster APs and can encode more information in AP output, and since large dendrites also associate with higher IQ scores, we next asked whether human cortical pyramidal neurons from individuals with higher IQ scores generate faster APs. To test this, we made whole-cell recordings from pyramidal cells in acute slices of temporal cortex (31 subjects, 129 neurons, median number of neurons per subject = 3; ranging from 1 to 11 Figure 3.5) and recorded APs at different firing frequencies in response to depolarizing current steps. We determined AP maximum rise speed, which is highly correlated with AP onset rapidity ($r = 0.79$ $p=4.29e-14$, $n = 60$, data not shown), and can more reliably be determined from recordings with sampling frequencies between 10 and 50 kHz. Maximum rise speed of APs depended on the firing history of the cell, with the first AP in the train having the highest AP rise speed and slowing down with increasing instantaneous firing frequency, the time interval between subsequent APs (Figure 3.5b–d). To test whether AP rise speed differed between IQ groups, we split all AP rise speed data into two groups based on IQ score – above and below 100. Although the AP rise speed of the first AP was not different between high and low IQ groups (Figure 3.5c), the AP slowed down stronger in individuals with lower IQ scores compared to APs of individuals with higher IQ scores (Figure 3.5d). At higher instantaneous firing frequencies (20–40 Hz), the AP rise speed was higher in individuals with IQ scores above 100 (Figure 3.5c right; AP rise speed high IQ = 338.4 ± 26.03 mV/ms; AP rise speed low IQ = 268.1 ± 12.20 mV/ms, t -test $p=0.0113$). We next calculated the slowing of APs with increasing instantaneous frequency by normalizing rise speed of APs to the rise speed of the first AP in the train. Relative to first AP, rise speed at 20–40 Hz showed significant slowing in subjects with lower IQ scores and decreased to 74% of the initial AP rise speed. In contrast, in neurons from individuals with higher IQ scores, AP rise speed remained on average at 84%

(Figure 3.5d right, high IQ = 0.84 ± 0.014 ; low IQ = 0.74 ± 0.024 , t-test p value=0.037).

We further investigated whether these differences at the group level reflected correlations between individual IQ scores and AP rise speeds. We correlated mean AP rise speeds both of the first AP and AP at 20–40 Hz from all neurons of the same subject to the subject's IQ score. The AP rise speed of the first AP in the train positively correlated with IQ scores ($r = 0.41$, $R^2 = 0.17$; Figure 3.5e), and this correlation was even stronger for AP rise speeds at instantaneous frequencies of 20–40 Hz ($r = 0.46$, $R^2 = 0.21$; Figure 3.5f). Importantly, also relative AP values showed significant positive correlations with IQ, indicating that it is the relative slowing of APs at high frequencies that associates with intelligence ($r = 0.37$, $R^2 = 0.14$; Figure 3.5g). Finally, we asked whether the slowing of APs relates to the dendritic size of the same neurons, as our model results suggest. We find that larger neurons show less slowing of AP rise speed (higher relative AP speeds) at 20–40 Hz ($r = 0.55$, $R^2 = 0.30$; Figure 3.5h). These findings reveal that higher IQ scores are accompanied by faster APs during repeated AP firing, while lower IQ scores associate with increased AP fatigue during elevated neuronal activity. Thus, neurons from individuals with higher IQ scores are better equipped to process synaptic signals at high rates and at faster time scales, which is necessary to encode large amounts of information accurately and efficiently.

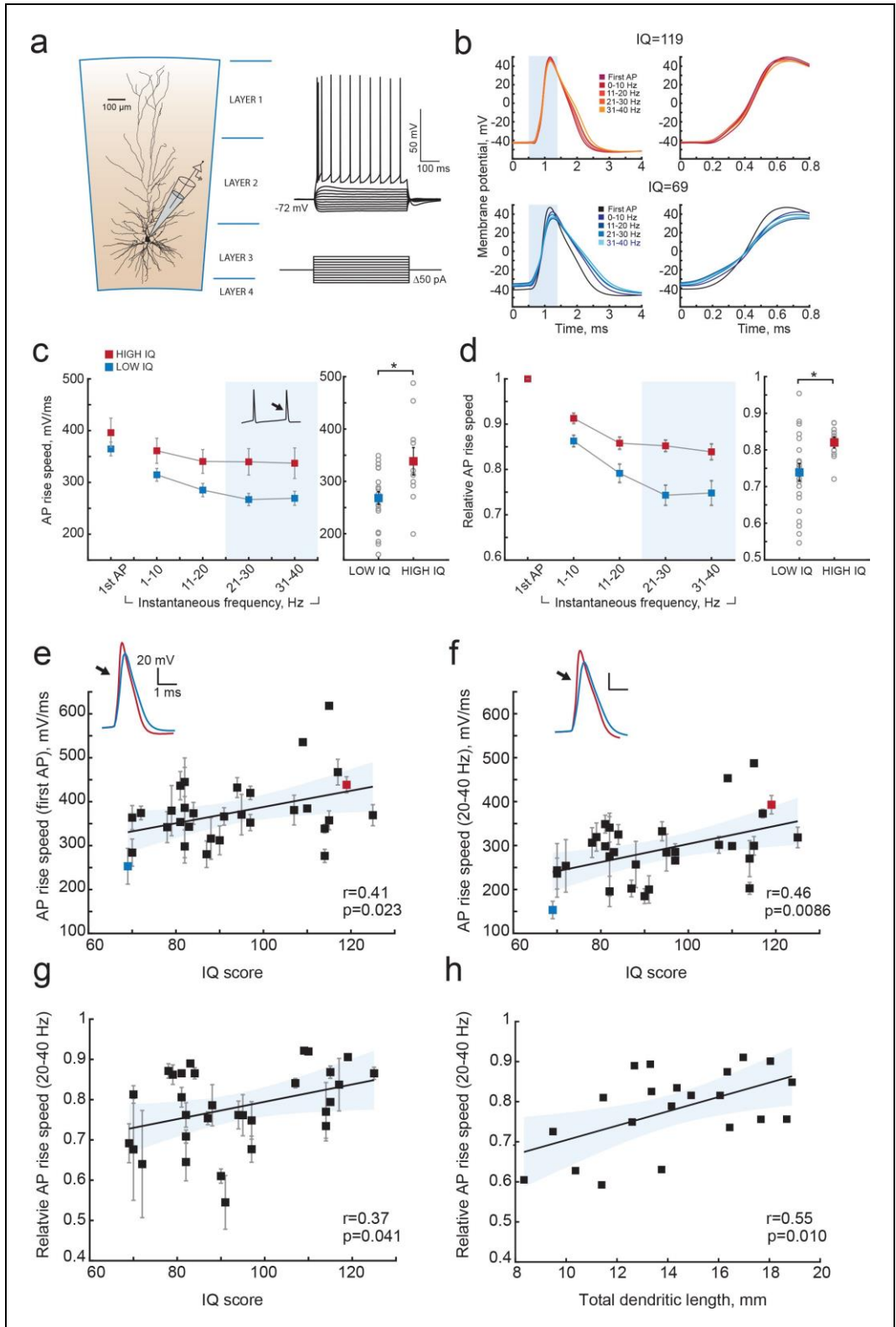


Figure 3.5. Higher IQ scores associate with faster AP initiation. (a) Scheme of a whole-cell recording showing biocytin reconstruction of a pyramidal neuron from human temporal cortex. Right: typical voltage responses to depolarizing somatic current injections. (b) Examples of AP traces at increasing instantaneous firing frequencies (frequency is shown in color code in insets) recorded from a subject with IQ = 119 (above panel, red) and a subject with IQ = 69 (lower panel, blue). AP rising phase in shaded area is displayed to the right (c) APs from subjects with higher IQ are better able to maintain their rise speed at increasing frequencies. Average (per neuron and subject) AP rise speed and (d) relative to first AP rise speeds in neurons from subjects with IQ < 100 (red, n subjects = 21, n neurons = 91) and subjects with IQ > 100 (blue, n subjects = 10, n neurons = 38) are displayed against instantaneous firing frequency. Right: data points in shaded area are shown as averaged values for 20–40 Hz (filled squares are group means, open circles are mean rise speeds per subject), *p<0.05. (e) IQ scores positively correlate with the rise speeds of first AP in the train (n subjects 31, n neurons = 129; $R^2 = 0.17$), (f) AP rise speed at 20–40 Hz (same data as right panel in (c), $R^2 = 0.21$) and (g) relative AP rise speeds at 20–40 Hz (same data as right panel in (d), $R^2 = 0.14$). (h) Larger neurons show less slowing of AP rise speed at higher frequencies: relative AP rise speeds at 20–40 Hz for individual neurons are plotted as a function of their TDL (n = 21 neurons, $R^2 = 0.30$). In c-d data are mean per subject \pm S.E.M; in e, f, g data are mean \pm standard deviation. DOI: <https://doi.org/10.7554/eLife.41714.010>

3.5 Discussion

Our findings provide a first insight into the possible cellular nature of human intelligence and explain individual variation in IQ scores based on neuronal properties: faster AP rise speed during neuronal activity and more complex, extended dendrites associate with higher intelligence. AP kinetics have profound consequences for information processing. In vivo, neurons are constantly bombarded by high frequency synaptic inputs and the capacity of neurons to keep track and phase-lock to these inputs determines how much of this synaptic information can be passed on to other neurons (Testa-Silva et al., 2014). The brain operates at a millisecond time-scale and even sub-millisecond details of spike trains contain behaviorally relevant information that can steer behavioral responses (Nemenman et al., 2008). Indeed, one of the most robust and replicable findings in behavioral psychology is the association of intelligence scores with measures of cognitive information-processing speed (Barrett et al., 1986). Specifically, reaction times (RT) in simple RT tasks provide a better prediction of IQ than other speed-of-processing tests, with a regression coefficient of 0.447 (Vernon, 1983). In addition, high positive correlations between RT and other speed-of-processing tests suggest the existence of a common mental speed factor (Vernon, 1983). Recently, these classic findings were confirmed in a large longitudinal population-based study counting more than 2000 participants (Der and Deary, 2017). Especially strong correlations between RT and general intelligence were reported for a slightly more complex 4-choice (Der and Deary, 2017). Our results provide a biological cellular explanation for such mental speed factors: in conditions of increased mental activity or more demanding cognitive task, neurons of individuals with higher IQ are able to sustain fast action potentials and can transfer more information content from synaptic input to AP output.

Pyramidal cells are integrators and accumulators of synaptic information. Larger dendrites can physically contain more synaptic contacts and integrate more information. Indeed, human pyramidal neuron dendrites receive twice as many synapses as in rodents (DeFelipe et al., 2002) and corticocortical whole-brain connectivity positively correlates with the size of dendrites in these cells (Scholtens et al., 2014; van den Heuvel et al., 2015). In this and a

previous study (Mohan et al., 2015), we find almost 2-fold larger dendritic arbor size (mean TDL = 14.67 ± 4 mm) and number of dendritic branches (64.03 ± 17.7) compared to reports that use post-mortem tissue (Bianchi et al., 2013; Elston et al., 2001; Jacobs et al., 2001). The differences could be explained by a number of advantages of biocytin filled neurons in surgical resections compared to traditionally used Golgi stainings in human post-mortem tissue. The cortical slices in our study are thicker ($350 \mu\text{m}$ compared to $120\text{--}250 \mu\text{m}$) and contain neurons with almost completely intact apical and basal dendrites, while other studies use only basal dendrites for quantification (Jacobs et al., 2001). Furthermore, only a small number of neurons are filled in a slice, which allows to unambiguously quantify all dendrites from individual cells. Importantly, the tissue comes from a living donor compared to post-mortem tissue collection, and thus does not suffer from post-mortem delays (de Ruiter, 1983) and only still living functional cells are filled. At the same time, post-mortem studies make it possible to make comparative analysis of several cortical areas. A gradient in complexity of pyramidal cells in cortical superficial layers accompanies the increasing integration capacity of cortical areas, indicating that larger dendrites are required for higher-order cortical processing (Elston et al., 2001; Jacobs et al., 2001; van den Heuvel et al., 2015). Our results align well with these findings, suggesting that the neuronal complexity gradient also exists from individual to individual and could explain differences in mental ability.

Within human cortex, association areas contain neurons with larger and more complex dendrites than primary sensory areas, while neuronal cell body density is lower in cortical association areas compared to primary sensory areas (DeFelipe et al., 2002; Elston, 2003). Larger neurons are not as tightly packed together within cortical space as smaller cells. A recent study by (Genç et al., 2018) used multi-shell diffusion tensor imaging to estimate parieto-frontal cortical dendritic density and found that higher IQ scores correlated with lower values of dendritic density (Genç et al., 2018). This may indicate that parieto-frontal cortical areas in individuals with higher IQ scores have less densely packed neurons, and may suggest that these neurons are larger. In our study, we carefully determined the amount and complexity of dendrite for each neuron, a computational unit within the cortex with well-defined input-output signals. Taking the results of (Genç et al., 2018) and our

study together may suggest that the neuronal circuitry associated with higher intelligence is organized in a sparse and efficient manner, where larger and more complex pyramidal cells occupy larger cortical volume.

Larger dendrites have an impact on excitability of cells (Bekkers and Häusser, 2007; Vetter et al., 2001) and determine the shape and rapidity of APs (Guy Eyal et al., 2014). Increasing the size of dendritic compartments in silico lead to acceleration of AP onset and increased encoding capability of neurons (Guy Eyal et al., 2014). Both in models and in slice recordings, changes of AP initiation dynamics were shown to fundamentally modify encoding of fast changing signals and the speed of communication between ensembles of cortical neurons (Guy Eyal et al., 2014; Ilin et al., 2013). Neurons with fast AP onsets can encode high frequencies and respond quickly to subtle input changes. This ability can be impaired and response speed is decreased when AP onsets are slowed down by experimental manipulations (Ilin et al., 2013). Our results not only demonstrate that AP speed depends on dendritic length and influences information transfer, but also show that both dendritic length and AP speed in human neurons correlate with intelligence. Thus, individuals with larger dendrites are better equipped to transfer synaptic information at higher frequencies.

Remarkably, dendritic morphology and different parameters of AP waveform are also parameters that we have previously identified as showing pronounced differences between humans and other species (Mohan et al., 2015; Testa-Silva et al., 2014). Human pyramidal cells in layers 2 and 3 have 3-fold larger and more complex dendrites than in macaque or mouse (Mohan et al., 2015). Moreover, human APs have lower firing threshold and faster AP onset kinetics both in single APs and during repeated firing (Testa-Silva et al., 2014). These differences across species may suggest evolutionary pressure on both dendritic structure and AP waveform and emphasize specific adaptations of human pyramidal cells in association areas for cognitive functions.

Our results were obtained from patients undergoing neurosurgical procedure and, thus, may potentially raise questions on how representative our findings are for normal healthy human subjects. Although no healthy controls can be used for single cell measurements, we addressed this issue in the following way. Firstly, in all patients, the resected neocortical tissue was not part of

epileptic focus or tumor and displayed no structural or functional abnormalities in preoperative MRI, electrophysiological recordings or microscopic investigation of stained tissue. Secondly, none of the parameters correlated with age at epilepsy onset, seizure frequency, age or disease duration (Figure 3.1— figure supplement 1). Thirdly, IQ, dendritic length or AP rise speed were not different across different patient groups (Figure 3.1— figure supplement 2). Finally, the cortical thickness correlation with general intelligence we observe in our study was also reported in hundreds of healthy subjects. Taken together, these results indicate that our findings are not likely to be influenced by disease background of the subjects.

In this study, intelligence was measured using WAIS IQ score, that combines results of 11 individual subtests of cognitive functioning into a single full-scale IQ score (Taylor and Heaton, 2001; Wechsler, 2008). This inevitably simplifies and reduces a multi-dimensional human trait to a single number. Although none of the intelligence tests can capture all aspects of human intelligence, IQ tests have proven their validity and relevance. The results of different cognitive subtests are highly correlated and generate a strong general factor – general intelligence or Spearman’s *g* (Spearman, 1904). Spearman’s *g*, calculated based on subtests of WAIS and expressed in total full-scale IQ score, strongly correlates with highly relevant life outcomes, including education, occupation, and income (Foverskov et al., 2019; Strenze, 2007). Moreover, intelligence is a stable trait over time in the same individual: the results of intelligence tests at the age of 11 predict the scores at the age of 90 (Deary et al., 2013; Gow et al., 2011). Thus, despite its shortcomings, full scale IQ score provides a relevant and meaningful estimation of general intelligence that lies at the core of cognitive differences between individuals.

In conclusion, our results provide first evidence that already at the level of individual neurons, such parameters as dendritic size and ability to maintain fast responses link to general mental ability. Multiplied by an astronomical number of cortical neurons in our brain, very small changes in these parameters may lead to large differences in encoding capabilities and information transfer in cortical networks and result in a speed advantage in mental processing and, finally, in faster reaction times and higher cognitive ability.

3.6 Materials and methods

3.6.1 Human subjects and brain tissue

All procedures were performed with the approval of the Medical Ethical Committee of the VU University Medical Centre, and in accordance with Dutch license procedures and the Declaration of Helsinki. Written informed consent was provided by all subjects for data and tissue use for scientific research. All data were anonymized.

Human cortical brain tissue was removed as a part of surgical treatment of the subject in order to get access to a disease focus in deeper brain structures (hippocampus or amygdala) and typically originated from gyrus temporalis medium (Brodmann area 21). Speech areas were avoided during resection surgery through functional mapping. We obtained neocortical tissue from 46 patients (24 females, 22 males; age range 18–66 years, Table 3.1) treated for mesial temporal sclerosis, removal of a hippocampal tumor, low grade hippocampal lesion, cavernoma or another unspecified temporal lobe pathology. From 35 of these patients, we also obtained pre-surgical MRI scans, from 31 patients we recorded Action Potentials from 129 neurons and from 25 patients we had fully reconstructed dendritic morphologies from 72 neurons.

In all patients, the resected neocortical tissue was not part of epileptic focus or tumor and displayed no structural/functional abnormalities in preoperative MRI investigation, electrophysiological whole-cell recordings or microscopic investigation of stained tissue. The physiological recordings, subsequent morphological reconstructions, morphological and action potential analysis were performed blind to the IQ of the patients.

3.6.2 IQ scores

Total IQ scores were obtained from all 46 subjects using the Dutch version of Wechsler Adult Intelligence Scale-III (WAIS-III) (Taylor and Heaton, 2001) and in some cases WAIS-IV (Wechsler, 2008) and consisted of following subtests: information, similarities, vocabulary, comprehension, block design, matrix reasoning, visual puzzles, picture comprehension, figure weights, digit span, arithmetic, symbol search and coding.

The tests were performed as a part of neuropsychological examination shortly before surgery, typically within one week.

3.6.3 MRI data and cortical thickness estimation

T1-weighted brain images (1 mm thickness) were acquired with a 3T MR system (Signa HDXt, General Electric, Milwaukee, Wisconsin) as a part of pre-surgical assessment (number of slices = 170– 180). Cortical reconstruction and volumetric segmentation was performed with the Freesurfer image analysis suite (<http://freesurfer.net>) (Fischl and Dale, 2000). The processing included motion correction and transformation to the Talairach frame. Calculation of the cortical thickness was done as the closest distance from the grey/white boundary to the grey/CSF boundary at each vertex and was based both on intensity and continuity information from the entire three-dimensional MR volume (Fischl and Dale, 2000). Neuroanatomical labels were automatically assigned to brain areas based on Destrieux cortical atlas parcellation as described in (Fischl et al., 2004). For averaging, the regions in temporal lobes were selected based on Destrieux cortical atlas parcellation in each subject.

3.6.4 Slice preparation

Upon surgical resection, the cortical tissue block was immediately transferred to ice-cold artificial cerebral spinal fluid (aCSF) containing in (mM): 110 choline chloride, 26 NaHCO₃, 10 D-glucose, 11.6 sodium ascorbate, 7 MgCl₂, 3.1 sodium pyruvate, 2.5 KCl, 1.25 NaH₂PO₄, and 0.5 CaCl₂ (300 mOsm) and transported to the neurophysiology laboratory (within 500 m from the operating room). The transition time between resection of the tissue and the start of preparing slices was less than 15 min. After removing the pia and identifying the pia-white matter axis, neocortical slices (350 μm thickness) were prepared in ice-cold slicing solution (same composition as described above). Slices were then transferred to holding chambers in which they were stored for 30 min at 34 °C and for 30 min at room temperature before recording in aCSF, which contained (in mM): 125

NaCl; 3 KCl; 1.2 NaH₂PO₄; 1 MgSO₄; 2 CaCl₂; 26 NaHCO₃; 10 D-glucose (300 mOsm), bubbled with carbogen gas (95% O₂/5% CO₂), as described previously (Mohan et al., 2015; Testa-Silva, 2010; Testa-Silva et al., 2014; Verhoog et al., 2016, 2013).

3.6.5 Electrophysiological recordings

Cortical slices were visualized using infrared differential interference contrast (IR-DIC) microscopy. After the whole cell configuration was established, membrane potential responses to steps of current injection (step size 30–50 pA) were recorded. None of the neurons showed spontaneous epileptiform spiking activity. Recordings were made using Multiclamp 700A/B amplifiers (Axon Instruments) sampling at frequencies of 10 to 50 kHz, and lowpass filtered at 10 to 30 kHz. Recordings were digitized by pClamp software (Axon) and later analyzed off-line using custom-written Matlab scripts (MathWorks). Patch pipettes (3–5 MOhms) were pulled from standard-wall borosilicate capillaries and filled with intracellular solution containing (in mM): 110 K-gluconate; 10 KCl; 10 HEPES; 10 K-phosphocreatine; 4 ATP-Mg; 0.4 GTP, pH adjusted to 7.3 with KOH; 285–290 mOsm, 0.5 mg/ml biocytin. All experiments were performed at 32–35 °C. Only cells with bridge balance of <20 MOhm were used for further analysis.

3.6.6 Morphological analysis

During electrophysiological recordings, cells were loaded with biocytin through the recording pipette. After the recordings the slices were fixed in 4% paraformaldehyde and the recorded cells were revealed with the chromogen 3,3-diaminobenzidine (DAB) tetrahydrochloride using the avidin–biotin–peroxidase method (Horikawa and Armstrong, 1988). Slices (350 µm thick) were mounted on slides and embedded in mowiol (Clariant GmbH, Frankfurt am Main, Germany). Neurons without apparent slicing artifacts and uniform biocytin signal were digitally reconstructed using NeuroLucida software (MicroBrightfield, Williston, VT, USA), using a 100

oil objective. After reconstruction, morphologies were checked for accurate reconstruction in x/y/z planes, dendritic diameter, and continuity of dendrites. Finally, reconstructions were checked using an overlay in Adobe Illustrator between the NeuroLucida reconstruction and Z-stack projection image from Surveyor Software (Chromaphor, Oberhausen, Germany). Only neurons with virtually complete dendritic structures were included; cells with major truncations due to slicing procedure were excluded.

Superficial layers pyramidal neurons were identified based on morphological and electrophysiological criteria at cortical depth within 400–1400 μm from cortical surface, that we previously found to correspond to cortical layers 2, 3 and 4 in humans (Mohan et al., 2015). For each neuron, we extracted total dendritic length (TDL) of all basal and apical dendrites and number of branch points and computed average TDL and average number of branch points for each subject by pooling data from all cells within one subject (1 to 10 neurons per subject). Only neurons without major truncations of apical dendrites by tissue sectioning were included for morphological analysis (Deitcher et al., 2017; Mohan et al., 2015).

3.6.7 NEURON modelling

Following previous work (Eyal et al., 2016; Guy Eyal et al., 2014) conductance-based multicompartmental ‘Hodgkin and Huxley models’ (Hodgkin and Huxley, 1952) of each of the reconstructed human pyramidal cells were built. To each model, a cylindrical axon (1 μm in diameter) was connected to the soma, consisting of a 50 μm long Axon Initial Segment (AIS) and a 1 mm long myelinated part. The AIS consisted of 25 electrical compartments, the rest of the axon of 21 compartments. Simulations were run with the open-source software simulator NEURON v.7.5 (Carnevale and Hines, 2006) (<https://neuron.yale.edu/neuron>), with $dt = 10 \mu\text{s}$ integration time step at 37 °C. All compartments incorporated passive membrane properties, with specific capacitance $C_m = 0.75 \text{ mF/cm}^2$, axial resistance $R_a = 0.1 \text{ MOhm/cm}$, specific resistance $R_m = 30.3 \text{ MOhm/cm}^2$, and leak-currents with reversal potential $E = 70 \text{ mV}$. In the myelinated part of the axon C_m was decreased 37.5 times and R_m was increased 5 times. Across all dendritic compartments, C_m was increased by 84% and R_m was decreased by the same

amount to account for dendritic spines (Benavides-Piccione et al., 2002; Sarid et al., 2007). Active membrane properties consisted of voltage-dependent fast-inactivating sodium (Na^+) and delayed-rectifier potassium (K^+) ionic conductances, taken from the SenseLab ModelDB database (McDougal et al., 2017) (<https://senselab.med.yale.edu/modeldb>) and set to: $g_{\text{Na}} = 0 \text{ pS}/\mu\text{m}^2$, $g_{\text{K}} = 0 \text{ pS}/\mu\text{m}^2$ in the myelinated axon, $g_{\text{Na}} = 8000 \text{ pS}/\mu\text{m}^2$ and $g_{\text{K}} = 1500 \text{ pS}/\mu\text{m}^2$ in AIS, $g_{\text{Na}} = 800 \text{ pS}/\mu\text{m}^2$, $g_{\text{K}} = 320 \text{ pS}/\mu\text{m}^2$ in the soma, and $g_{\text{Na}} = 20 \text{ pS}/\mu\text{m}^2$ and $g_{\text{K}} = 10 \text{ pS}/\mu\text{m}^2$ for dendrites. Reversal potentials for Na^+ and K^+ currents were +50 mV and 85 mV, respectively. Resulting input resistances were $61.5 \pm 4.73 \text{ MOhm}$ and resting potentials were $70.5 \pm 0.02 \text{ mV}$. Onset rapidity of simulated action potentials (APs) was calculated as the slope of membrane potentials $V(t)$ in the phase plane (i.e. $V(t)$ vs dV/dt) at 10 mV/ms and averaged across APs in simulated trains. The dynamical input-output ‘transfer gain’ (Köndgen et al., 2008; Linaro et al., 2018; Testa-Silva et al., 2014) was determined by injecting sinusoidally oscillating input currents for 120 s at the soma, with amplitude I_1 , frequency F (1–1000 cycle/s), a DC baseline I_0 amplitude, and randomly fluctuating component I_{noise} :

$$I(t) = I_0 + I_1 \sin(2\pi Ft) + I_{\text{noise}}(t) \quad (3.1)$$

$I_{\text{noise}}(t)$ was an exponentially filtered stochastic Gaussian white-noise (Arsiero et al. 2007), with zero-mean, variance s^2 and correlation length $\tau_1 = 5 \text{ ms}$, by iterating at each simulation time step:

$$I_{\text{noise}}(t + dt) = \left(1 - \frac{dt}{\tau_1}\right) I_{\text{noise}}(t) + s\sqrt{2dt/\tau_1}\xi_t \quad (3.2)$$

where $\{\xi_t\}$ is a sequence of independent pseudo-random Gaussian numbers. s^2 was set such that membrane potential hyperpolarization resulted in subthreshold potential fluctuations of $\sim 3 \text{ mV}$ at -75 mV . DC baseline I_0 was set to induce mean firing rates of $\sim 10 \text{ spike/s}$. I_1 was set to 1/6 of I_0 . AP firing times $\{t_k\}$ were detected at the soma and collected across all values of F . The output ‘transfer gain’ $r_1(F)$ at a given frequency F was defined as the amplitude of complex numbers in polar form:

$$r_1(F) = \text{amplitude} \left\{ \sum_{j=1}^N \exp(j2\pi Ft_k) \right\} / N \quad (3.3)$$

where N is the number of spikes and j is the imaginary unit. $r_1(F)$ was further normalized to $r_1(F_0)$, with $F_0 = 3$ cycle/s. The profile of $r_1(F)$ resembled a low-pass electrical filter, with cut-off frequency F_c defined as the highest frequency at which $r_1(F_c) = r_1(F_0)/\sqrt{2}$. Input waveforms in Figure 3.4, inset, consisted of three rapidly varying components for 240 s:

$$I(t) = I_0 + I_1[\sin(2\pi F_1 t) + \sin(2\pi F_2 t) + \sin(2\pi F_3 t)]/3 + I_{noise}(t) \quad (3.4)$$

with $F_1 = 200$, $F_2 = 300$, $F_3 = 450$ cycle/s.

3.6.8 Action Potential waveform analysis of electrophysiological recordings

Action Potential (AP) waveforms were extracted from voltage traces recorded in response to intracellular current injections and sorted according to their instantaneous firing frequency. Instantaneous frequency was determined as $1/\text{time to previous AP}$. Subsequently all APs were binned in 10 Hz bins, while the first APs in each trace were isolated in a separate bin. AP rise speed was defined as the peak of AP derivative (dV/dt). For each analyzed cell, representative APs with all parameters were plotted for visual check to avoid errors in the analysis.

For each neuron, the mean values of AP rise speed in a given frequency bin were obtained by averaging all APs within that frequency bin. Relative AP rise speeds were calculated by dividing the mean AP rise speed in each frequency bin (1–10 Hz, 11–20 Hz, 21–30 Hz and 31 to 40 Hz) by the mean first AP rise speed (first APs in the train of APs).

To obtain AP values for each subject, AP parameters within each frequency bin were averaged for all neurons from one subject. All AP analysis was performed using customized Matlab scripts (source code available at <https://github.com/INF-Rene/Morphys> (Verhoog et al., 2018); copy archived at <https://github.com/elifesciences-publications/Morphys>).

3.6.9 Statistical analysis

Statistical significance of all correlations between parameters was determined using Pearson correlation and linear regression (using Matlab, version R2017a, Mathworks). As multiple cells were measured per subject, correlations were calculated on mean parameter values per subject. All Pearson correlation coefficients and p values for correlations are shown in figure insets, R^2 coefficients and sample sizes are shown in figure legends and main text.

For statistical analysis of AP data, we divided all subjects according to their IQ into two groups: group with $IQ > 100$ and a group with $IQ < 100$. Differences between 2 IQ groups in AP rise times were statistically tested using Student t-test. For analysis of different patient groups (Figure 3.1—figure supplements 2) an ANOVA test was applied for each parameter separately.

3.7 Acknowledgements

We thank Dr Linda Douw for her assistance with the analysis of brain imaging data and Mr. M Wijnants for his technical assistance and to the supercomputer facilities CalUA (University of Antwerp) for computing time. NAG received funding for this work from the from the Netherlands Organization for Scientific Research (NWO; VENI grant). HDM received funding for this work from the Netherlands Organization for Scientific Research (NWO; VICI grant), ERC StG ‘BrainSignals’, and EU H2020 ‘Human Brain Project’ grant agreement no. 604102.

3.8 Ethics

Human subjects: All procedures were performed with the approval of the Medical Ethical Committee of the VU University Medical Centre (2012/362), and in accordance with Dutch license procedures and the Declaration of Helsinki. Written informed consent was provided by all

subjects for data and tissue use for scientific research. All data were anonymized.

3.9 References

- Barrett P, Eysenck HJ, Lucking S. 1986. Reaction time and intelligence: A replicated study. *Intelligence* **10**:9–40. doi:10.1016/0160-2896(86)90025-5
- Bekkers JM, Häusser M. 2007. Targeted dendrotomy reveals active and passive contributions of the dendritic tree to synaptic integration and neuronal output. *Proc Natl Acad Sci U S A* **104**:11447–11452. doi:10.1073/pnas.0701586104
- Benavides-Piccione R, Ballesteros-Yáñez I, DeFelipe J, Yuste R. 2002. Cortical area and species differences in dendritic spine morphology. *J Neurocytol* **31**:337–346. doi:10.1023/A:1024134312173
- Bianchi S, Stimpson CD, Bauernfeind AL, Schapiro SJ, Baze WB, McArthur MJ, Bronson E, Hopkins WD, Semendeferi K, Jacobs B, Hof PR, Sherwood CC. 2013. Dendritic Morphology of Pyramidal Neurons in the Chimpanzee Neocortex: Regional Specializations and Comparison to Humans. *Cereb Cortex* **23**:2429–2436. doi:10.1093/CERCOR
- Carnevale NT, Hines ML. 2006. The NEURON book, The NEURON Book. Cambridge University Press. doi:10.1017/CBO9780511541612
- Chklovskii DB, Schikorski T, Stevens CF. 2002. Wiring optimization in cortical circuits. *Neuron* **34**:341–347. doi:10.1016/S0896-6273(02)00679-7
- Choi YY, Shamosh NA, Sun HC, DeYoung CG, Min JL, Lee JM, Kim SI, Cho ZH, Kim K, Gray JR, Kun HL. 2008. Multiple bases of human intelligence revealed by cortical thickness and neural activation. *J Neurosci* **28**:10323–10329. doi:10.1523/JNEUROSCI.3259-08.2008
- Coleman JRI, Bryois J, Gaspar HA, Jansen PR, Savage JE, Skene N, Plomin R, Muñoz-Manchado AB, Linnarsson S, Crawford G, Hjerling-Leffler J, Sullivan PF, Posthuma D, Breen G. 2019. Biological annotation of genetic loci associated with intelligence in a meta-analysis of 87,740 individuals. *Mol Psychiatry* **24**:182–197. doi:10.1038/s41380-018-0040-6
- de Ruiter JP. 1983. The influence of post-mortem fixation delay on the reliability of the Golgi silver impregnation. *Brain Res* **266**:143–147. doi:10.1016/0006-8993(83)91317-3
- Deary IJ, Pattie A, Starr JM. 2013. The Stability of Intelligence From Age 11

- to Age 90 Years: The Lothian Birth Cohort of 1921. *Psychol Sci* **24**:2361–2368. doi:10.1177/0956797613486487
- Deary IJ, Penke L, Johnson W. 2010. The neuroscience of human intelligence differences. *Nat Rev Neurosci*. doi:10.1038/nrn2793
- DeFelipe J, Alonso-Nanclares L, Arellano JI. 2002. Microstructure of the neocortex: Comparative aspects. *J Neurocytol*. doi:10.1023/A:1024130211265
- Deitcher Y, Eyal G, Kanari L, Verhoog MB, Kahou GAA, Mansvelder HD, De Kock CPJ, Segev I, Christiaan CPJDK, Kock PJ De. 2017. Comprehensive Morpho-Electrotonic Analysis Shows 2 Distinct Classes of L2 and L3 Pyramidal Neurons in Human Temporal Cortex. *Cereb Cortex* **27**:5398–5414. doi:10.1093/cercor/bhx226
- Der G, Deary IJ. 2017. The relationship between intelligence and reaction time varies with age: Results from three representative narrow-age age cohorts at 30, 50 and 69 years. *Intelligence* **64**:89–97. doi:10.1016/j.intell.2017.08.001
- Elston GN. 2003. Cortex, Cognition and the Cell: New Insights into the Pyramidal Neuron and Prefrontal Function. *Cereb Cortex Novemb* **13**:1124–1138. doi:10.1093/cercor/bhg093
- Elston GN, Benavides-Piccione R, DeFelipe J. 2001. The pyramidal cell in cognition: a comparative study in human and monkey. *J Neurosci* **21**:RC163–RC163. doi:10.1523/JNEUROSCI.21-17-j0002.2001
- Eyal G., Mansvelder HD, de Kock CPJ, Segev I. 2014. Dendrites Impact the Encoding Capabilities of the Axon. *J Neurosci* **34**:8063–8071. doi:10.1523/jneurosci.5431-13.2014
- Eyal Guy, Mansvelder HD, de Kock CPJ, Segev I. 2014. Dendrites impact the encoding capabilities of the axon. *J Neurosci* **34**:8063–8071. doi:10.1523/JNEUROSCI.5431-13.2014
- Eyal G, Verhoog MB, Testa-Silva G, Deitcher Y, Lodder JC, Benavides-Piccione R, Morales J, Defelipe J, de Kock CPJ, Mansvelder HD, Segev I. 2016. Unique membrane properties and enhanced signal processing in human neocortical neurons. *Elife* **5**. doi:10.7554/eLife.16553
- Fischl B, Dale AM. 2000. Measuring the thickness of the human cerebral cortex from magnetic resonance images. *Proc Natl Acad Sci U S A* **97**:11050–11055. doi:10.1073/pnas.200033797

- Fischl B, van der Kouwe A, Destrieux C, Halgren E, Ségonne F, Salat DH, Busa E, Seidman LJ, Goldstein J, Kennedy D, Caviness V, Makris N, Rosen B, Dale AM. 2004. Automatically Parcellating the Human Cerebral Cortex. *Cortex* **14**:11–22. doi:10.1093/cercor/bhg087
- Foverskov E, Mortensen EL, Holm A, Pedersen JLM, Osler M, Lund R. 2019. Socioeconomic Position Across the Life Course and Cognitive Ability Later in Life: The Importance of Considering Early Cognitive Ability. *J Aging Health* **31**:947–966. doi:10.1177/0898264317742810
- Genç E, Fraenz C, Schlüter C, Friedrich P, Hossiep R, Voelkle MC, Ling JM, Güntürkün O, Jung RE. 2018. Diffusion markers of dendritic density and arborization in gray matter predict differences in intelligence. *Nat Commun* **9**:1–11. doi:10.1038/s41467-018-04268-8
- Gow AJ, Johnson W, Pattie A, Brett CE, Roberts B, Starr JM, Deary IJ. 2011. Stability and Change in Intelligence From Age 11 to Ages 70, 79, and 87: The Lothian Birth Cohorts of 1921 and 1936. *Psychol Aging* **26**:232–240. doi:10.1037/a0021072
- Hodgkin AL, Huxley AF. 1952. A quantitative description of membrane current and its application to conduction and excitation in nerve. *J Physiol* **117**:500–544. doi:10.1113/jphysiol.1952.sp004764
- Horikawa K, Armstrong WE. 1988. A versatile means of intracellular labeling: injection of biocytin and its detection with avidin conjugates. *J Neurosci Methods* **25**:1–11. doi:10.1016/0165-0270(88)90114-8
- Ikari K, Hayashi M. 1981. Aging in the Neuropil of Cerebral Cortex—A Quantitative Ultrastructural Study. *Psychiatry Clin Neurosci* **35**:477–486. doi:10.1111/j.1440-1819.1981.tb00245.x
- Ilin V, Malyshev A, Wolf F, Volgushev M. 2013. Fast computations in cortical ensembles require rapid initiation of action potentials. *J Neurosci* **33**:2281–2292. doi:10.1523/JNEUROSCI.0771-12.2013
- Jacobs B, Schall M, Prather M, Kapler E, Driscoll L, Baca S, Jacobs J, Ford K, Wainwright M, Trembl M. 2001. Yair Deitcher, Guy Eyal, Lida Kanari, Matthijs B Verhoog, Guy Antoine Atenekeng Kahou, Huibert D Mansvelder, Christiaan P J de Kock, Idan Segev. *Cerebral Cortex* **11**:558–571.
- Karama S, Ad-Dab'bagh Y, Haier RJ, Deary IJ, Lyttelton OC, Lepage C, Evans AC. 2009. Positive association between cognitive ability and cortical thickness in a representative US sample of healthy 6 to 18 year-olds. *Intelligence* **37**:145–155. doi:10.1016/j.intell.2008.09.006

- Köndgen H, Geisler C, Fusi S, Wang XJ, Lüscher HR, Giugliano M. 2008. The dynamical response properties of neocortical neurons to temporally modulated noisy inputs in vitro. *Cereb Cortex* **18**:2086–2097. doi:10.1093/cercor/bhm235
- Lam M, Trampush JW, Yu J, Knowles E, Davies G, Liewald DC, Starr JM, Djurovic S, Melle I, Sundet K, Christoforou A, Reinvang I, DeRosse P, Lundervold AJ, Steen VM, Espeseth T, Räikkönen K, Widen E, Palotie A, Eriksson JG, Giegling I, Konte B, Roussos P, Giakoumaki S, Burdick KE, Payton A, Ollier W, Chiba-Falek O, Attix DK, Need AC, Cirulli ET, Voineskos AN, Stefanis NC, Avramopoulos D, Hatzimanolis A, Arking DE, Smyrnis N, Bilder RM, Freimer NA, Cannon TD, London E, Poldrack RA, Sabb FW, Congdon E, Conley ED, Scult MA, Dickinson D, Straub RE, Donohoe G, Morris D, Corvin A, Gill M, Hariri AR, Weinberger DR, Pendleton N, Bitsios P, Rujescu D, Lahti J, Le Hellard S, Keller MC, Andreassen OA, Deary IJ, Glahn DC, Malhotra AK, Lencz T. 2017. Large-Scale Cognitive GWAS Meta-Analysis Reveals Tissue-Specific Neural Expression and Potential Nootropic Drug Targets. *Cell Rep* **21**:2597–2613. doi:10.1016/j.celrep.2017.11.028
- Linaro D, Biró I, Giugliano M. 2018. Dynamical response properties of neocortical neurons to conductance-driven time-varying inputs. *Eur J Neurosci* **47**:17–32. doi:10.1111/ejn.13761
- McDaniel MA. 2005. Big-brained people are smarter: A meta-analysis of the relationship between in vivo brain volume and intelligence. *Intelligence* **33**:337–346. doi:10.1016/j.intell.2004.11.005
- McDougal RA, Morse TM, Carnevale T, Marengo L, Wang R, Migliore M, Miller PL, Shepherd GM, Hines ML. 2017. Twenty years of ModelDB and beyond: building essential modeling tools for the future of neuroscience. *J Comput Neurosci*. doi:10.1007/s10827-016-0623-7
- Mohan H, Verhoog MB, Doreswamy KK, Eyal G, Aardse R, Lodder BN, Goriounova NA, Asamoah B, Clementine Brakspear AB, Groot C, van der Sluis S, Testa-Silva G, Obermayer J, SRM Boudewijns Z, Narayanan RT, Baayen JC, Segev I, Mansvelder HD, de Kock CP. 2015. Dendritic and Axonal Architecture of Individual Pyramidal Neurons across Layers of Adult Human Neocortex. *Cereb Cortex* **25**:4839–4853. doi:10.1093/cercor/bhv188
- Narr KL, Woods RP, Thompson PM, Szeszko P, Robinson D, Dimtcheva T, Gurbani M, Toga AW, Bilder RM, Semel T. 2007. Relationships

- between IQ and Regional Cortical Gray Matter Thickness in Healthy Adults. *Cereb Cortex* **17**:2163–2171. doi:10.1093/cercor/bhl125
- Nemenman I, Lewen GD, Bialek W, de Ruyter van Steveninck RR. 2008. Neural Coding of Natural Stimuli: Information at Sub-Millisecond Resolution. *PLoS Comput Biol* **4**:e1000025. doi:10.1371/journal.pcbi.1000025
- Pol HEH, Schnack HG, Posthuma D, Mandl RCW, Baaré WF, Van Oel C, Van Haren NE, Collins DL, Evans AC, Amunts K, Bürgel U, Zilles K, De Geus E, Boomsma DI, Kahn RS. 2006. Genetic contributions to human brain morphology and intelligence. *J Neurosci* **26**:10235–10242. doi:10.1523/JNEUROSCI.1312-06.2006
- Posthuma D, De Geus EJC, Baaré WFC, Hulshoff Pol HE, Kahn RS, Boomsma DI. 2002. The association between brain volume and intelligence is of genetic origin. *Nat Neurosci*. doi:10.1038/nn0202-83
- Salinas E, Sejnowski TJ. 2001. Correlated neuronal activity and the flow of neural information. *Nat Rev Neurosci*. doi:10.1038/35086012
- Sarid L, Bruno R, Sakmann B, Segev I, Feldmeyer D. 2007. Modeling a layer 4-to-layer 2/3 module of a single column in rat neocortex: Interweaving in vitro and in vivo experimental observations. *Proc Natl Acad Sci U S A* **104**:16353–16358. doi:10.1073/pnas.0707853104
- Scholten LH, Schmidt R, de Reus MA, van den Heuvel MP. 2014. Linking macroscale graph analytical organization to microscale neuroarchitectonics in the macaque connectome. *J Neurosci* **34**:12192–12205. doi:10.1523/JNEUROSCI.0752-14.2014
- Sniekers S, Stringer S, Watanabe K, Jansen PR, Coleman JRI, Krapohl E, Taskesen E, Hammerschlag AR, Okbay A, Zabaneh D, Amin N, Breen G, Cesarini D, Chabris CF, Iacono WG, Ikram MA, Johannesson M, Koellinger P, Lee JJ, Magnusson PKE, McGue M, Miller MB, Ollier WER, Payton A, Pendleton N, Plomin R, Rietveld CA, Tiemeier H, Van Duijn CM, Posthuma D. 2017. Genome-wide association meta-analysis of 78,308 individuals identifies new loci and genes influencing human intelligence. *Nat Genet* **49**:1107–1112. doi:10.1038/ng.3869
- Spearman C. 1904. “General Intelligence,” Objectively Determined and Measured. *Am J Psychol* **15**:201. doi:10.2307/1412107
- Strenze T. 2007. Intelligence and socioeconomic success: A meta-analytic review of longitudinal research. *Intelligence*. doi:10.1016/j.intell.2006.09.004

- Taylor MJ, Heaton RK. 2001. Sensitivity and specificity of WAIS–III/WMS–III demographically corrected factor scores in neuropsychological assessment. *J Int Neuropsychol Soc* **7**:867–874. doi:10.1017/s1355617701777107
- Testa-Silva G. 2010. Human synapses show a wide temporal window for spike-timing-dependent plasticity. *Front Synaptic Neurosci* **2**:12. doi:10.3389/fnsyn.2010.00012
- Testa-Silva G, Verhoog MB, Linaro D, de Kock CPJ, Baayen JC, Meredith RM, De Zeeuw CI, Giugliano M, Mansvelder HD. 2014. High Bandwidth Synaptic Communication and Frequency Tracking in Human Neocortex. *PLoS Biol* **12**:e1002007. doi:10.1371/journal.pbio.1002007
- Trampush JW, Yang MLZ, Yu J, Knowles E, Davies G, Liewald DC, Starr JM, Djurovic S, Melle I, Sundet K, Christoforou A, Reinvang I, Derosse P, Lundervold AJ, Steen VM, Espeseth T, Rääkkönen K, Widen E, Palotie A, Eriksson JG, Giegling I, Konte B, Roussos P, Giakoumaki S, Burdick KE, Payton A, Ollier W, Horan M, Chiba-Falek O, Attix DK, Need AC, Cirulli ET, Voineskos AN, Stefanis NC, Avramopoulos D, Hatzimanolis A, Arking DE, Smyrnis N, Bilder RM, Freimer NA, Cannon TD, London E, Poldrack RA, Sabb FW, Congdon E, Conley ED, Scult MA, Dickinson D, Straub RE, Donohoe G, Morris D, Corvin A, Gill M, Hariri AR, Weinberger DR, Pendleton N, Bitsios P, Rujescu D, Lahti J, Le Hellard S, Keller MC, Andreassen OA, Deary IJ, Glahn DC, Malhotra AK, Lencz T. 2017. GWAS meta-analysis reveals novel loci and genetic correlates for general cognitive function: A report from the COGENT consortium. *Mol Psychiatry* **22**:336–345. doi:10.1038/mp.2016.244
- van den Heuvel MP, Scholtens LH, Barrett LF, Hilgetag CC, de Reus MA. 2015. Bridging cytoarchitectonics and connectomics in human cerebral cortex. *J Neurosci* **35**:13943–13948. doi:10.1523/JNEUROSCI.2630-15.2015
- Verhoog M, Wilbers R, Heyer D. 2018. Morphys. <https://github.com/INF-Rene/Morphys>
- Verhoog MB, Goriounova NA, Obermayer J, Stroeder J, Johannes Hjorth JJ, Testa-Silva G, Baayen JC, de Kock CPJ, Meredith RM, Mansvelder HD. 2013. Mechanisms underlying the rules for associative plasticity at adult human neocortical synapses. *J Neurosci* **33**:17197–17208. doi:10.1523/JNEUROSCI.3158-13.2013

- Verhoog MB, Obermayer J, Kortleven CA, Wilbers R, Wester J, Baayen JC, De Kock CPJ, Meredith RM, Mansvelder HD. 2016. Layer-specific cholinergic control of human and mouse cortical synaptic plasticity. *Nat Commun* **7**:1–13. doi:10.1038/ncomms12826
- Vernon PA. 1983. Speed of information processing and general intelligence. *Intelligence* **7**:53–70. doi:10.1016/0160-2896(83)90006-5
- Vetter P, Roth A, Häusser M. 2001. Propagation of action potentials in dendrites depends on dendritic morphology. *J Neurophysiol* **85**:926–937. doi:10.1152/jn.2001.85.2.926
- Wechsler D. 2008. Wechsler Adult Intelligence Scale, Fourth. ed.

CHAPTER 4

The location of the axon initial segment
affects the bandwidth of spike initiation
dynamics

PLoS Computational Biology, 2020

4.1 Chapter information

4.1.1 Publication

Christophe Verbist, Michael G. Müller, Huibert D. Mansvelder, Robert Legenstein, Michele Giugliano

4.1.2 Author contribution

Conceived and designed the research: C.V., M.G. and R.L. Performed simulations: C.V. and M.M. Analysed the data: C.V. and M.M. Wrote the paper: C.V., M.M., R.L. and M.G. Acquired funding: R.L. and M.G.

4.2 Abstract

The dynamics and the sharp onset of action potential (AP) generation have recently been the subject of intense experimental and theoretical investigations. According to the resistive coupling theory, an electrotonic interplay between the site of AP initiation in the axon and the somato-dendritic load determines the AP waveform. This phenomenon not only alters the shape of AP recorded at the soma but also determines the dynamics of excitability across a variety of time scales. Supporting this statement, here we generalize a previous numerical study and extend it to the quantification of the input-output gain of the neuronal dynamical response. We consider three classes of multicompartmental mathematical models, ranging from ball-and-stick simplified descriptions of neuronal excitability to 3D-reconstructed biophysical models of excitatory neurons of rodent and human cortical tissue. For each model, we demonstrate that increasing the distance between the axonal site of AP initiation and the soma markedly increases the bandwidth of neuronal response properties. We finally consider the Liquid State Machine paradigm, exploring the impact of altering the site of AP initiation at the level of a neuronal population, and demonstrate that an optimal distance exists to boost the computational performance of the network in a simple classification task.

4.3 Author summary

The neurons in the brain encode information through electrical impulses. The performance of a cell in terms of its ability to process and transfer information downstream thus depends heavily on the machinery of initiation of these impulses. In this work, we consider both the cell morphology and the biophysical properties of impulse initiation as the primary parameters that influence information processing in single neurons as well as in networks. We specifically analyze the location of nerve impulse initiation along the cell's axon and the way the neuron transfers incoming information. By using single-cell models of various complexity as well as network models, we conclude that information processing is sensitive to the geometrical details of impulse initiation.

4.4 Introduction

The dynamics of AP initiation and its underlying time-scales have been themes of intense investigation in rodent and human cortical neurons, both experimentally (Boucsein et al., 2009; Ilin et al., 2013; Köndgen et al., 2008; Linaro et al., 2018; Lundstrom et al., n.d.; Naundorf et al., 2006; Tchumatchenko et al., 2011; Testa-Silva et al., 2014) and theoretically (Brette, 2013; G. Eyal et al., 2014; Fourcaud and Brunel, 2002; Ilin et al., 2013; Telenczuk et al., 2017). Investigations have focused particularly on the shape of the somatic AP, its rapidity at onset, and on its underlying biophysics (Brette, 2013; Ilin et al., 2013; Naundorf et al., 2006; Yu et al., 2008). In fact, early numerical and theoretical studies on single-compartmental models of spike-initiation (Fourcaud-Trocmé et al., 2003; Fourcaud and Brunel, 2002) suggested a strong causal relationship between the rapidity of the AP at its onset and the dynamics of the instantaneous firing rate. The latter ultimately determine the encoding and tracking properties of neurons and networks of rapid components in their input (Linaro et al., 2018). Indeed, neurons with rapid APs are able to track very fast temporal modulations of their inputs (Tchumatchenko et al., 2011; Testa-Silva et al., 2014) better than neurons with smooth AP waveforms.

The proposed biophysical bases, underlying rapid APs, have been then linked to ion channel cooperativity (Naundorf et al., 2006; Öz et al., 2015), axo-somatic backpropagation (Yu et al., 2008), and to the electrotonic coupling of dendro-somatic compartments to the site of AP initiation in the axon (Brette, 2013; G. Eyal et al., 2014). Recently, Brette and collaborators have further explored how the specific location of the AP initiation in the axon (i.e. the axon initial segment, AIS) would affect the AP rapidity at its onset (Telenczuk et al., 2017) and reviewed the diversity of AIS and axon location (Kole and Brette, 2018). Specifically, they demonstrated *in silico* that increasing the AIS distance from the soma makes the AP somatic waveform sharper than for proximal AIS locations (Telenczuk et al., 2017).

Therefore, we expect that altering the AIS location during development or upon its activity-dependent plasticity (Grubb and Burrone, 2010; Kuba, 2010) should also influence the bandwidth of the neuron input-output firing response properties, thus ultimately changing its computational performance.

In this work, we have numerically characterized how a non-stationary input is capable of destabilizing instantaneously the (otherwise stationary) output firing frequency of a model neuron, active on average at 5 spike/s. Mimicking previous experimental protocols (Boucsein et al., 2009; Köndgen et al., 2008; Linaro et al., 2018; Lundstrom et al., n.d.; Testa-Silva et al., 2014), we applied a weak oscillation on the top of a current-clamp stimulus and observed how the instantaneous firing rate of the model oscillates around 5 spike/s (e.g. 5 ± 3 spike/s). As in the experiments, faster input oscillations (e.g. 10 – 50 – 100 – 500 – 1000 cycle/s) lead to faster oscillation of the instantaneous firing rate, although with stronger amplitude attenuation. The study of this attenuation, as a function of the oscillation frequency, quantifies the linear transfer gain of the model neuron and constitutes a minimal description of the dynamics of its AP initiation. We then systematically examined the linear transfer gain in three classes of conductance-based multicompartmental model neurons. For each model, we altered the somatic distance of the AIS by controlling the density of voltage-gated sodium and potassium ion channels along the axon and estimated the (low-pass) cut-off harmonic frequency (COF) of the resulting linear transfer gain. We specifically included in our study a large class of 3D-reconstructed models of cortical neurons, using the detailed biophysical models database recently released by the Blue Brain Project (Markram et al., 2015). Furthermore, we investigated the influence of the AP onset dynamics and response bandwidth on the computational power of a neuronal network. To this end, we used the Liquid State Machine (LSM) paradigm, a standard model for generic computations in cortical microcircuits (Maass et al., 2002).

4.5 Results

We studied the dynamics of the excitability in multicompartmental neuron models with increasing complexity. We aimed at directly reproducing *in silico* an experimental protocol previously applied *in vitro*, thus enabling comparison with existing electrophysiological data. Instead of characterizing the conventional (stationary) spiking response to DC current pulses, we measured the instantaneous firing rate while injecting weak sinusoidal stimuli with a variety of harmonic frequencies f as well as fluctuating noisy waveforms into the soma of each model neuron (Figure 4.1A). We referred

the timing of each AP to the phase of the input sine (Figure. 4.1B) and applied circular statistics (see the Methods) to quantify, for each harmonic frequency f , the magnitude and the phase of the instantaneous firing rate (Figure 4.1C). These quantities describe the transfer gain associated to the dynamic response of each model (Figure 4.1A), as in the previous experiments (Köndgen et al., 2008). This allowed us to quantify how a temporal modulation of the input current influenced the instantaneous output firing rate of neurons, firing on average at 5 spike/s (see the Methods).

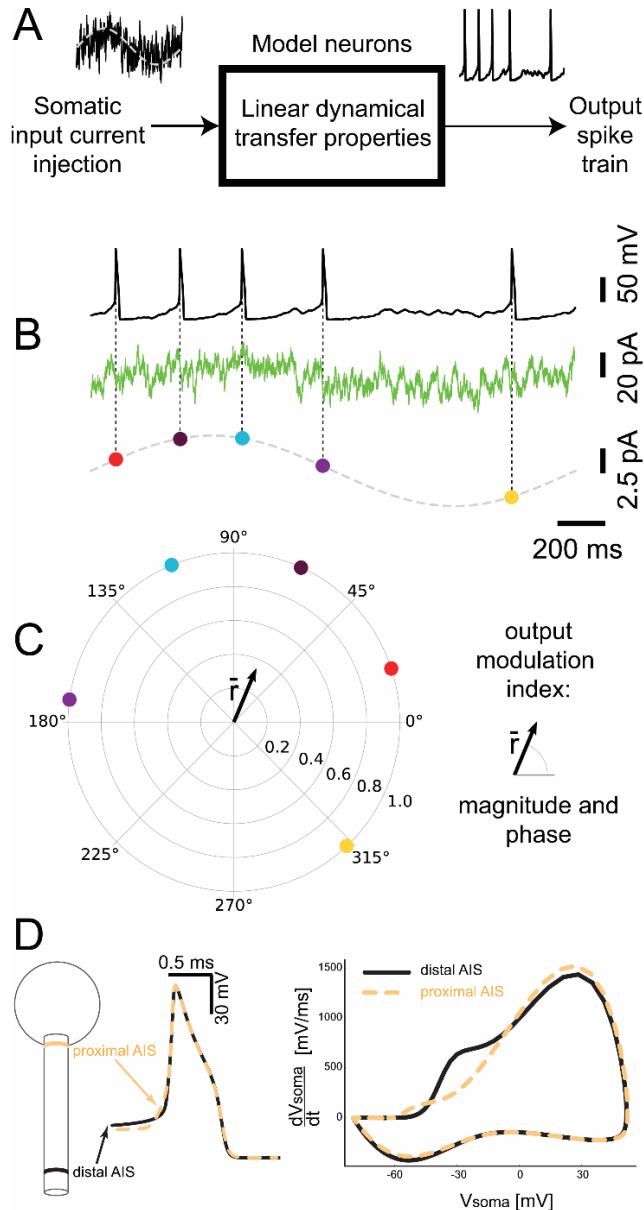


Figure 4.1. Linear dynamical transfer properties of multicompartmental model neurons. We studied the dynamics of AP initiation in neuronal models, by estimating the temporal modulation of the instantaneous firing probability, in response to the somatic injection of a noisy current (B, green trace). The offset of this current (A-B, dashed grey trace) was weakly modulated over time at a harmonic frequency f . By Circular Statistics methods, we referred the time of each AP to the corresponding phase of the input oscillation. Then we regarded in the complex plane each AP as a vector with unitary length (C, filled colored markers) (C). We finally estimated the magnitude and phase of the vectors sum \vec{r} (C), averaging together tens of thousands of APs and thus resulting in a vector with length lower than 1. We systematically explored magnitude and phase for a broad range of values of f (i.e. 10 - 1000 cycle/s). As the soma-AIS distance increased, the somatic AP waveform varied and became steeper (D).

4.5.1 The AIS location alters neuronal responsiveness

For each model neuron under consideration, we systematically varied the location of the AIS with respect to the soma and quantified the dynamics of neuronal responses, extending the scope of a recent study (Telenczuk et al., 2017). We started with a minimal model, composed of a soma and a multicompartmental axon (“ball and stick”, BAS). While relocating the AIS hardly altered the model’s input resistance (i.e. by $\sim 0.01\%$; not shown), we found that it greatly affected the steepness of somatic action potentials at their onset (Figure 4.2A-B), confirming the previous study. Specifically, we found a 7-fold increase in the slope of the action potential trajectory at onset (Figure 4.2D), corresponding to an increasing distance between the AIS and the soma of up to $50\ \mu\text{m}$. We also observed a $\sim 4\ \text{mV}$ hyperpolarization of the membrane potential at onset (Figure 4.2C), conventionally identifying the AP “threshold” potential, for the same range of AIS distances from the soma. Indicating an increase in cell excitability, a similar hyperpolarization has been already predicted by the critical resistive coupling theory (Brette, 2013) in terms of a smaller sodium-channel current eliciting an AP and resulting from the weakening of the intensity of the axo-somatic resistive current (Telenczuk et al., 2017).

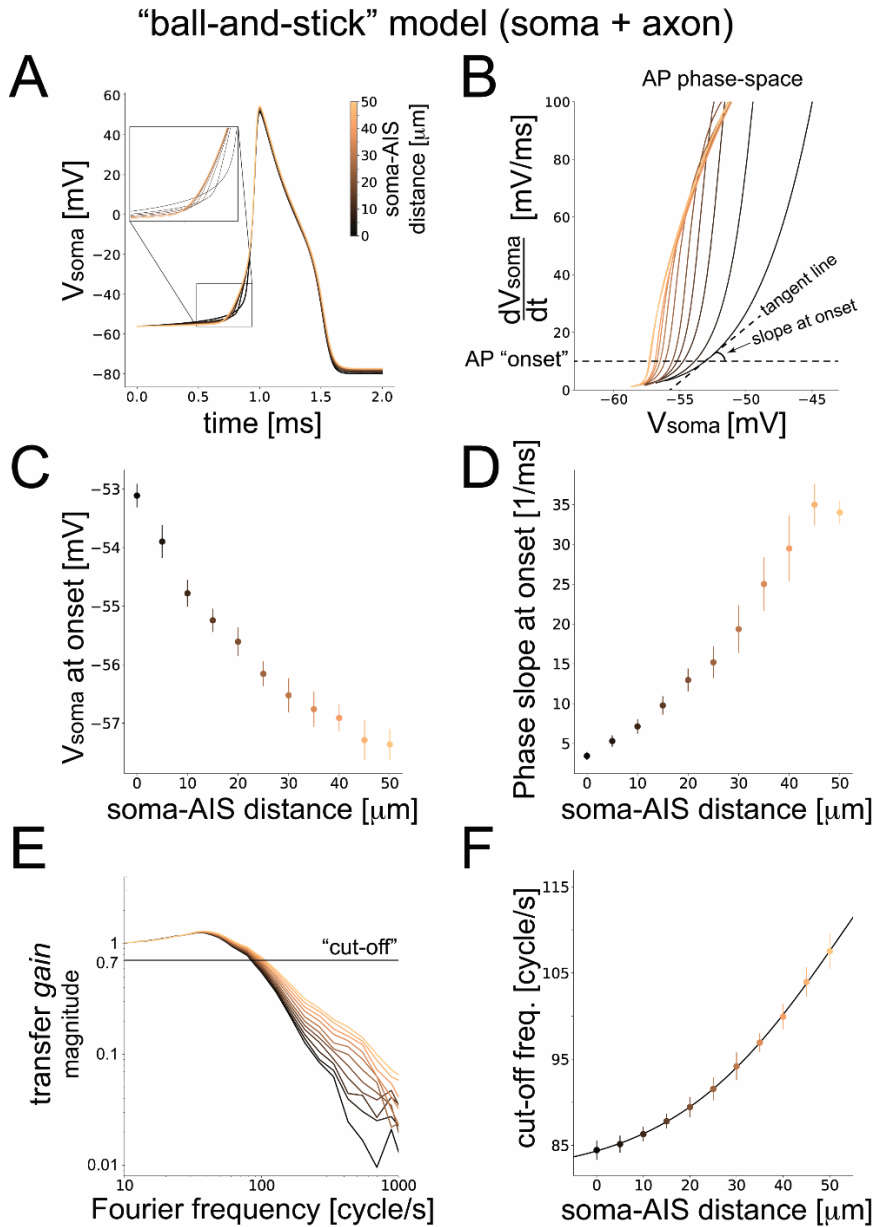


Figure 4.2. Performance of the “ball-and-stick” neuron model. Color-coding across panels reflects the soma-AIS distances, with darker colors used for more proximal AIS locations and brighter colors for more distal AIS locations. The somatic AP waveform was examined in time (A) and in the phase-space, plotting the derivative of the potential *versus* the potential (B). We conventionally set the AP “onset” to 10mV/ms (dashed horizontal black line), deriving the value of AP threshold (i.e. the potential at the onset) (C) and the AP rapidity (i.e. the phase slope at onset) (D). The magnitude of the dynamical transfer gain of the model was estimated as in Figure 4.1 and plotted in the Fourier domain, across increasing soma-AIS distances, normalized to its value at 1 cycle/s (E). The “cut-off” frequency, defined as the harmonic frequency corresponding to a 30% attenuation of the magnitude, was then studied against the soma-AIS distance (D) and fitted by a logistic function. Error bars (C-F) represent the standard deviation over 100 independent repeated simulations.

Similar to real neurons, as we probed the response of the BAS model to temporally modulated noisy waveforms (Figure 4.1), we observed a low-pass filter behavior in the Fourier domain and, characterized for large input harmonic frequency f by a $1/f^\alpha$ power law. The value of its exponent α decreased from 1.82 to 1.03 almost linearly with an increasing AIS distance from the soma (Figure 4.2E). The low pass filter gain profile was normalized with its value at $f = 1$ cycle/s and then quantified in terms of a conventional cutoff frequency (COF). Such a COF describes the value of f where the transfer gain attenuates down to 70% of its normalized amplitude (Figure 4.2E). In our numerical study, we observed a $\sim 30\%$ increase in the COF, ranging from ~ 85 cycle/s to ~ 110 cycle/s (Figure 4.2F) as the AIS moved away from the soma up to $50 \mu\text{m}$. Note how the increase in the COF is accompanied by a change in the slope of the curves, exclusively for large Fourier frequencies (Figure 4.2E).

4.5.2 Multicompartmental neuron models

We repeated the same analysis for a family of 3D reconstructed multicompartmental models of rat neocortical neurons, released by the Blue Brain Project (BBP). Restricting our focus to excitatory cells only, we first report the results observed for a L5 thick-tufted pyramidal cell (TTPC). We augmented these models with a functional multicompartmental axon, identical in geometry and biophysical properties to the one used in the BAS model. Note that, in the original multicompartmental description of the cell's morphology by the BBP, the axon was also simplified to a short "stick" version.

The somatic AP slope at its onset increased with the AIS - soma distance, although markedly less (~ 2 -fold) than in the BAS model (Figure 4.3A-D). The progressive hyperpolarization of the membrane potential at onset was similar in all cases (~ 3 mV difference; Figure 4.3C) and similarly corresponding to an excitability increase predicted by the critical resistive theory (Brette, 2013; Telenczuk et al., 2017).

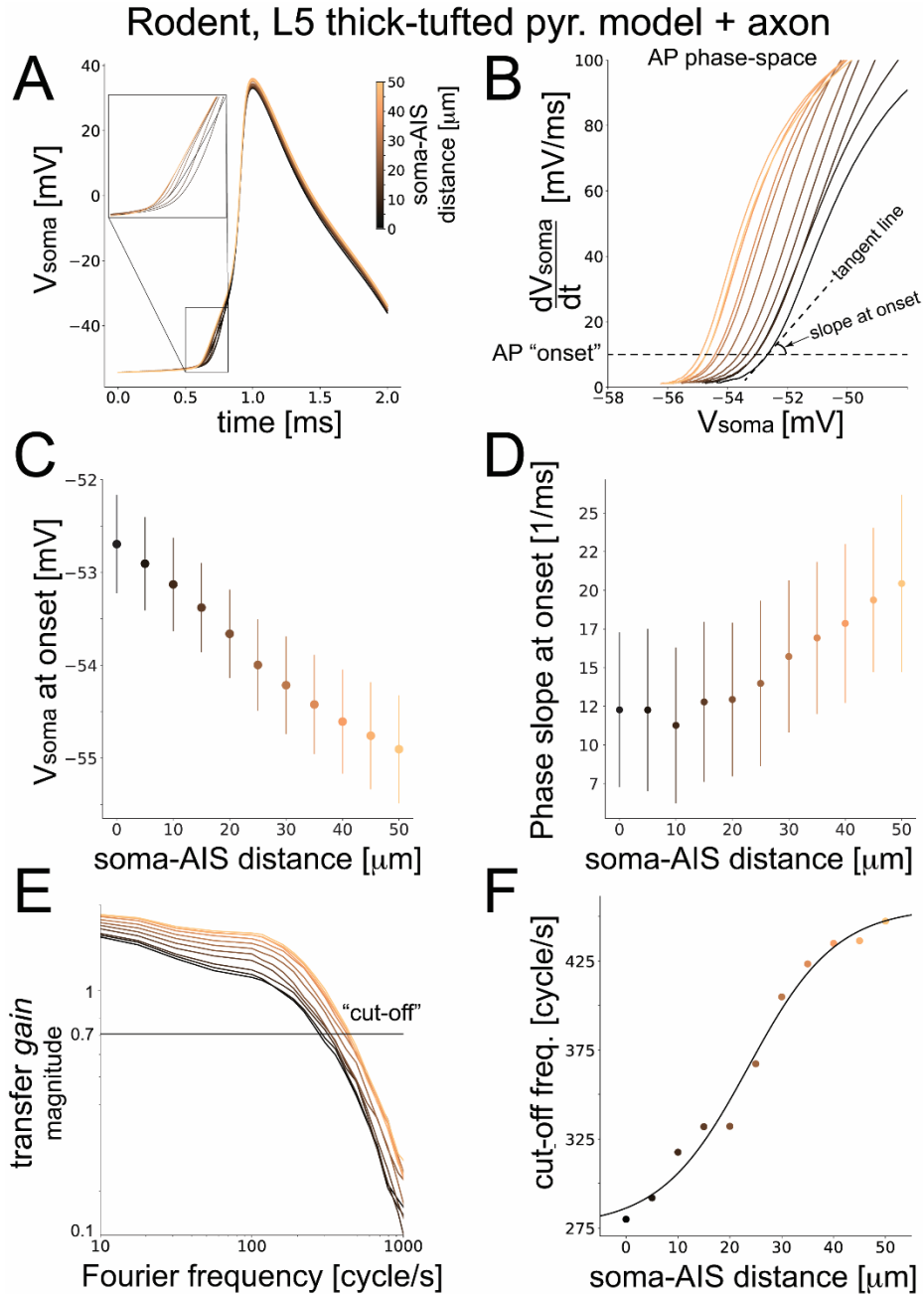


Figure 4.3. Performance of a rat cortical pyramidal neuron model. We repeated the analysis of Figure 4.2 for a model of rat neocortical layer 5 pyramidal cells. As in the “ball-and-stick” model, when the AIS moved away from the soma (A), the somatic AP became steeper (A), while its threshold potential decreased (B,C) and its rapidity at onset increased (B,D). The magnitude of the dynamical transfer gain of the model was plotted in the Fourier domain, across increasing soma-AIS distances, normalized to its value at 1 cycle/s (E). The “cut-off” frequency was then studied against the soma-AIS distance (D) and fitted by a logistic function. Color coding as in Figure 4.2 and error bars (C-F) representing the standard deviation over 100 independent repeated simulations.

When examined in the Fourier domain, the magnitude of the transfer gain was quantitatively very similar to experimental reports (Ilin et al., 2013; Köndgen et al., 2008; Linaro et al., 2018) with a COF well above $f = 100$ cycle/s. Interestingly, its low-pass profile featured roughly the same slope at large harmonic frequencies f , regardless of the AIS location (Figure 4.3E). Notably, increasing the AIS - soma distance caused a 55% increase in the value of the COF, ranging from ~ 275 cycle/s to ~ 450 cycle/s and effectively altering the overall bandwidth of the neuronal response (Testa-Silva et al., 2014).

Encouraged by the agreement with the previous experimental data and intrigued by the significant modulation of neuronal bandwidth by the AIS location, we further studied the same phenomenon in all other 65 model cells of the BBP database, representative of 13 distinct types of excitatory neurons (i.e. $65 = 13 * 5$ instances of each type) (Markram et al., 2015). As for the TTPC, we augmented each of the 65 models with a multicompartmental axon, identical to the cases discussed so far. We confirmed, not only, similar effects of the AIS location on the transfer bandwidth in all other excitatory cells, but we could also rank response width and sensitivity of each model.

According to our simulations (Figure 4.4), the neuronal cells with the broadest bandwidth of their transfer gain are those located in layer 4, followed in ranking by those in layer 6, layer 5, and finally in layer 2/3. Figure 4.4 summarizes how the COF varies with the increasing soma – AIS distance, accompanying data points (colored markers) by sigmoidal best fit functions (black continuous traces). However, when studying the sensitivity to the AIS location of the bandwidth, the previous ranking reversed with layer 2/3 cells exceeding all the other layers (Figure 4.4; see Table 4.1 and the curve slope k parameter). Regardless of the cell type, layer 4 cells displayed the weakest sensitivity to the AIS location of their bandwidth, with a change of $\sim 10 - 12\%$. Similarly, L6 cells had a modest increase in their COFs, quantified as $\sim 14 - 17\%$, for increasing values of the AIS - soma distance. L5 had a stronger dependency, with an increase up to 60%. We thus observed an extremely high sensitivity to AIS location for L2/3 pyramidal cells, with up to $\sim 150\%$ increase of the COF (in the range 200 – 400 cycles/s). In addition, over all 65 models tested, the slope of the transfer *gain* for high harmonic frequencies f did not vary substantially (not shown) upon

moving away the AIS from the soma, as observed for the TTPC (Figure 4.3E).

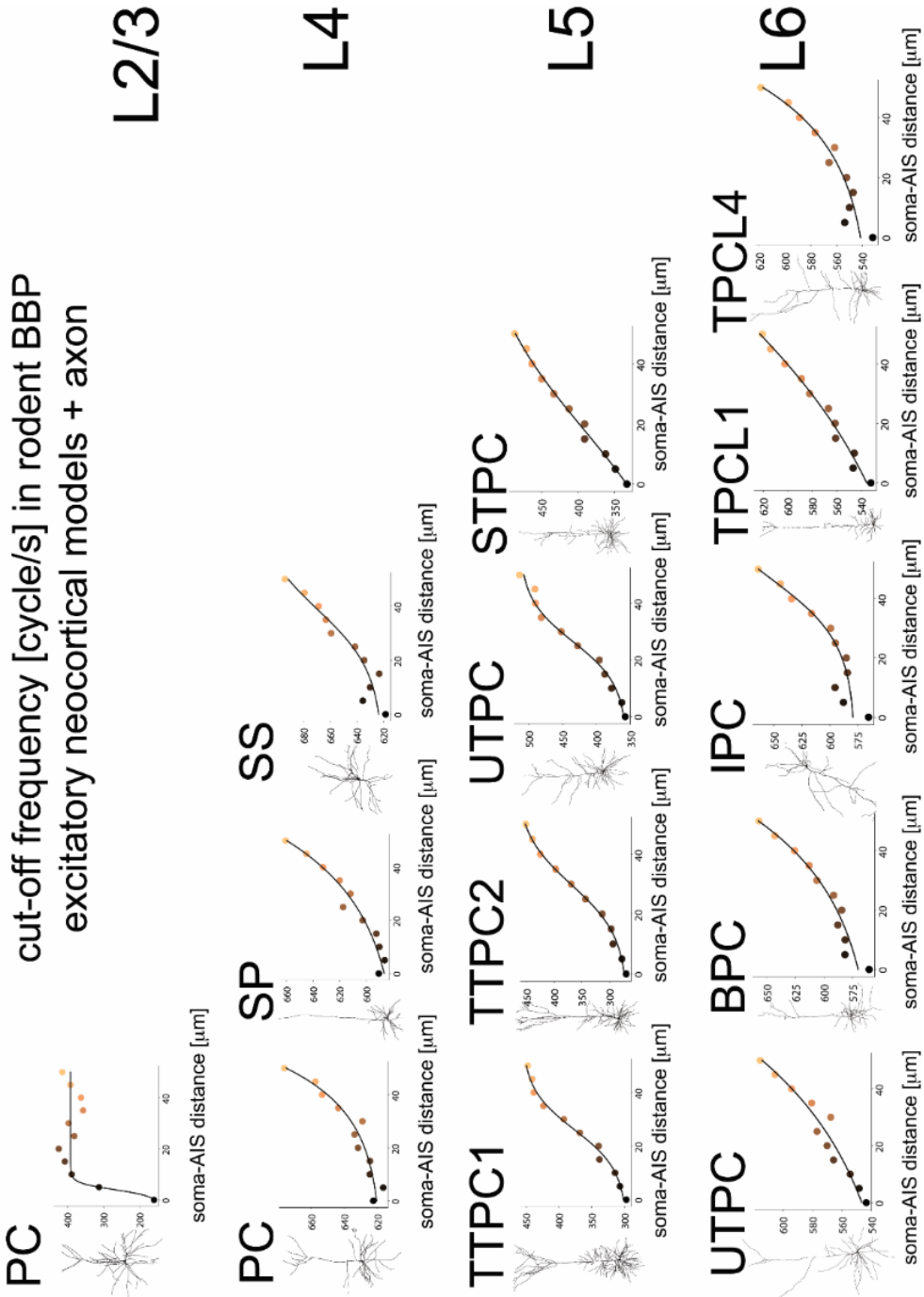


Figure 4.4. Performance of various excitatory rat cortical neuron models. We repeated the analysis of Figs. 4.2-4.3, focusing on the “cut-off” frequency sensitivity to the soma-AIS distance (see Figure 4.2F, 4.3F) of all the 13 excitatory neuron models, as released by the Blue Brain Project. Each panel refers to a distinct cell type across cortical layers 2/3, 4, 5, and 6, and is representative of Pyramidal Cells (PC), Star Pyramidal cells (SP), Spiny Stellate neurons (SS), Thick-Tufted Pyramidal Cells (TTPC), Untufted Pyramidal Cells (UTPC), Slender Tufted Pyramidal Cells (STPC), Pyramidal Cell with Bipolar apical-like dendrites (BPC), Pyramidal Cell with Inverted apical-like dendrites (IPC), Tufted Pyramidal Cell with apical dendrites terminating in Layer 1 (TPCL1), and Tufted Pyramidal Cell with apical dendrites terminating in Layer 4 (TPCL4). The continuous traces represent logistic functions whose parameters (Table 4.1) have been best fitted to the simulation results. Color coding as in Figure 4.2.

Summarizing the sensitivity of the COF on the AIS - soma distance, we provide below the best-fit parameters of a logistic function (see the Methods), indicating the layer and the cell type:

	a	k	d ₀	b
L23 - PC	242.86	0.747	4.02	148.73
L4 - PC	3339.00	0.056	121.02	616.93
L4 - SP	2261.71	0.038	134.15	573.59
L4 - SS	98.24	0.086	38.65	620.23
L5 - TTPC1	309.86	0.043	18.14	237.51
L5 - TTPC2	160.00	0.129	26.12	296.38
L5 - UTPC	203.68	0.114	29.74	266.72
L5 - STPC	158.90	0.130	26.45	355.61
L6 - UTPC	2875.42	0.035	141.00	552.11
L6 - BPC	153.73	0.091	47.16	577.21
L6 - IPC	471.09	0.023	85.16	478.35
L6 - TPCL1	2762.32	0.045	125.18	532.61
L6 - TPCL4	3235.00	0.023	196.43	515.90

Table 4.1. Best-fit parameters. For each different excitatory model of the BBP database, the best fit parameters of a logistic function (Eq. 4.4) of Figure 4.4 are represented in this table.

As a further validation experiment, we also inspected the phase of the transfer gain for one of the models (L6 TTPC-L4), as we increased the AIS - soma distance (Figure A in S1 Supporting Information). As expected from experimental data (Köndgen et al., 2008; Linaro et al., 2018), we found that

the relationship between the phase and the AIS distance could be fitted, for large harmonic frequencies f , by a straight line (Fourcaud-Trocmé et al., 2003). By definition, a linear dependency on f in the Fourier domain corresponds to the presence of a time delay in the time domain. We could therefore verify that the farther the AIS is from the soma, the longer is the propagation delay of the AP generated at the AIS and recorded at the soma.

Finally, as larger dendritic trees have been shown to contribute to the dynamical transfer properties of neurons (G. Eyal et al., 2014), we studied the dynamical response of a model reconstructed from the human neocortical tissue (HUM, Figure 4.5). This model was available from a previous study (Goriounova et al., 2018) and featured a morphology considerably larger than any rat cortical cell. In the HUM model, we observed only a modest sensitivity (~ 2 fold) to the AIS position of the AP slope at the onset, while the increase in excitability by a hyperpolarization of the somatic AP threshold voltage was comparable to the other models. When examining the transfer gain, only a $\sim 20\%$ increase in the COF was observed (Figure 4.5F). Note also how the increase in the cutoff is not accompanied with any change in the slope of the curves for large Fourier harmonic frequencies f (Figure 4.5E), as opposed to Figure 4.2E.

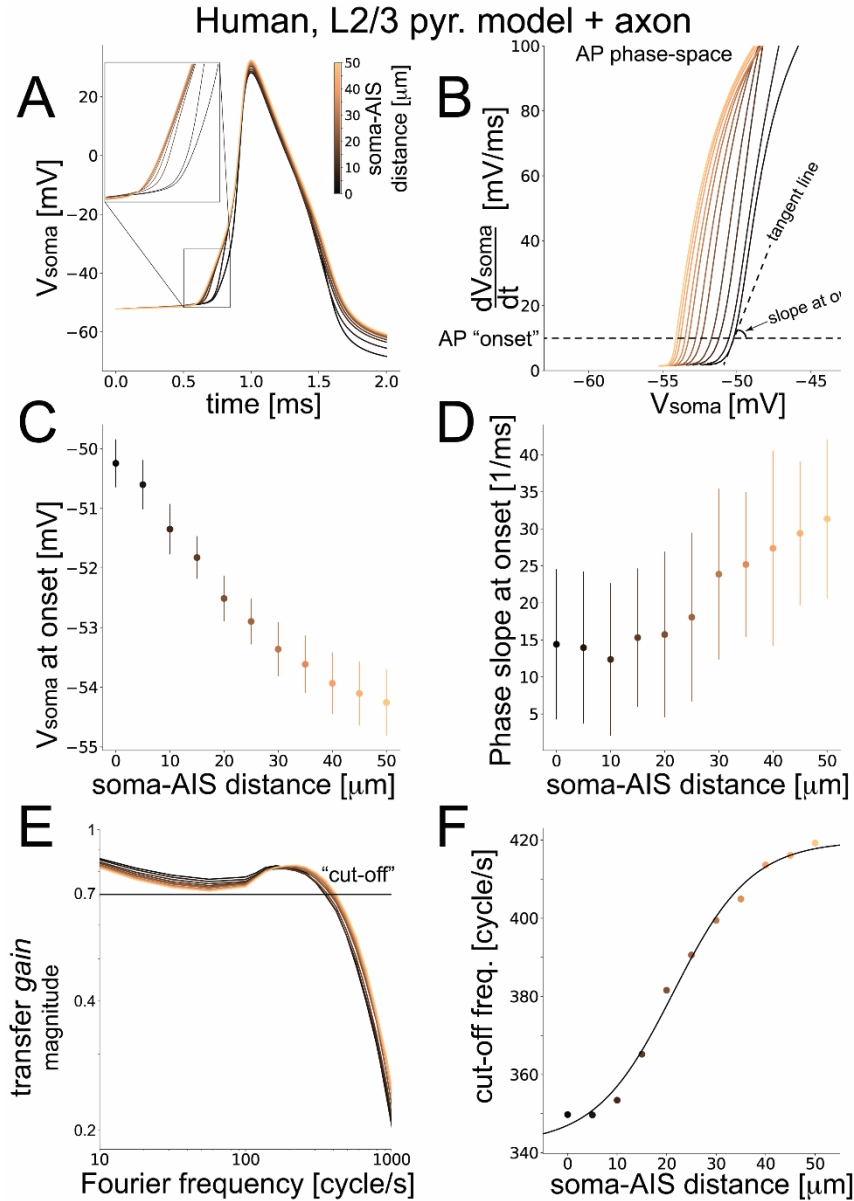


Figure 4.5. Performance of a human cortical neuron model. We repeated the analysis of Figs. 4.2-4.3 for a multicompartmental model of human neocortical layer 2/3 pyramidal cells. When the AIS moved away from the soma (A), the somatic AP became steeper (A), while its threshold potential decreased (B,C) and its rapidity at onset increased (B,D). The magnitude of the dynamical transfer gain of the model was plotted in the Fourier domain, across increasing soma-AIS distances, normalized to its value at 1 cycle/s (E). The “cut-off” frequency was then studied against the soma-AIS distance (D) and fitted by a logistic function. Color coding as in Figure 4.2 and error bars (C-F) representing the standard deviation over 100 independent repeated simulations.

Concluding this section, Table 4.2 summarizes for the BAS, the L5 TTPC pyramidal BBP, and the HUM models, the sensitivity of the COF on the AIS - soma distance d as the best-fit parameters of a logistic function (see the Methods).

	a	k	d_0	b
BAS	57.69	0.0541	53.32	81.3
TTPC BBP	180.9	0.1167	23.47	247.1
HUM	77.56	0.1271	21.35	342.2

Table 4.2. Best fit parameters across models. The best-fit parameters for the logistic functions in Figs. 4.2-4.3F and 4.5F are represented in this table.

4.5.3 Network simulations

Since the bandwidth of AP initiation dynamics ultimately determines the signal transfer properties of large networks (Fourcaud-Trocmé et al., 2003), we hypothesized that changing the AIS location might to some extent influence the computational properties of a neuronal network. We therefore investigated the influence of the AIS location on the performance of a Liquid State Machine (LSM) model (Maass et al., 2002). As all multicompartmental models examined here were computationally expensive, we reduced the BAS model into an equivalent single-compartmental exponential integrate-and-fire (eIF) (Fourcaud-Trocmé et al., 2003) (Figure 4.6), closely following established methods (Badel et al., 2008a, 2008b). In a LSM, a cortical microcircuit is modelled as a randomly connected network of excitatory and inhibitory integrate-and-fire neurons (the “liquid”, see Figure 4.7A) with dynamic synaptic transmission (Tsodyks et al., 1998). Projection neurons in cortical layers III and V are modelled in the LSM as linear readout neurons, which receive as input filtered spike trains from a random subset of neurons in the liquid. We used the output of the readout neurons as output of the LSM. When inputs are presented to the network via a number of input neurons, the recurrent connections give rise to prolonged reverberating activity in the liquid, whose rich dynamics are used by the linear readout (trained as a supervised classifier) to achieve some desired output behavior. It has been shown that this simple model possesses remarkable

computational capabilities as it can approximate any fading memory filter (Maass et al., 2002).

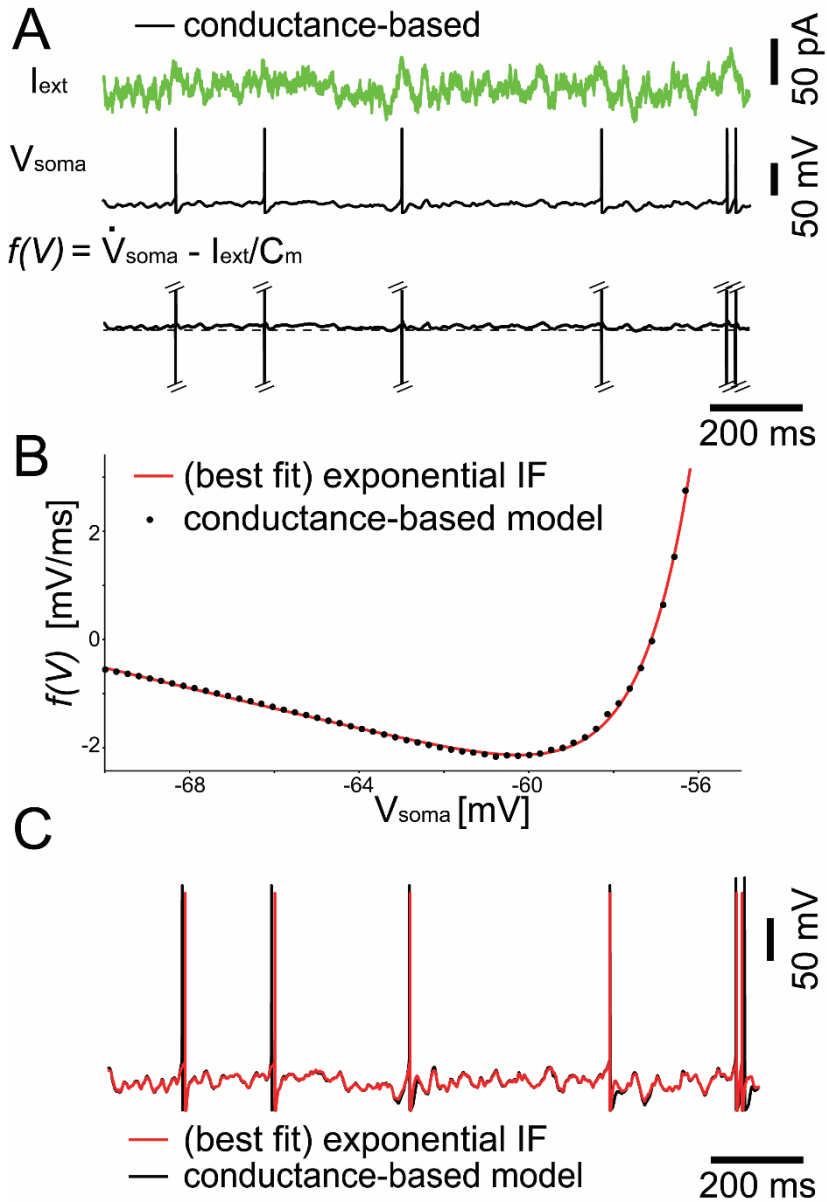


Figure 4.6. Reduction to a point neuron model. We tuned the parameters of an exponential Integrate-and-Fire (eIF) point neuron model to optimally match the membrane potential of the ball-and-stick model, in response to the same noisy input current. (A) The voltage-dependent AP initiation current was isolated by subtraction, (B) best fitted to the current-voltage relationship of the eIF, and (C) shown to adequately capture both the timing of individual APs and the trajectory of subthreshold membrane potential.

To determine the computational capabilities of these LSMs, we considered a delayed XOR task (Figure 4.7B-C). This simple task tests two important properties of the network: its short-term memory (Hasson et al., 2015) and its nonlinear processing capabilities, both potentially linked to the AP initiation dynamics. We generated two prototypical input AP patterns lasting 50 ms and using 10 input channels (Figure 4.7B) and presented a random sequence of jittered versions of these patterns (spike shifts drawn from a Gaussian with zero mean and 5 ms standard deviation). We trained a binary classifier as readout to compute the XOR of the input at the end of each pattern presentation.

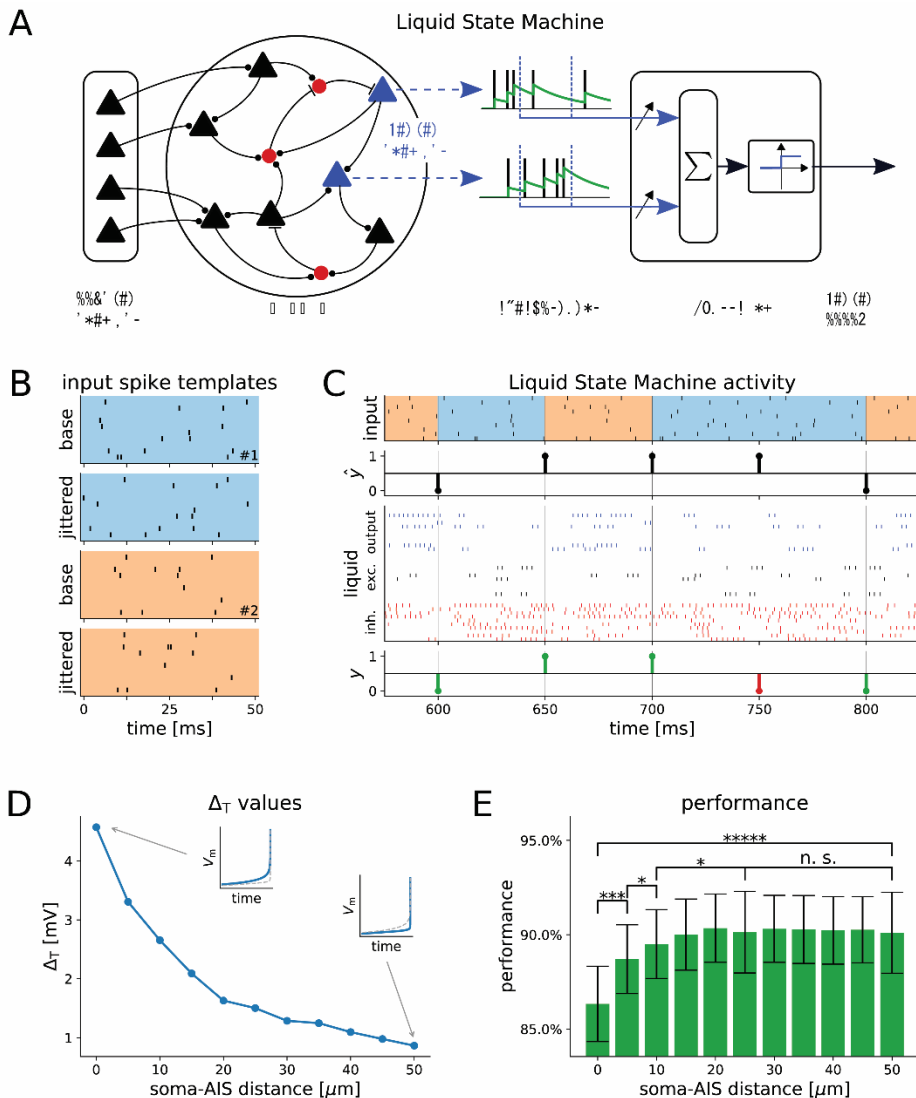


Figure 4.7. Liquid-state machine computations. In order to test the functional impact of the AIS location and of the bandwidth of the transfer gain, we simulated a network of exponential Integrate-and-Fire (eIF) units using parameters fit to models with different AIS locations (see Figure 4.6 and Table 4.3). (A) The input was fed to a pool of recurrently connected neurons (black and blue: excitatory, red: inhibitory). Neurons were connected randomly through dynamic synapses. The filtered spikes (liquid states) of a subset of excitatory neurons (output neurons, blue), was used as input to a linear classifier. (B) The network input consisted of jittered versions of two base spike templates. (C) The classifier was trained to compute a XOR of the last two shown templates (top) using the spikes of the output neurons (blue) in the liquid (middle). As performance criterion we recorded how often the readout response y (bottom) matched the target output \hat{y} (correct outputs are shown in green, incorrect outputs in red) for the parameters for different AIS locations (e.g. the AP slope Δ_T). (D) The fitted Δ_T values are shown versus the soma-AIS distance. The insets show the change of the slope at the AP onset from the first to the last AIS position. (E) As we varied the AIS locations, the Liquid State Machine performance improved in the classification task. The effect was significant for the first two distance increments (50 runs, Wilcoxon rank-sum test, $*=p < 0.05$, $**=p < 0.005$, etc.).

We used this setup to study the influence of the AIS location on the performance of the LSM (Figure 4.7D) by varying the intrinsic parameters used for the neurons within the *liquid*. The systematic reduction of the multicompartmental models into a point neuron (Badel et al., 2008b) resulted in one set of eIF parameters for each AIS – soma distance (see the Methods), allowing us to determine the computational effect of changing the AIS location.

We found that the location of the AIS had a significant impact on the LSM performance (Figure 4.7E), as the mean classification accuracy increased from 86% when the AIS was located at 0 μm to over 90% when the AIS was pushed far away from the soma. The increase in LSM performance stopped after a distance of 20 μm was reached, revealing a saturating regime. The differences in the mean network accuracy were small but highly significant (see Figure 4.7E). The parameter sets for different AIS locations differ primarily in the value of Δ_T , which sets the AP sharpness in the eIF model, but also in other values (see Table 4.3). One might therefore ask whether Δ_T , by defining the signal transfer behavior of individual neurons (Fourcaud-Trocmé et al., 2003), exerts the main influence on the network performance. We repeated the same simulations using the eIF parameters at one of the medium distances, and varied only Δ_T in the set {0.5, 2.5, 4.5} mV (roughly the value range for this parameter found by the fitting procedure). The results show a significant correlation between the AP sharpness and the LSM performance (Figure C in S1 Supporting Information), which suggests that the observed effect of the AIS location on network performance is mainly driven by the changes of the AP slope at spike onset. We furthermore performed additional experiments with different sets of network parameters (see Methods and Figure C in S1 Supporting Information Figure 4.2). The results (Supporting Figure 4.2) show that the relationship between soma-AIS distance and network performance holds in a number of different scenarios.

AIS-soma d (μm)	τ_m (ms)	E_L (mV)	V_T (mV)	Δ_T (mV)
0	3.40	-74.14	-62.34	4.57
5	5.05	-74.04	-61.28	3.31
10	5.93	-74.09	-60.61	2.66
15	6.89	-74.27	-59.90	2.09
20	7.85	-74.51	-59.14	1.63
25	7.60	-74.39	-59.16	1.50
30	7.86	-74.46	-58.95	1.29
35	7.58	-74.36	-59.14	1.25
40	7.70	-74.39	-59.01	1.10
45	7.74	-74.40	-58.96	0.98
50	7.76	-74.40	-58.89	0.87

Table 4.3. eIF parameter for BAS model. Numerical parameters, resulting from fitting eIF models to the BAS model with a different AIS-soma distance d , are reported in the table.

4.6 Discussion

This work is grounded in two recent theories: 1) how AP initiation determines the dynamic response of a neuron to time-varying inputs (Fourcaud-Trocmé et al., 2003; Fourcaud and Brunel, 2002), and 2) how compartmentalization explains the sharpness of somatic AP initiation (Brette, 2013; Telenczuk et al., 2017).

The first predicts that the transfer gain, linking in the Fourier domain the instantaneous output firing rate of a neuron to its input, depends on two biophysical properties: the AP sharpness and the average firing rate. Intuitively, we may grasp the former by considering an analogy with the operation of “convolution” (or, equivalently, filtering) of a signal. In fact, when a signal is convolved with a “slow/smooth” function, the result appears blurred, smoothed, and lacking the high-frequency content of the original signal, as in a low-pass electronic filter. On the other hand, when the convolution occurs with a “sharper” function (i.e. as sharp and steep as an impulse), the result resembles more faithfully the original signal. Thus, the sharper the “convolution kernel” the broader the transfer bandwidth, so that sharper somatic AP waveforms correspond to broader bandwidth of the input-output responses of a neuron.

The second theory predicts that an electrotonic interaction between the soma and the axon is responsible for the AP initiation. In this case, the inward sodium currents at the axonal site of AP initiation is matched by the axial resistive current, flowing from the axon to the soma and forming a dipole. This alters the sharpness of the somatic AP, as an intrinsic signature of the global current-loop between the soma and the AIS and not a consequence of studying AP waveforms in a distinct site from where it was generated. In particular, Brette and colleagues (Telenczuk et al., 2017) showed an increase in the sharpness of the AP when moving the AIS away from the soma.

Combining the predictions of the two theories together, we found that as the AIS relocation modifies the AP sharpness, the bandwidth of the transfer gain of the neuron is also altered. We have examined this phenomenon in a variety of multicompartmental mathematical models and found that as the location of the AIS is moved away from the soma, the sharpness of the AP

increases and the bandwidth increases, allowing an even more reliable transfer of high-frequency information from the input to the output of the neurons.

It is interesting to set our result in the broader context of an activity-dependent form of AIS homeostatic plasticity, recently described *in vitro* for excitatory neurons (Grubb and Burrone, 2010). It was elegantly shown that a prolonged increase in the neuronal firing rate triggers a distal displacement of the AIS of up to 17 μm from the soma, while a decrease in firing reversed the effect. We speculate that this plasticity could be functionally linked, and possibly even synergistic, to our results. In fact, as a neuron increases its mean firing rate (e.g. from 5 to 10 spike/s), its bandwidth and COF increase accordingly (Fourcaud-Trocmé et al., 2003; Fourcaud and Brunel, 2002). Then, upon the homeostatic displacement of the AIS location, the COF would even further increase, broadening the overall bandwidth of the input-output dynamical transfer properties of the neurons. Perhaps a similar interaction might support the cooperation between functional and structural plasticities, jointly contributing to make the neuron a broader information channel, capable of routing downstream information with increased temporal accuracy.

To the best of our knowledge, our results also provide, for the first time, proof of a very good quantitative match between detailed (i.e. BBP and HUM) cortical neuron models and experimental findings regarding their dynamical transfer function (Ilin et al., 2013; Köndgen et al., 2008; Linaro et al., 2018; Tchumatchenko et al., 2011; Testa-Silva et al., 2014). Moreover, the simulations described in Figure 4.4 for all 13 types of excitatory neurons allow us to make a prediction on the cells' dynamical transfer properties across several layers. It will be very interesting to test in experiments whether the performance ranking across cell types is confirmed. These are important elements to make conclusions about the validity and good predictive value of the BBP model database, when tested in experimental protocols not included in the original model optimization procedures (Markram et al., 2015).

Compared to the dynamics observed in the BAS model, the AP trajectory of BBP models always showed a biphasic behavior at its onset, even when the AIS was closest to the soma. This is a consequence of the electrotonic role

played by the dendritic tree, which is absent in the BAS model. Indeed, according to the critical resistive coupling theory (Brette, 2013; Telenczuk et al., 2017), the BBP models' dendritic arborizations act as a large current sink for the axon, where the AP is generated. Along these lines, HUM and BBP models differed only quantitatively, given the substantially larger dendritic tree in HUM reconstructed morphology, as already discussed (G. Eyal et al., 2014).

Despite the simplicity of the (short) axonal geometry used here, our conclusions remain true even for longer and more accurate axonal geometries. In fact, augmenting the original axon model with 1 mm long unmyelinated or myelinated geometry extensions affected our results only quantitatively but not qualitatively (Figure B in S1 Supporting Information).

Searching for functional significance of the AIS-soma distance sensitivity (described above for different model neurons), we asked whether a broader or narrower neuronal bandwidth leads to an advantage for information processing in networks of neurons (Fourcaud-Trocmé et al., 2003). We investigated this question using the LSM paradigm, a generic model for computations in cortical microcircuits (Buonomano and Maass, 2009; Maass et al., 2002). As simulations of large networks of neurons are infeasible using the detailed morphological models described above, we reduced these models to exponential integrate-and-fire units. This reduction resulted in one set of neuron parameters per AIS-soma distance, which allowed us to investigate the impact of the AIS location on the computational capabilities of the network. These single-compartmental neuron models of course fail at capturing in its entirety the broad complexity of electrophysiological phenomena of multicompartmental models. Nonetheless, their description of neuronal excitability can mimic AP initiation in an effective manner, allowing us to explore network dynamical properties with modest CPU resources.

We used this network to solve a delayed XOR task, which incorporates two essential components of information processing in neural circuits: short-term memory and nonlinear processing capabilities. Generally, the network was able to solve this task quite well, but the results differed for different AIS locations. We found small but highly significant increases in accuracy as we increased the AIS-soma distance. It is intriguing to note that in L5 cortical

cells the AIS starts within 5-10 μm from the soma (Hamada et al., 2016), while the average length of the AIS is 25-40 μm , (Baranauskas et al., 2013) shows that APs are initiated at the distal end of the AIS, which would correspond to a AIS distance of roughly 25-50 μm in our simulations.

To conclude, we have confirmed that the bandwidth of the spike initiation mechanisms is highly sensitive to the location of the AIS along the axon, in simplified models as well as in a family of biophysically accurate cortical model neurons. We have also shown the impact of the AIS location on computation in a network of neurons. In contrast to the highly complex task solved by cortical networks *in vivo*, we have considered a rather simple task and have used networks of modest size. It is possible that the significant changes of network performance we observe in our setup will be amplified when larger networks with hierarchical structure and model complex tasks are considered.

4.7 Materials and Methods

4.7.1 Conductance-based model neurons

We simulated three types of conductance-based multicompartmental models, running the NEURON simulator (Carnevale and Hines, 2006; Hines and Carnevale, 2001) on a high-performance computer cluster. The first type, referred to as the “ball-and-stick” (BAS) model in the text, had a single-compartmental soma and no dendrites. The second type, referred to as “Blue Brain Project” (BBP) models in the text, featured somata, realistic dendritic trees, and accurate excitable membrane properties, reconstructed from rat somatosensory cortical neurons over 13 distinct electrical classes (Markram et al., 2015). BBP models consisted of 65 distinct models, extracted from a subset (i.e. only excitatory cells) of a previously released database (<https://bbp.epfl.ch/nmc-portal/downloads>). Finally, the third type, referred to as the “human pyramidal neuron” (HUM) in the text, was based on a 3D-reconstructed pyramidal cell from the superficial layers of human temporal cortical tissue, as described previously (Goriounova et al., 2018). HUM was equipped with very basic excitable membrane properties (Goriounova et al., 2018), following closely the approach of (G. Eyal et al., 2014).

Each BAS, BBP, and HUM model was extended to include an identical multicompartmental axon, originating from the soma, with the same geometry and membrane electrical mechanisms. This axon was described as a cylinder, with diameter of 1 μm and length of 50 μm and was computer simulated as a set of 11 individual compartments, whose axial resistance and specific capacitance were 150 Ωcm and 0.5625 μFcm^2 , respectively. Each compartment included passive and active ionic currents with parameters chosen as in (Yu et al., 2008), namely fast-inactivating sodium- and delayed-rectifier potassium-currents, as well as voltage-independent mixed “leakage” currents. Briefly, the Nernst’s reversal potentials of these currents were set uniformly to 60 mV, -80 mV, and -60 mV, for sodium, potassium, and leak currents, respectively. The values of the corresponding maximal ionic conductances varied in space from one compartment to the next. Specifically, while the maximal conductance of the leak currents was fixed along the axon to $3.3 \cdot 10^{-5}$ pS/ μm^2 , the values for sodium- and potassium-currents differed and were markedly higher (i.e., ~ 100 times) corresponding

to one *ad hoc* compartment, chosen to represent the AIS. These values were 88 nS/ μm^2 and 17.6 nS/ μm^2 at the AIS *versus* 0.8 nS/ μm^2 and 0.16 nS/ μm^2 everywhere else along the axon, for sodium- and potassium-currents, respectively. In additional simulations (Figure B, in S1 Supporting Information) we increased the length of the axon, adding other 840 compartments, to model an unmyelinated 1 mm long extension. Alternatively, we implemented an myelinated 1 mm long extension of the axon by 42 additional compartments as in (Guy Eyal et al., 2014).

For the three classes of models considered in this work the spatial proximity of the AIS to the soma could be varied at will by defining the maximal ionic conductances of each axonal compartment to reflect the AIS location. All model details and computer code are publicly available from FigShare (DOI: 10.6084/m9.figshare.12123279).

4.7.2 Linear Dynamical Transfer Properties: Spike-Train Analysis in the Fourier Domain

In analogy to an experimental protocol adopted *in vitro* for real neurons to probe the dynamics of their neuronal excitability (Boucsein et al., 2009; Ilin et al., 2013; Köndgen et al., 2008; Linaro et al., 2018; Testa-Silva et al., 2014) and also used in previous *in silico* investigations (G. Eyal et al., 2014; Fourcaud-Trocmé et al., 2003; Ilin et al., 2013), the BAS, BBP, and HUM models were injected at their somata with a fluctuating stimulation current. This current was composed as the superposition of a DC offset, a sine wave with harmonic frequency f , and a Gaussian colored noise:

$$I(t) = I_0 + I_1 \sin(2\pi F t) + s I_n(t) \quad (4.1)$$

where $I_n(t)$ was the noise term, generated using an iterative expression (Gillespie, 1996) and representing a realization of an Ornstein-Uhlenbeck stochastic process (Destexhe et al., 2003) with zero mean, unitary standard deviation, and autocorrelation time-length τ . The values of the harmonic frequency f were chosen from the range of 1 cycle/s to 10'000 cycle/s in each simulation, which lasted 100 s and was repeated 10-100 times. The numerical integration time step of the model equations was set to 0.005 ms, ensuring numerical stability and avoiding any aliasing of the injected sinusoidal waveform.

For each AIS location, we set $I_1 = 0$ and adapted the values of I_0 (i.e. the stimulus' mean) and s (i.e. the stimulus' standard deviation) to achieve the same steady-state output mean firing rate r_0 of 5 spike/s and the same standard deviation of the subthreshold fluctuations of their membrane potential, in the range 5 – 10 mV. We note that to this aim, the rescaling of I_0 and s was very minor, corresponding to changes of less than 2% and 0.001%, respectively. Under such a stationary firing regime, for small amplitudes I_1 (i.e. $I_1 \ll I_0$) of the input sine wave, the BAS, BBP, and HUM models neurons generated spike trains, whose instantaneous firing rate $r(t)$ linearly reflected the input oscillation and could be described at the (periodic) steady-state as

$$r(t) = r_0 + r_1 \sin(2\pi f t + \Phi) \quad (4.2)$$

where r_1 and Φ were found to vary as functions of f . These quantities represent the magnitude and the phase of the linear dynamical transfer response of the neuron, expressed as a complex number (Fourcaud-Trocmé et al., 2003; Köndgen et al., 2008). They were directly estimated from the times of occurrence of somatic spikes t_k (i.e. $k = 1, 2, \dots, N$) by circular statistics (Ilin et al., 2013), in terms of the magnitude and of the angle of a complex quantity:

$$\mathbf{r} = \frac{1}{N} \sum_{k=1}^N e^{j 2\pi f t_k} \quad (4.3)$$

where $j = \sqrt{-1}$ is the imaginary unit. Throughout the figures of this paper, we refer to the response modulation index (i.e. r_1/r_0) of the model neuron as the *transfer gain*, estimated as twice the magnitude $\|\mathbf{r}\|$. We normalized this quantity by its value at $f = 1$ cycle/s, so that neuronal transfer gains could be systematically compared across neuron models and conditions.

For a subset of our BBP models simulations, we also examined the phase Φ that we estimated as the angle of \mathbf{r} , studying how it changed with f . As reported elsewhere for real neurons and in conductance-based models (Fourcaud-Trocmé et al., 2003; Köndgen et al., 2008; Linaro et al., 2018), $\Phi(f)$ is best described by an additional decreasing linear trend for large values of f . Accordingly, the slope of the best-fit straight line to the profile of $\Phi(f)$ for large values of f allowed us to quantify the corresponding propagation delay δt in the time domain.

4.7.3 Action Potential Trajectory and Transfer Gain profile

AP waveforms were recorded from the somatic compartments in all simulated neuron models, in response to noisy stimulation alone (i.e. setting $I_1 = 0$) and under the same steady-state firing regime as already described. The AP trajectory was then examined both in the time domain *versus* $V_{\text{soma}}(t)$ and in the *phase space* dV_{soma}/dt *versus* V_{soma} , averaging successive APs over a period of 40 s (i.e. about 200 APs, at 5 spike/s). The analysis in the *phase space* was restricted for the range of values corresponding to the AP initiation (i.e. -70 to 50 mV) (Naundorf et al., 2006). The AP *onset* was conventionally defined as the moment in time during the upstroke AP trajectory when the rate of membrane potential increase exceeded 10 mV/ms (Naundorf et al., 2006). The AP *phase slope at onset* was then defined as the rapidity of the AP trajectory in the phase space at the onset (i.e. the slope of the tangent line to the AP curve at 10 mV/ms).

With regards to the normalized transfer gain, its (low-pass) *cut-off* Fourier harmonic frequency was measured operatively by employing the common definition used in electronic filter analysis as well as in previous works (Fourcaud-Trocmé et al., 2003). Corresponding to the “half power” frequency of a filter, the *cut-off* is value of the harmonic frequency f corresponding to a 30% attenuation of the gain (i.e. a value of ~ -3 dB). When studied systematically for an increasing soma-AIS distance d , the dependence of the COF on d was also summarized by optimally fitting the four parameters of the logistic function:

$$COF(d) = \frac{a}{1+e^{-k(d-d_0)}} + b \quad (4.4)$$

where a is the function’s maximal value, k represents its steepness at the midpoint d_0 , and b is an offset.

4.7.4 Reduction to the Integrate-and-Fire point neuron model

All multicompartmental models examined in this work were computationally expensive, making the numerical simulation of large networks unfeasible. In the perspective of including an analysis based on the

Liquid State Machine paradigm (see below), we reduced our multicompartmental models into equivalent eIF models (Fourcaud-Trocmé et al., 2003), closely following the work of Gerstner and collaborators (Badel et al., 2008a, 2008b). As a proof of principle, we restricted our efforts to the BAS models. Thus, for each soma-AIS distance d in the BAS model, a new set of eIF parameters was identified by fitting the eIF's current-voltage relationship $f(V_{soma})$, known analytically, to the current-voltage relationship of the BAS model, known numerically, while injecting the same noisy waveform in both models (i.e., $I_1 = 0$, Figure 4.6):

$$f(V_{soma}) = \frac{1}{\tau_m} (E_L - V_{soma} + \Delta_T e^{(V_{soma} - V_T)/\Delta_T}) \quad (4.5)$$

Thus, the eIF free parameters C_m , τ_m , E_L , Δ_T and V_T could be set to best approximate the current-voltage relationship from the BAS simulations, measured as

$$f(V_{soma}) = \langle \frac{d}{dt} V_{soma} - I/C_m \rangle_{V_{soma}} \quad (4.6)$$

where the average operator is applied for each value of the somatic voltage V_{soma} . The model parameters obtained by the fitting procedure for eIF neurons are given in Table 4.3.

The remaining parameters were: membrane capacitance $C_m = \tau_m$, $g_L = 14$ pF, and the reset potential $V_{reset} = -80$ mV. The eIF also featured an absolute refractory period $t_{ref} = 2$ ms. We repeated the same optimization procedure for a set of different positions of the AIS along the axon, and each time we obtained a distinct set of eIF model parameters. In particular, such a systematic optimization resulted in a distinct set of values for the eIF parameter Δ_T , which describes in eIF models the rapidity of the AP at its onset.

4.7.5 Liquid State Machine: the classification task

We implemented a recurrent network of eIF model neurons, composed of 1000 excitatory and 250 inhibitory units (parameters are given in Table 4.4).

Each neuron received current-based synaptic inputs from C_E presynaptic excitatory and C_I inhibitory neurons, randomly chosen. The network further received feed-forward inputs from a series of external units that projected to C_{in} randomly chosen excitatory neurons. The weights of all synaptic connections were drawn from a Gaussian random distribution with mean J^* and standard deviation $0.7J^*$, except for feed-forward input synapses that were uniformly distributed in the range $[0.5J_{in}, 1.5J_{in}]$. Each neuron additionally received noisy background synaptic inputs, modeled implicitly as a Poisson process (rate: 20 event/s, $J_{noise} = 2$ nA). All excitatory synapses had propagation delays, drawn uniformly from (1, 10) ms for excitatory and from (0.1, 2) ms for inhibitory synapses. Synaptic transmission was modelled as additive currents, characterized by an instantaneous rise time and an exponential decay (time constant: 3 ms for excitatory inputs, 2 ms for inhibitory inputs). Finally, all recurrent connections experienced short-term depression and facilitation (Maass et al., 2002; Markram et al., 1998), where the efficacy of a synapse at the time of the n -th spike was determined by the base weight w_0 , a recovery state variable R_n and an utilization state variable u_n according to

$$w_n = w_0 R_n u_n . \quad (4.7)$$

The recovery and the utilization terms R_n and u_n were updated each time a presynaptic spike occurred, using the following iterative expressions:

$$R_1 = 1 \quad (4.8)$$

$$R_n = U + u_{n-1}(1 - U)\exp\left(-\frac{\Delta t}{F}\right) \quad (4.9)$$

and

$$u_1 = U \quad (4.10)$$

$$u_n = 1 + (R_{n-1} - R_{n-1}u_{n-1} - 1)\exp\left(-\frac{\Delta t}{D}\right) \quad (4.11)$$

where Δt is the inter-spike interval, U is the utilization of synaptic resources for a single spike, and where F and D are the time constants for facilitation and depression processes, respectively. The parameters for each

synapse type (Table 4.4) were chosen according to empirical data (Gupta et al., 2000), as in (Maass et al., 2002).

connection	J (nA)	w_0 (nA)	U	D (ms)	F (ms)	Δ_{syn} (ms)	deg.	C
in	8.9	$\sim \mathcal{U}(0.5J, 1.5J)$				$\sim \mathcal{U}(1,10)$	Out-degree	70
EE	1.9	$\sim \mathcal{N}(J, 0.7J)$	0.59	813	1	$\sim \mathcal{U}(1,10)$	in-degree	28
EI	6.7	$\sim \mathcal{N}(J, 0.7J)$	0.049	399	1790	$\sim \mathcal{U}(1,10)$	in-degree	28
IE	6.1	$\sim \mathcal{N}(J, 0.7J)$	0.016	45	376	$\sim \mathcal{U}(0.1,2)$	in-degree	48
II	4.9	$\sim \mathcal{N}(J, 0.7J)$	0.25	706	21	$\sim \mathcal{U}(0.1,2)$	in-degree	48

Table 4.4. Connection parameters. $\mathcal{N}(\mu, \sigma)$ denotes a normal distribution with mean μ and standard deviation σ . $\mathcal{U}(a, b)$ denotes a uniform distribution in $[a, b]$. The last column denotes whether connections are drawn with a fixed indegree or a fixed outdegree per neuron.

To obtain a well-performing network, we optimized the connectivity parameters (C_E , C_I , C_{in} , see last column in Table 4.4) and the connection weight-means (J_{EE} , J_{EI} , J_{IE} , J_{II} , J_{in} , second column in Table 4.4) using the eIF model corresponding to an AIS located at a distance of 25 μm from the soma (i.e. half of the range of considered values). We then investigated how the network performance changed when using eIF models fitted to models with different AIS locations.

The states of the network (i.e. the “liquid states”) were extracted from 200 randomly chosen excitatory neurons by filtering their AP trains with an exponential kernel (time constant of 20 ms). This extraction was repeated every 50 ms at the end of each epoch of external stimulation.

We trained the network to perform a delayed XOR on spike pre-defined templates. In each template presentation, 10 input units fired at predefined times (generated from a Poisson point process with rate 20 event/s) over an overall duration of 50 ms. The network was presented with jittered versions of these AP templates, where each input neuron activation time was shifted by a random number drawn from a Gaussian distribution with zero mean and standard deviation of 5 ms. These jittered templates were presented to the network in random order (Figure 4.7A-C). We trained linear readout units on the network state to generate as output an XOR of the identity of the two last patterns.

The training of the readouts was carried out by running the network for 500 s, and then randomly splitting the sequence of resulting states into a training set (80%), used to train one linear classifier, and into a test set (20%), used for performance evaluation. For each run, we trained 100 classifiers for different random training/test splits, this allowed for a more robust performance estimation. We used the mean performance as the result of one run.

We then tested the LSM performance using all eIF models, i.e., we investigated the influence of AIS position on the network performance. As the performance of an LSM can significantly depend on the exact wiring (which is randomly drawn), we generated $N = 50$ networks (i.e. different randomly drawn connectivity, weights, and synaptic delays) and tested each eIF model on all such networks. This resulted in 50 performance values for each AIS position. For the efficiency of the LSM, we report mean and standard deviations of these results. The p-values were computed using the Wilcoxon rank-sum test (Figure 4.7E).

We performed additional experiments to verify the robustness of these results (Figure C in S1 Supporting Information Figure 2). In order to test whether the AP sharpness has a significant influence on network performance, we evaluated the network performance using the neuron parameters obtained via fitting at a soma-AIS distance of 25 μm while

varying solely Δ_T in the value range found by the fitting method (see Results, Figure C, panel A, in S1 Supporting Information Figure 2A). In the reported simulations, we used longer delays for excitatory synapses in order to account for faster responses of inhibitory neurons. To test whether this choice influences our results, we repeated the complete experimental procedure (network parameter optimization and evaluation of network performance at different soma-AIS distances) using equal delays for excitatory and inhibitory connections (i.e., all synaptic delays were drawn from uniform distributions in [0.1, 2] ms). While this resulted in an overall decrease of performance, there was no qualitative change of the differential behavior for different soma-AIS distances (Figure C, panel B, in S1 Supporting Information Figure 2B). In our simulations, we optimized network parameters for an intermediate soma-AIS distance of 25 μm . In order to test whether this choice influences the results, we finally repeated the experimental procedure but optimized the network parameters for a soma-AIS distance of 0 μm , i.e., at a distance where we found the network to perform worst. The results were similar to those obtained by the optimization for a distance of 25 μm (Figure C, panel C, in S1 Supporting Information Figure 2C).

4.8 Data availability

Relevant simulation scripts are available at FigShare.com as <https://dx.doi.org/10.6084/m9.figshare.12123279>.

4.9 Acknowledgments

We thank Dr. D. Linaro for discussions and assistance and the anonymous reviewers for their constructive criticism and help to improve the paper. The computational resources and services used in this work were provided by the VSC (Flemish Supercomputer Center).

4.10 References

- Badel L, Lefort S, Brette R, Petersen CCH, Gerstner W, Richardson MJE. 2008a. Dynamic I-V Curves Are Reliable Predictors of Naturalistic Pyramidal-Neuron Voltage Traces. *J Neurophysiol* **99**:656–666. doi:10.1152/jn.01107.2007
- Badel Laurent, Lefort Sandrine, Berger Thomas K, Carl ·, Petersen CH, Gerstner W, Richardson Magnus J E, Badel L, Gerstner · W, Berger T K, Lefort S, Petersen · C C H, Richardson M J E. 2008b. Extracting non-linear integrate-and-fire models from experimental data using dynamic I-V curves. *Biol Cybern* **99**:361–370. doi:10.1007/s00422-008-0259-4
- Baranauskas G, David Y, Fleidervish IA. 2013. Spatial mismatch between the Na⁺ flux and spike initiation in axon initial segment. *Proc Natl Acad Sci U S A* **110**:4051–4056. doi:10.1073/pnas.1215125110
- Boucsein C, Tetzlaff T, Meier R, Aertsen A, Naundorf B. 2009. Brief Communications Dynamical Response Properties of Neocortical Neuron Ensembles: Multiplicative versus Additive Noise. doi:10.1523/JNEUROSCI.3424-08.2009
- Brette R. 2013. Sharpness of Spike Initiation in Neurons Explained by Compartmentalization. *PLoS Comput Biol* **9**. doi:10.1371/journal.pcbi.1003338
- Buonomano D V., Maass W. 2009. State-dependent computations: spatiotemporal processing in cortical networks. *Nat Rev Neurosci* **10**:113–125. doi:10.1038/nrn2558
- Carnevale NT, Hines ML. 2006. The NEURON book, The NEURON Book. Cambridge University Press. doi:10.1017/CBO9780511541612
- Destexhe A, Rudolph M, Paré D. 2003. The high-conductance state of neocortical neurons in vivo. *Nat Rev Neurosci* **4**:739–751. doi:10.1038/nrn1198
- Eyal G., Mansvelder HD, de Kock CPJ, Segev I. 2014. Dendrites Impact the Encoding Capabilities of the Axon. *J Neurosci* **34**:8063–8071. doi:10.1523/jneurosci.5431-13.2014
- Eyal Guy, Mansvelder HD, de Kock CPJ, Segev I. 2014. Dendrites impact the encoding capabilities of the axon. *J Neurosci* **34**:8063–8071. doi:10.1523/JNEUROSCI.5431-13.2014

- Fourcaud-Trocmé N, Hansel D, van Vreeswijk C, Brunel N. 2003. How spike generation mechanisms determine the neuronal response to fluctuating inputs. *J Neurosci* **23**:11628–11640. doi:23/37/11628 [pii]
- Fourcaud N, Brunel N. 2002. Dynamics of the firing probability of noisy integrate-and-fire neurons. *Neural Comput* **14**:2057–2110. doi:10.1162/089976602320264015
- Gillespie DT. 1996. Exact numerical simulation of the Ornstein-Uhlenbeck process and its integral. *Phys Rev E - Stat Physics, Plasmas, Fluids, Relat Interdiscip Top* **54**:2084–2091. doi:10.1103/PhysRevE.54.2084
- Goriounova NA, Heyer DB, Wilbers R, Verhoog MB, Giugliano M, Verbist C, Obermayer J, Kerkhofs A, Smeding H, Verberne M, Idema S, Baayen JC, Pieneman AW, de Kock CP, Klein M, Mansvelder HD. 2018. Large and fast human pyramidal neurons associate with intelligence. *Elife* **7**. doi:10.7554/eLife.41714
- Grubb MS, Burrone J. 2010. Activity-dependent relocation of the axon initial segment fine-tunes neuronal excitability. *Nature* **465**:1070–1074. doi:10.1038/nature09160
- Gupta A, Wang Y, Markram H. 2000. Organizing principles for a diversity of GABAergic interneurons and synapses in the neocortex. *Science (80-)* **287**:273–278. doi:10.1126/science.287.5451.273
- Hamada MS, Goethals S, De Vries SI, Brette R, Kole MHP. 2016. Covariation of axon initial segment location and dendritic tree normalizes the somatic action potential. *Proc Natl Acad Sci U S A* **113**:14841–14846. doi:10.1073/pnas.1607548113
- Hasson U, Chen J, Honey CJ. 2015. Hierarchical process memory: Memory as an integral component of information processing. *Trends Cogn Sci*. doi:10.1016/j.tics.2015.04.006
- Hines ML, Carnevale NT. 2001. NEURON: a tool for neuroscientists. *Neuroscientist* **7**:123–35. doi:10.1177/107385840100700207
- Ilin V, Malyshev A, Wolf F, Volgushev M. 2013. Fast computations in cortical ensembles require rapid initiation of action potentials. *J Neurosci* **33**:2281–2292. doi:10.1523/JNEUROSCI.0771-12.2013
- Kole MH, Brette R. 2018. The electrical significance of axon location diversity. *Curr Opin Neurobiol*. doi:10.1016/j.conb.2018.02.016
- Köndgen H, Geisler C, Fusi S, Wang XJ, Lüscher HR, Giugliano M. 2008.

The dynamical response properties of neocortical neurons to temporally modulated noisy inputs in vitro. *Cereb Cortex* **18**:2086–2097. doi:10.1093/cercor/bhm235

Kuba H. 2010. Plasticity at the axon initial segment. *Commun Integr Biol* **3**:597–598. doi:10.4161/cib.3.6.13242

Linaro D, Biró I, Giugliano M. 2018. Dynamical response properties of neocortical neurons to conductance-driven time-varying inputs. *Eur J Neurosci* **47**:17–32. doi:10.1111/ejn.13761

Lundstrom BN, Higgs MH, Spain WJ, Fairhall AL. n.d. Fractional differentiation by neocortical pyramidal neurons. doi:10.1038/nn.2212

Maass W, Natschläger T, Markram H. 2002. Real-time computing without stable states: A new framework for neural computation based on perturbations. *Neural Comput* **14**:2531–2560. doi:10.1162/089976602760407955

Markram H, Muller E, Ramaswamy S, Reimann MW, Abdellah M, Sanchez CA, Ailamaki A, Alonso-Nanclares L, Antille N, Arsever S, Kahou GAA, Berger TK, Bilgili A, Buncic N, Chalimourda A, Chindemi G, Courcol JD, Delalondre F, Delattre V, Druckmann S, Dumusc R, Dynes J, Eilemann S, Gal E, Gevaert ME, Ghobril JP, Gidon A, Graham JW, Gupta A, Haenel V, Hay E, Heinis T, Hernando JB, Hines M, Kanari L, Keller D, Kenyon J, Khazen G, Kim Y, King JG, Kisvarday Z, Kumbhar P, Lasserre S, Le Bé JV, Magalhães BRC, Merchán-Pérez A, Meystre J, Morrice BR, Muller J, Muñoz-Céspedes A, Muralidhar S, Muthurasa K, Nachbaur D, Newton TH, Nolte M, Ovcharenko A, Palacios J, Pastor L, Perin R, Ranjan R, Riachi I, Rodríguez JR, Riquelme JL, Rössert C, Sfyarakis K, Shi Y, Shillcock JC, Silberberg G, Silva R, Tauheed F, Telefont M, Toledo-Rodriguez M, Tränkler T, Van Geit W, Díaz JV, Walker R, Wang Y, Zaninetta SM, Defelipe J, Hill SL, Segev I, Schürmann F. 2015. Reconstruction and Simulation of Neocortical Microcircuitry. *Cell* **163**:456–492. doi:10.1016/j.cell.2015.09.029

Markram H, Wang Y, Tsodyks M. 1998. Differential signaling via the same axon of neocortical pyramidal neurons. *Proc Natl Acad Sci U S A* **95**:5323–5328. doi:10.1073/pnas.95.9.5323

Naundorf B, Wolf F, Volgushev M. 2006. Unique features of action potential initiation in cortical neurons. *Nature* **440**:1060–1063. doi:10.1038/nature04610

- Öz P, Huang M, Wolf F. 2015. Action potential initiation in a multi-compartmental model with cooperatively gating Na channels in the axon initial segment. *J Comput Neurosci* **39**:63–75.
doi:10.1007/s10827-015-0561-9
- Tchumatchenko T, Malyshev A, Wolf F, Volgushev M. 2011. Ultrafast population encoding by cortical neurons. *J Neurosci* **31**:12171–12179.
doi:10.1523/JNEUROSCI.2182-11.2011
- Telenczuk M, Fontaine B, Brette R. 2017. The basis of sharp spike onset in standard biophysical models. *PLoS One* **12**:e0175362.
doi:10.1371/journal.pone.0175362
- Testa-Silva G, Verhoog MB, Linaro D, de Kock CPJ, Baayen JC, Meredith RM, De Zeeuw CI, Giugliano M, Mansvelder HD. 2014. High Bandwidth Synaptic Communication and Frequency Tracking in Human Neocortex. *PLoS Biol* **12**:e1002007.
doi:10.1371/journal.pbio.1002007
- Tsodyks M, Pawelzik K, Markram H. 1998. Neural Networks with Dynamic Synapses. *Neural Comput* **10**:821–835.
doi:10.1162/089976698300017502
- Yu Y, Shu Y, McCormick DA. 2008. Cortical Action Potential Backpropagation Explains Spike Threshold Variability and Rapid-Onset Kinetics. *J Neurosci* **28**:7260–7272.
doi:10.1523/JNEUROSCI.1613-08.2008

CHAPTER 5

Homogeneous and narrow bandwidth of spike initiation in rat L1 cortical interneurons

Frontiers in Cellular Neuroscience, 2020

5.1 Chapter Information

5.1.1 Publication

Stefano Borda Bossana*, **Christophe Verbist***, Michele Giugliano. *Front. Cell. Neurosci.*, doi: 10.3389/fncel.2020.00118

*Equally contributing authors

5.1.2 Author contribution

Conceived and designed the research: M.G. Performed the experiments: S.B.B. Performed the simulations: C.V. Analysed the data: S.B.B. and C.V. Wrote the paper: S.B.B., C.V., and M.G.

5.2 Abstract

Cortical layer 1 contains a population of GABAergic interneurons, considered a key component of information integration, processing, and relaying in neocortical networks. In fact, L1 interneurons combine top-down information with feed-forward sensory inputs in layer 2/3 and 5 pyramidal cells, while filtering their incoming signals. Despite L1 importance for network emerging phenomena, little is known on the dynamics of the spike initiation and encoding properties of its neurons. Using acute brain tissue slices from the rat neocortex, combined with the analysis of an existing database of model neurons, we investigated the dynamical transfer properties of these cells, sampling the entire population of known “electrical classes”, and comparing experiments and model predictions. We found the bandwidth of spike initiation to be significantly narrower than in L2/3 and 5 pyramidal cells, with values below 100 *cycle/s*, but without significant heterogeneity in the cell response properties, across distinct electrical types. The upper limit of the neuronal bandwidth was significantly correlated to the mean firing rate, as anticipated from theoretical studies but not reported for pyramidal cells. Finally, at high spectral frequencies, the magnitude of the neuronal response attenuated as a power-law, with an exponent significantly smaller than what reported for pyramidal neurons and reminiscent of the dynamics of a “leaky” integrate-and-fire model of spike initiation. Finally, most of our *in vitro* results matched quantitatively the numerical simulations of the models, as a further contribution to independently validate the models against novel experimental data.

5.3 Introduction

Layer 1 (L1) is the most superficial neocortical layer and holds a key role in the hierarchy of information processing within neocortical networks. It contains a resident population of interneurons, which are solely GABAergic in the mature neocortex (Gentet, 2012; Hestrin and Armstrong, 1996). They receive afferents from a variety of brain areas, including primary and higher order thalamic relays, cortico-cortical projections, as well as neuromodulatory afferents from subcortical structures. Thanks to this convergence, it was suggested that L1 interneurons might integrate top-down information with feedforward sensory inputs, filter out the noise in the incoming signals, and convert them into local inhibition (Larkum, 2013; Schuman et al., 2019). From L1, information is then transferred to pyramidal cells (PCs) of layer 2/3 (L2/3) and of layer 5 (L5) via two distinct microcircuits, which can either promote or inhibit the generation of dendritic spikes (Jiang et al., 2013). Hence, L1 interneurons may play a pivotal role as modulating, in a state-dependent manner, the coincidence detection mechanism that ensures amplification and further processing of attentional signals by PCs (D'Souza and Burkhalter, 2017; Larkum and Zhu, 2002; Zhu and Zhu, 2004).

However, as opposed to L2/3 and L5 pyramidal cells, the excitable properties of interneurons have not yet been examined systematically, in terms of dynamical firing regimes (but see Linaro et al., 2019; Merino et al., 2019). Within neocortical networks of layers 2/3 and 5, we already know that information encoding and transfer feature wide-bandwidth dynamics. These performances are ensured by the rapid onset dynamics of action potentials, which allow neuronal populations to collectively phase-lock their instantaneous firing rate to the fast-varying Fourier components of the input signals (200 – 1000 *cycle/s*) (Goriounova et al., 2018; Linaro et al., 2018). In analogy to electrical filters, the upper limit to such broad neuronal bandwidth is referred to as *cutoff frequency* (Brunel et al., 2001; Fourcaud-Trocmé et al., 2003), which has been experimentally measured in L2/3 and L5 pyramidal neurons upon identification of the *dynamical transfer function* of those cells (Boucsein et al., 2009; Goriounova et al., 2018; Ilin et al., 2013; Köndgen et al., 2008; Linaro et al., 2018).

For L1, we know that several subpopulations of L1 interneurons can be distinguished on the basis of their firing in response to constant amplitude currents (Muralidhar et al., 2014), displaying quite heterogeneous electrical phenotypes. Nonetheless, it is still not clear how these different electrical signatures contribute to distinct properties in the network dynamics of information processing within L1.

In this work, by means of whole-cell patch clamp recordings in rodent acute brain tissue slices, we examined L1 interneurons *in vitro* and identified their electrical phenotype as well as their dynamical transfer function. We quantified how L1 cells' firing output is influenced by a temporal modulation of their input, namely described in the Fourier domain the cells' filter properties of incoming input signals. Allowing a comparison with previous studies in principal cells, we specifically adopted a simple and established experimental protocol (Higgs and Spain, 2009; Ilin et al., 2013). This is equivalent (Tchumatchenko and Wolf, 2011) to our previous probing strategy of dynamical excitable properties of cortical neurons (Köndgen et al., 2008; Linaro et al., 2018). Importantly, we showed earlier that cutoff frequency and bandwidth are features that are independent on the parameters of the injected currents and the firing regimes (Linaro et al., 2018).

Given the impact that L1 interneurons have on the output of PCs, characterising their dynamical response properties is highly relevant and timely to clarify how information integration, processing, and transfer take place to select behaviourally-relevant signals. Finally, a set of previously released multicompartmental mathematical models of L1 interneurons (Markram et al., 2015) was studied under the same stimulation protocols as *in vitro*, aiming at further validating them and at supporting the interpretation of the experimental data.

5.4 Materials and Methods

5.4.1 Brain tissue slice preparation

Experiments were performed as described previously (Arsiero et al., 2007; Köndgen et al., 2008) and in accordance with international and institutional guidelines on animal welfare. All procedures were approved by the Ethical Committee of the University of Antwerp (permission no. 2011_87) and licensed by the Belgian Animal, Plant and Food Directorate-General of the Federal Department of Public Health, Safety of the Food Chain and the Environment (license no. LA1100469).

14–21 days old Wistar rats of either sex were anaesthetised using Isoflurane and decapitated. Brains were rapidly extracted and immersed in bubbled ice-cold artificial cerebrospinal fluid (ACSF) containing (in mM) 125 NaCl, 25 NaHCO₃, 2.5 KCl, 1.25 NaH₂PO₄, 2 CaCl₂, 1 MgCl₂, 25 glucose, saturated with 95% O₂ and 5% CO₂, and having a pH of 7.3 and osmolarity of ~315 mOsm. 300 μ m thick parasagittal slices were then cut from the primary somatosensory cortex using a vibratome (VT1000 S, Leica Microsystems GmbH, Germany) and incubated in ACSF at 36 °C for 30 min.

After recovery, slices were stored in ACSF at room temperature in a holding chamber until recordings started. Once placed in the recording chamber, constituting the stage of an upright microscope, L1 cells were visualised with infrared differential interference contrast microscopy (DIC), under 40x magnification. All experiments were performed in submerged conditions at a temperature of 32 °C, under continuous perfusion with oxygenated ACSF.

5.4.2 Electrophysiology

Layer 1 cells were selected on the basis of their distance from the pia mater and from the border with L2/3, which was identified as an increase in the density of cell somata, located approximately 100 μ m away from the pia mater. Within this region, the whole-cell patch-clamp configuration was established from the cell soma, and the neuronal response properties probed in the current-clamp mode. Filamented borosilicate glass pipettes were prepared using a micropipette horizontal puller (P-97, Sutter Instruments, Novato, CA, USA) and had a resistance of 4–7 M Ω when filled with an intracellular solution containing (in mM): 115 K-gluconate, 20 KCl, 10 4–

(2-hydroxyethyl)-1-piperazineethanesulfonic acid (HEPES), 4 adenosine triphosphate-Mg, 0.3 Na²-guanosine triphosphate, 10 Na²-phosphocreatine, with a pH adjusted to 7.3 with KOH and osmolarity of ~290 mOsm.

Recordings and intracellular current stimulation were performed using an Axon Multiclamp 700B Amplifier (Molecular Devices, USA) controlled by a personal computer running a real-time Linux operating system (Linaro et al., 2014). For more information on how to install our real-time software see (Linaro et al., 2015). Recorded voltage waveforms were sampled at a frequency of 30 kHz and digitized at 16 bit. In order to compensate for the glass pipette electrical resistance and capacitance, a digital non-parametric model was repeatedly identified throughout the recording sessions, by a computer-aided technique, known as *active electrode compensation* (Brette et al., 2008a). This allowed us to digitally separate the electrode and membrane contributions to the recorded traces, requiring neither the bridge balance nor capacitance neutralisation circuits of the amplifier. The adoption of such a technique became a routine procedure in our laboratory, for both conventional and real-time experiments (Couto et al., 2015; Linaro et al., 2019, 2018). However, while for dynamic clamp an online accurate “active” electrode compensation is necessary to avoid recording instabilities (Brette et al., 2008b; Linaro et al., 2019), for current clamp – in the context of the present work – it is not strictly required. In fact, on one hand we focused here on probing the dynamical transfer function of neurons in current-clamp mode by spike-triggered averaging (see below), so that an accurate *active electrode compensation* was not imperative. Indeed, despite using a single electrode for both stimulation and recordings, only the times of AP occurrence must be detected for further analysis (see below). Such a detection occurs by definition with a very high signal-to-noise ratio and it usually does not represent a problem, even with an imperfect electrode compensation. On the other hand, estimating the features of AP waveforms definitely benefits of a more accurate (non-parametric) compensation procedure than the (parametric) one allowed by the electronic amplifier controls. Finally, postponing the compensation of all acquired traces to an offline automated procedure ultimately offered us an efficient management of time during each experiment, while only requiring to periodically run a “calibration” protocol (Linaro et al., 2015).

5.4.3 Electrical phenotype identification

The recorded voltage traces were processed and analysed offline in MATLAB (The MathWorks, Natick MA, USA). Data from $N = 65$ L1 interneurons were included in this study, selected on the basis of a healthy cell resting membrane potential ($< -65\text{mV}$) and AP peak amplitude ($> 50\text{mV}$). These criteria were considered to be indicative of a good patch stability and proper electrical access to the cell. The membrane input resistance, capacitance, and time constant were estimated by standard procedures (Köndgen et al., 2008). Briefly, hyperpolarising current steps of decreasing amplitudes (i.e. $[-200; 0]\text{ pA}$ lasting 1 s each) were repeatedly applied and voltage response was recorded. The membrane input resistance was then identified as the slope of the best-fit straight line to the steady-state data points in the voltage *versus* current plane. The membrane time constant was instead extracted as the slowest time constant of the best-fit bi-exponential function, describing the recovery of the membrane potential from 10 ms -long hyperpolarising pulses of amplitude -150 pA . The cell capacitance was finally estimated as the ratio between the time constant and the input resistance of the membrane.

Each recorded neuron was classified in one of the five identified subtypes, on the basis of their response to depolarising current pulses (Muralidhar et al., 2014). Briefly, a *frequency-current* curve was first computed upon injecting current steps of increasing depolarising amplitudes (i.e. in the range $[0; 300]\text{ pA}$, lasting 1 s). The voltage responses containing a train of action potentials (APs), corresponding to a mean firing rate of 20 spike/s , were compared to each other as the sequence of successive inter-spike intervals (ISI) was plotted (Figure 5.1a). Sorting each cell into one of the five classes (i.e. cAC: continuous accommodating, cNAC: continuous non-accommodating, bNAC: bursting non-accommodating, cSTUT: continuous stuttering, and cIR: continuous irregular firing) was performed manually, following closely (Muralidhar et al., 2014) and according to the following criteria: - cAC, if the slope of the best-fit straight line over the ISI sequence was larger than 1 ms ; - cNAC: if the best-fit line was mostly horizontal (i.e. slope smaller than 1 ms); - bNAC: if the initial 1-2 ISIs were shorter than 20 ms and followed by a train of APs showing no accommodation; - cSTUT: if at least one ISI was equal or larger than 100 ms ; - cIR: if the ISI

sequence was irregular, with individual values shorter than 100 ms. The above criteria led to classifying 11 cells as cAC, 13 as cNAC, 10 as bNAC, 17 as cSTUT, and 14 as cIR (Figure 5.1a).

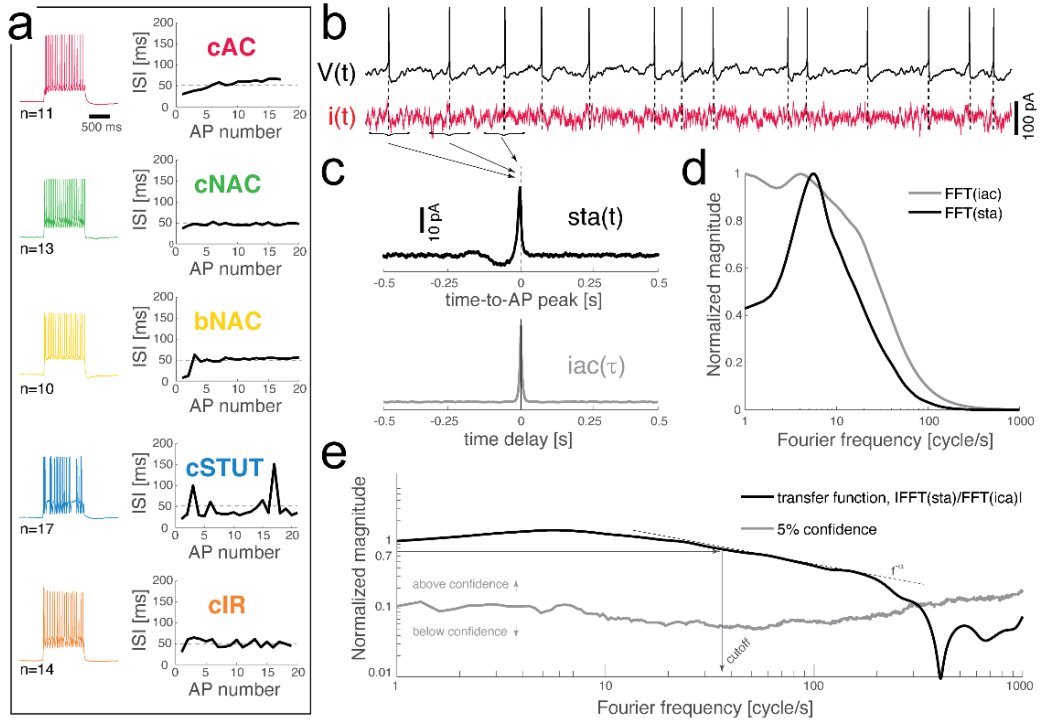


Figure 5.1. Dynamical transfer function identification, in L1 cortical interneurons Distinct subtypes of L1 interneurons can be distinguished (a) from their electrical response pattern, by the sequence of interspike intervals (ISIs) in a 20 spike/s train. These are: continuous accommodating (cAC), c. non-accommodating (cNAC), bursting non- accommodating (bNAC), c. stuttering (cSTUT) and c. irregular (cIR). Regardless of their identity, neurons were stimulated by a fluctuating current $i(t)$ (b) while recording their voltage response $V(t)$. The spike-triggered average (i.e. $sta(t)$) of the stimulus and its autocorrelation function (i.e. $iac(\tau)$) were computed (c) and fast Fourier-transformed (d) to estimate the neuron dynamical transfer function (e). As in electronic filters, the magnitude of this function expresses the intensity of the output firing rate of the cell, across temporal modulations or Fourier components of an input signal, thus revealing the bandwidth of spike initiation dynamics. The cutoff was characterised – above significance (see the Methods) – as the frequency corresponding to a 70% decrease of the response magnitude of the value taken at 1 cycle/s. The high-frequency profile was finally described as a $f^{-\alpha}$ power law.

5.4.4 Spike-triggered average and dynamical transfer function

Wide-band input current waveforms $i(t)$ were injected into the cell soma, in order to probe their first-order dynamical transfer properties, following closely (Ilin et al., 2013) (see also Higgs and Spain, 2009). Under these conditions, neuronal firing is irregular and subthreshold membrane potential fluctuations resemble the activity recorded *in vivo* (Destexhe et al., 2003). The injected current was defined as the sum of a DC and of a fluctuating component (Figure 5.1b):

$$i(t) = i_0 + \sigma \eta(t)$$

with $\eta(t)$ being an independent realisation of an Ornstein–Uhlenbeck stochastic process (Cox and Miller, 1977) with zero mean, unitary variance, and correlation time $\tau = 5 \text{ ms}$. $\eta(t)$ was generated off-line, iterating an algebraic expression (Gillespie, 1996).

By such a definition, σ represents the standard deviation of the noisy fluctuation in $i(t)$, while i_0 is its expected value. In each experiment, σ was adjusted to obtain membrane potential fluctuations with 4 mV standard deviation and $\approx 15 \text{ mV}$ peak to peak changes. The value of i_0 was instead chosen to maintain the mean firing rate of the neurons in the range 3–6 spike/s. Each stimulation trial lasted 60 s and was preceded by brief current steps, monitoring over time the stability of the recording, i.e. in terms of resting potential, input resistance, and mean firing rate as in (Köndgen et al., 2008). The stimulation was repeated several times, with distinct realisations of $\eta(t)$, until at least 3500 APs in total were collected, while allowing sufficient inter-stimulus recovery intervals of up to 60–100 s, depending on the cell. This resulted in 18–20 repetitions, corresponding to approximately 40–45 min of recording in total.

We recorded the train of APs fired by the cell in response to the injected stimulus $i(t)$, evaluating offline the spike-triggered average $sta(t)$ of such a stimulus waveform. This analysis allows an estimate of the dynamical transfer function (Köndgen et al., 2008) in biological neurons as well as model neurons, and was performed following closely (Ilin et al., 2013). Briefly, $sta(t)$ was evaluated as the ensemble average of the data points of

$i(t)$ that shortly preceded and followed the peak of each AP fired, i.e. over the times $t_1, t_2, t_3, \dots, t_N$ of AP occurrences (Figure 5.1b-c):

$$sta(t) = \langle \sum_{k=1}^N i(t_k - t) \rangle \quad t \in [-T; T],$$

where $T = 500 \text{ ms}$ is the chosen time interval preceding and following each AP. This expression can be equivalently rewritten as an ensemble average of the convolution between $i(t)$ and a train of Dirac's delta functions $s(t)$ (i.e. one for each AP):

$$sta(t) = \langle \int_{-\infty}^{+\infty} s(\tau) i(\tau - t) d\tau \rangle, \quad s(t) = \sum_{k=1}^N \delta(t - t_k).$$

Invoking linearity and swapping integral and the average operators, we may derive another expression (Dayan and Abbott, 2005), linking $sta(t)$ to the instantaneous firing rate $r(t)$ associated to the AP train $s(t)$:

$$sta(t) = \int_{-\infty}^{+\infty} r(\tau) \langle i(\tau - t) \rangle d\tau$$

In the Fourier domain, this convolution integral simplifies as the product of the firing rate transform $R(f)$ and the average (complex conjugate) of the input transform $I^*(f)$:

$$STA(f) = R(f) \langle I^*(f) \rangle.$$

Finally, as $R(f)$ is also the product of the first-order dynamical transfer function $H(f)$ (Marmarelis and Naka, 1972) times the average input $\langle I(f) \rangle$ (Brunel et al., 2001),

$$R(f) = H(f) \langle I(f) \rangle,$$

the transfer function $H(f)$ (Figure 5.1e) can be computed as the ratio between the $sta(t)$ (fast) Fourier transform and the power spectral density of $i(t)$ (Figure 5.1c-d):

$$H(f) = STA(f) / \langle I(f) I^*(f) \rangle$$

where the power spectral density of $i(t)$ is the (fast) Fourier transform of its autocorrelation function $iac(\tau) = \langle i(t) i(t - \tau) \rangle$.

The profile of the transfer function was considered above a 5% confidence threshold (Figure 5.1e), generated by a bootstrap method on surrogate data (Press, 2007). Briefly, these were obtained upon generating 500 times a

random shuffling of the original interspike intervals and repeating each time the $sta(t)$ analysis in the Fourier domain. The confidence threshold was then computed at each frequency as the sum of the mean (surrogate) transfer function (i.e. over the 500 surrogate trials) and its (surrogate) standard deviation.

The *cutoff* frequency was then defined as the frequency at which the magnitude of the transfer function $||H(f)||$ (above the confidence threshold) decreases down to the 70% of the value it takes at 1 Hz (Figure 5.1e).

For very large Fourier frequencies f , the magnitude of the transfer functions decayed as a negative power law, i.e. $f^{-\alpha}$ (Fourcaud-Trocmé et al., 2003; Köndgen et al., 2008; Linaro et al., 2018). In order to best describe the input–output transformation of the neurons in this high spectral domain, the part of the transfer curves going from the cutoff frequency down to 20% of the cutoff value was fitted by a power-law $y = b x^{-\alpha}$ where α describes the slope of the decay in log-log coordinates.

5.4.5 Rapidness of the action potential at its onset

The average waveform of the action potential (AP) was examined for each cell by averaging the APs fired during the steady-state response regime of the recorded voltage responses. The threshold for AP initiation (in mV) was conventionally calculated as the potential where the change in voltage over time is $20 mV/ms$ (Naundorf et al., 2006). When plotted in the plane dV_m/dt versus V_m , each AP described a closed trajectory. The AP speed at onset (expressed in ms^{-1}) was then measured in this plane, as the slope of the tangent line to the AP trajectory at the voltage coordinate corresponding to the AP threshold.

The *dynamic IV curve* method was also employed to quantify the AP waveforms, relating the upstroke phase of an AP to the best-fit equation of a non-linear (i.e. exponential) relationship between dV_m/dt and V_m (Badel et al., 2008a, 2008b). From the resulting fit, the spike-slope factor Δ_T was extracted to further quantify the rapidness of the AP.

5.4.6 Computer simulations

The simulation of 69 distinct L1 interneuron models was performed in NEURON (Carnevale and Hines, 2006; Hines and Carnevale, 2001), using the publicly available Blue Brain Project (BBP) database (Markram et al., 2015). Each model was originally built from experimental data, collected from L1 neurons classified into the same electrical response phenotypes employed in this work (see also Ascoli et al., 2008).

We mimicked *in silico* the very same stimulation protocols and analysis employed *in vitro*, as close as possible. For the spike-triggered average estimate, we chose the parameters of the injected current $i(t)$ by means of an iterative procedure, based on the bisection method (Press, 2007). Given the increased reproducible character of simulated neuronal responses compared to experiments, by selecting I_0 we could set the firing rate of the models with higher precision. We then chose three regimes (3, 5, and 7 *spikes/s*) to cover the entire range obtained in our experiments (3–6 *spike/s*) with increased confidence. We repeated 60 s long stimulations *in silico* until a minimum of 5000 APs were collected, and we followed closely the analysis methods described in the previous sections.

5.4.7 Statistical analysis

All numerical data are presented as *mean* \pm *standard deviation*. Statistical analysis of all correlations between parameters was performed using the Pearson correlation test (Press, 2007), reporting the values of the correlation coefficient ρ and its p-value. The one-way analysis of variance by Kruskal-Wallis was employed (i.e. the MATLAB *kruskalwallis()* command) to reject the hypothesis at 1% significance that the observables extracted from distinct electrical phenotypes originate from the same probability density distribution. Finally, the qualitative comparisons between the distribution densities of cutoff frequencies, among different electrical phenotypes (Figure 5.3), was performed normalising the peak amplitudes of smoothed histograms by the kernel smoothing method (i.e. the MATLAB *histfit()* command).

5.4.8 Data availability

Relevant data sets and analysis scripts are available at FigShare.com as <https://dx.doi.org/10.6084/m9.figshare.12091047>.

5.5 Results

We describe the firing response properties of L1 cortical interneurons, based on a set of whole-cell patch-clamp recordings in $n = 65$ cells from slices of the rat somatosensory cortex. We studied systematically both passive and active membrane properties, revealing that cells had an input resistance of $184.40 \pm 51.15 M\Omega$, a membrane capacitance of $201.51 \pm 62.95 nF$, and a membrane time constant of $35.77 \pm 10.23 ms$ (see the Methods). When active response properties were studied, we identified distinct electrical phenotypes and sorted cells into 5 separate classes (Muralidhar et al., 2014). Such a classification was based on the analysis of the time course of the interspike intervals (ISIs) sequence, during ≈ 20 *spike/s* trains of action potentials (APs), in response to a current step lasting 1 s (Figure 5.1a).

5.5.1 Encoding properties of L1 interneurons

We studied the encoding properties of L1 interneurons by measuring their *dynamical transfer function* in the Fourier domain (Figure 5.1b-e). Following closely (Ilin et al., 2013), we injected randomly fluctuating current stimuli into the soma of the cells, mimicking the irregular and intense synaptic activity present *in vivo* in an intact cortex. A DC offset was also superimposed to the injected current, adapting its amplitude so that the output mean firing rate was in the range 3–6 *spike/s*. Under these conditions (see the Methods), cells fired irregularly (Figure 5.1b) with a coefficient of variation of 0.53 ± 0.09 for their distribution of ISIs. This stimulation protocol enabled us to measure the spike-triggered average waveform of the injected current ($sta(t)$) and compare it to its autocorrelation function ($iac(t)$), in the Fourier domain (Figure 5.1c-d). In fact, the ratio of the two quantities in the transformed domain immediately leads to an estimate of the dynamical transfer function (Figure 5.1e) (see the Methods) arising from the cell's spike initiation mechanisms.

Magnitude and phase of the transfer function, especially for large spectral frequencies, allow one to predict the collective dynamics of a neuronal population, in response to rapid external inputs (Fourcaud-Trocmé et al., 2003; Köndgen et al., 2008) as well as to interpret oscillatory regimes (Wang, 2010). Here we quantified the bandwidth of the neuronal transfer function, expressing the numerical value of the conventional high-frequency *cutoff* limit (see the Methods). The distribution of the *cutoff* frequencies demonstrates that in general L1 interneurons can encode fast-varying input signals up to 200 *cycle/s* (Figure 5.2a). However, differently from L2/3 and L5 pyramidal cells (Linaro et al., 2018; Testa-Silva et al., 2014) the majority (i.e. $\approx 65\%$) of L1 neurons unexpectedly display a *cutoff* below 100 *cycle/s*.

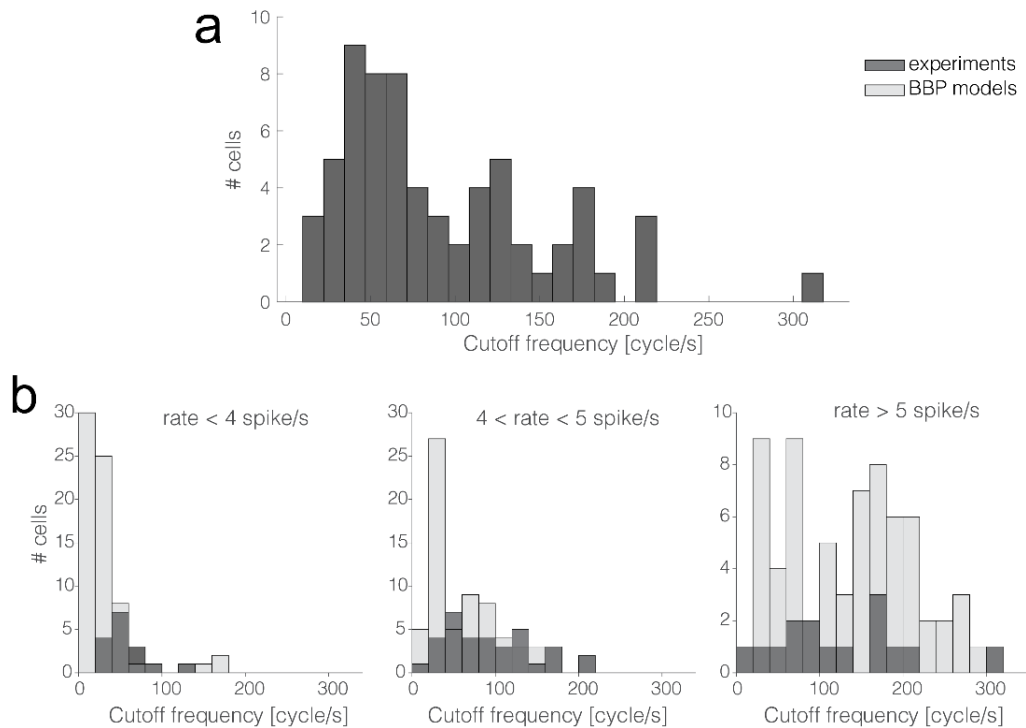


Figure 5.2. The cells' cutoff frequencies distribution. More than 60% of the 65 interneurons recorded in this work had their cutoff frequencies markedly below 100 *cycle/s* (a). The same trend was quantitatively confirmed *in silico*, repeating the same protocol of Figure 5.1b-e in 69 L1 neuron models (b), as released by the Blue Brain Project (BBP). Numerical simulations and experimental data were compared over three distinct ranges of experimental firing rates, where models were set to fire at precisely: 3, 5, and 7 *spike/s* (b, from left to right). The histogram overlay displays the rather good model predictions of the horizontal span of cutoff frequencies, over the three distinct firing rates.

These observations were confirmed *in silico* applying the experimental protocol of Figure 5.1b-e on a large public database of 69 detailed multicompartmental models of rat cortical L1 interneurons (see the Methods). At a reference mean firing rate of 5 *spike/s*, around 78% of the models display a *cutoff* frequency below 100 *cycle/s*. Figure 5.2b compares experimental and simulated data when the computer models were set to fire on average at (from left to right) 3, 5, and 7 *spike/s*. Under these conditions, the coefficients of variation of their respective ISI distributions were 0.74 ± 0.12 , 0.65 ± 0.12 and 0.58 ± 0.12 respectively for 3, 5 and 7 *spike/s* mean firing rates. Real cells were thus found in good agreement with the range of *cutoff* frequencies displayed by the models, when their firing rate was sorted in close intervals.

5.5.2 Electrical classes and encoding properties

When cells' electrical classes were explicitly taken into consideration, we found no preference in the *cutoff* frequency distributions (Figure 5.3a-b). Indeed, the probability distribution densities for each group of continuous accommodating (cAC), c. non-accommodating (cNAC), bursting non-accommodating (bNAC), c. stuttering (cSTUT) and c. irregular (cIR) showed substantial overlap (Figure 5.3a) and no significant differences were found (Figure 5.3b).

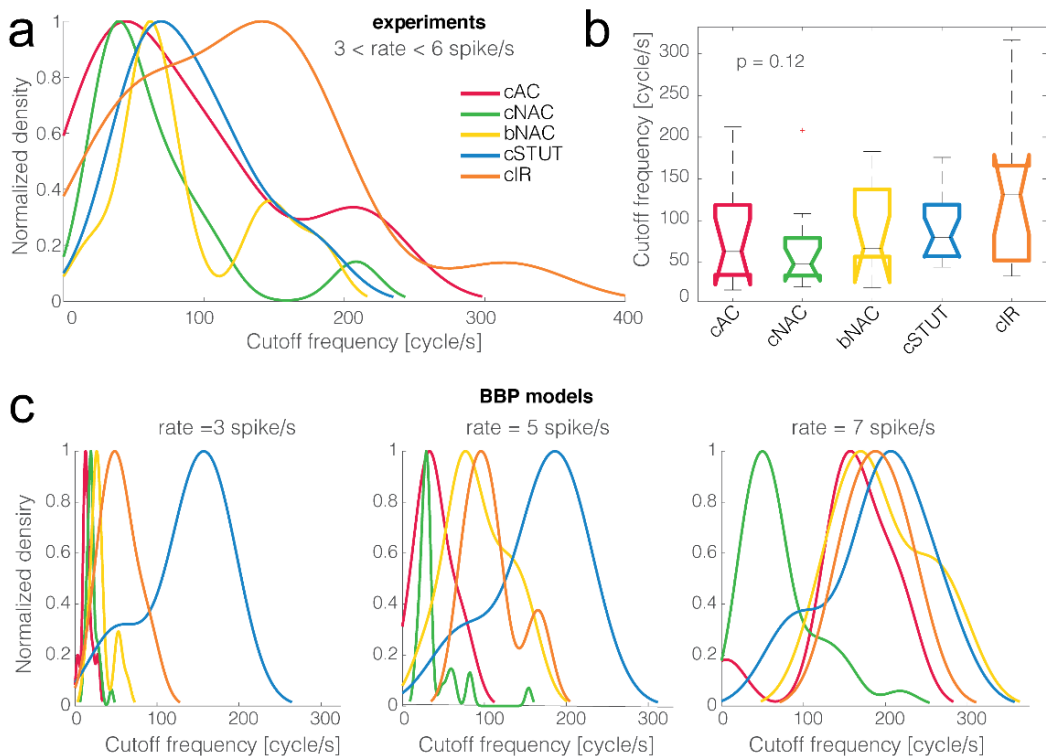


Figure 5.3. Cells' electrical phenotype and cutoff frequencies distributions. When the five distinct electrical classes of L1 interneurons were compared to each other, their (smoothed) probability density distributions of the cutoff frequencies, normalised by their peak values, showed no major differences (a). Quantitatively, the Kruskal-Wallis statistical test failed to reject at 1% significance level the null hypothesis that the cutoff frequencies come from the same distribution (b). A similar trend was largely reproduced *in silico*, for the BBP models (c).

The same analysis was repeated *in silico*, where the diversity of electrical (as well as morphological) phenotype is made explicit *a priori* by a distinct set of electrotonic and excitable properties (Markram et al., 2015). The model's electrical identity played a role in shaping, to some extent, the probability distribution densities of the cSTUT and the cNAC classes, in particular.

5.5.3 Dependency of *cutoff* on the mean firing rate

Previous theoretical investigations on the dynamical properties of spike initiation reported that, in Integrate-and-Fire neuron models, the *cutoff* frequency is sensitive to the mean firing rate. Thus, the higher the rate the wider the bandwidth (Brunel et al., 2001; Fourcaud-Trocmé et al., 2003). This was examined experimentally in L5 pyramidal cells but failed to be confirmed, as the mean firing rate altered the dynamical transfer function at

low, not high, spectral frequencies (Linaro et al., 2018). Despite the small range of our experimental firing rates, we asked whether L1 interneurons behave differently than pyramidal cells. We thus studied the correlation between *cutoff* frequency and the mean firing rate and found it to be very significantly correlated ($\rho = 0.48$, $p < 0.001$), as also exemplified in Figure 5.4a. This implies that the boundary in the Fourier domain where fast input signal components get filtered out increases considerably even with a moderate increase in the neuronal firing rate.

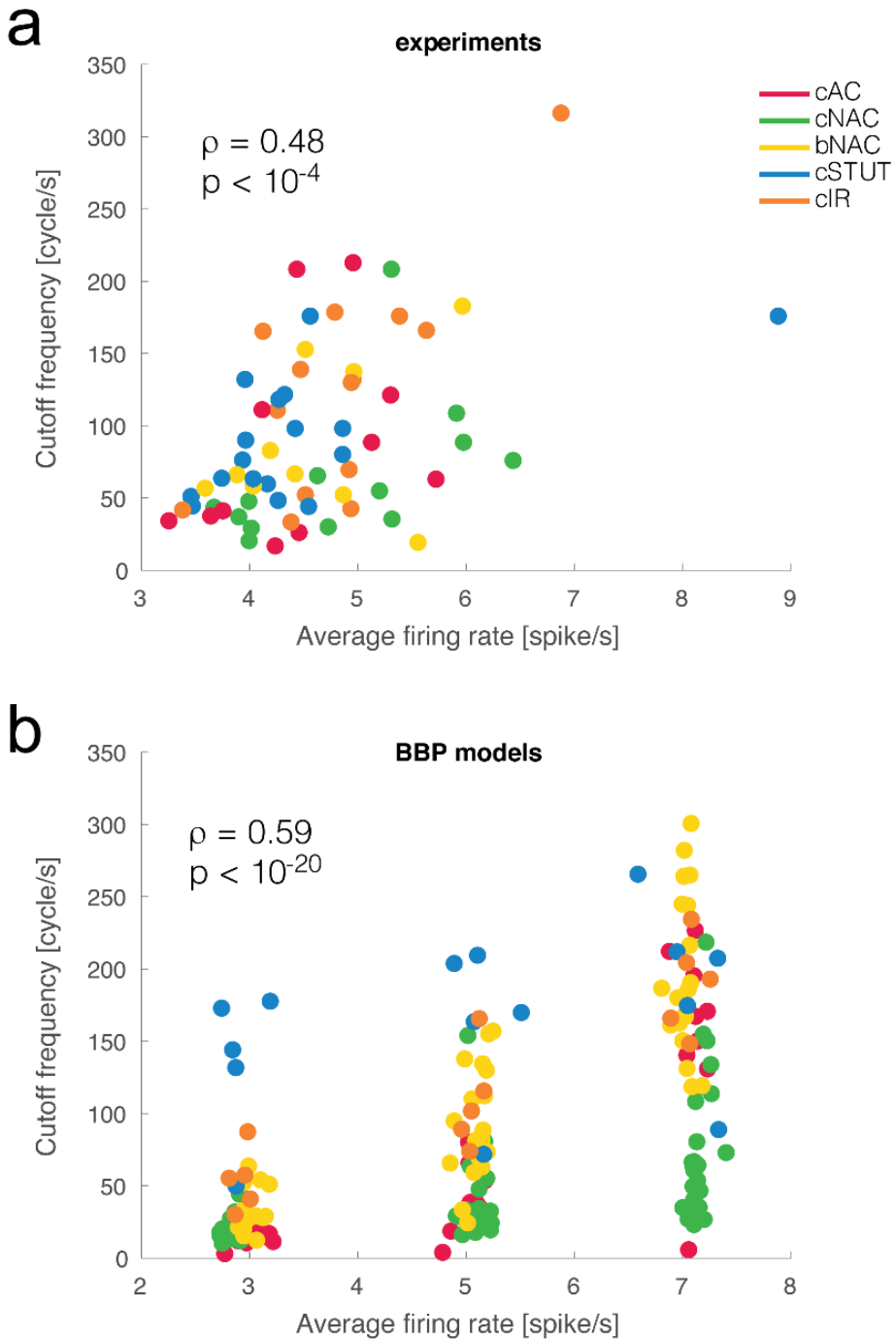


Figure 5.4. Mean firing rate modulation of the cutoff frequencies As suggested by earlier theoretical studies, a significant correlation was observed between the mean firing rate of a cell and the cutoff frequency of its dynamical transfer function (a). The very same result was reproduced in silico, for the BBP models (b).

When the analysis was repeated *in silico*, a similar phenomenon was replicated for the entire population of multicompartmental neuron models. There we found a similar correlation with a much stronger significance ($\rho = 0.58, p < 10^{-20}$) (Figure 5.4b). This effect is very apparent in the simulated experiment reported in Figure 5.4b, as most of electrical types progressively shift their *cutoff* frequency upwards for increasing firing rates. Such a susceptibility was further quantified by linear fitting the simulated data points at different firing rates, for each firing type. The slope of this fit was 34.57 *cycle/spike* for cAC, 11.96 for cNAC, 41.16 for bNAC, 11.43 for cSTUT, and 32.78 for cIR. This indicates that cSTUT and cNAC models were the least sensitive to their firing rate, while cAC, bNAC, and cIR were the most sensitive.

5.5.4 Action potential rapidity at onset

The broad bandwidth of the AP initiation dynamics has been related, in both theoretical (Fourcaud-Trocmé et al., 2003) and experimental works (Linaro et al., 2018; Testa-Silva et al., 2014), to the rapidity of APs at their onset. Thus neurons with fast AP onset dynamic keep track of the most rapid spectral components in the input signals, as demonstrated for L2/3 and L5 pyramidal cells (see also Goriounova et al., 2018). However, when we examined the correlation between AP rapidity and *cutoff* frequency in L1 interneurons, we failed to confirm the previous reports. In fact, correlations were not significant ($\rho = 0.13, p = 0.32$).

As we repeated the analysis *in silico* for all L1 model neurons available, we also observed a lack of significant correlations as in the experiments ($\rho = 0.15, p = 0.22$; $\rho = 0.08, p = 0.32$; $\rho = 0.16, p = 0.20$; at firing rates of 3, 5 and 7 *spike/s*, respectively). Moreover, no clear separation of AP rapidity at onset was found across the electrical classes of the model cells. Even when the impact of some morphological features were considered (as in Eyal et al., 2014; Goriounova et al., 2018), we found no significant correlations between the AP onset rapidity and total dendritic length of the model cells, over a broad range of total dendritic lengths 500–5400 μm ($\rho = 0.11, p = 0.38$; $\rho = 0.10, p = 0.40$; $\rho = 0.11, p = 0.35$; at firing rates of 3, 5 and 7 *spike/s*, respectively). However, unexpectedly we found slightly significantly negative correlations between the total dendritic length

and the *cutoff* frequency ($\rho = -0.3, p = 0.011$; $\rho = -0.31, p = 0.011$; $\rho = -0.20, p = 0.10$; at a firing rates of 3, 5 and 7 *spike/s*, respectively).

As the last result was neither anticipated in simulation studies (Eyal et al., 2014) nor matched others' experimental reports, we further characterised *in vitro* and *in silico* the AP initiation, employing the *dynamic IV curve* (Badel et al., 2008a, 2008b). This allowed us to extract an additional quantitative parameter for AP initiation, known as the slope factor Δ_T (see the Methods). Across all our experiments, Δ_T took values smaller than 2.5 *mV* (1.51 ± 0.73 *mV*), a range that was confirmed and replicated *in silico*, consistently with the larger spike *sharpness* of interneurons compared to pyramidal cells (Badel et al., 2008a)

While Δ_T and the AP onset rapidity showed correlations *in silico* ($\rho = -0.26, p = 0.03$ at 5 *spike/s*), their values *in vitro* had no significant correlation ($\rho = -0.11, p = 0.37$). Importantly, as the values of Δ_T and the *cutoff* frequency were compared across cells, a significant correlation was finally observed in our experimental data ($\rho = -0.31, p = 0.012$), but not *in silico* ($\rho = -0.06, p = 0.6$ at 5 *spike/s*).

5.5.5 Transfer at high spectral frequencies

For high spectral frequencies f (i.e. above the *cutoff*), the dynamical transfer function is known to decay as $f^{-\alpha}$ (Köndgen et al., 2008), where the numerical value of the exponent has been linked to the precise dynamics of AP initiation at threshold (Fourcaud-Trocmé et al., 2003). In comparison with standard simplified models of excitability, such as the Integrate-and-Fire units (Tuckwell, 1988), previous results in pyramidal neurons (i.e. $\alpha \in [1; 1.5]$) consistently pointed towards an *exponential* or *polynomial* dependency of the AP initiation on the membrane potential (Köndgen et al., 2008; Linaro et al., 2018). Unexpectedly, as we analysed the transfer properties of L1 neuron at high spectral frequencies, we found values of α in the range from 0 to 1.4, with the largest majority (i.e. 94%) smaller than 1 (0.57 ± 0.26) (Figure 5.5a). The distribution of α across different electrical cell types displayed largely overlapping features (Figure 5.5a) with no significant differences, thus hinting at similar transfer behaviours.

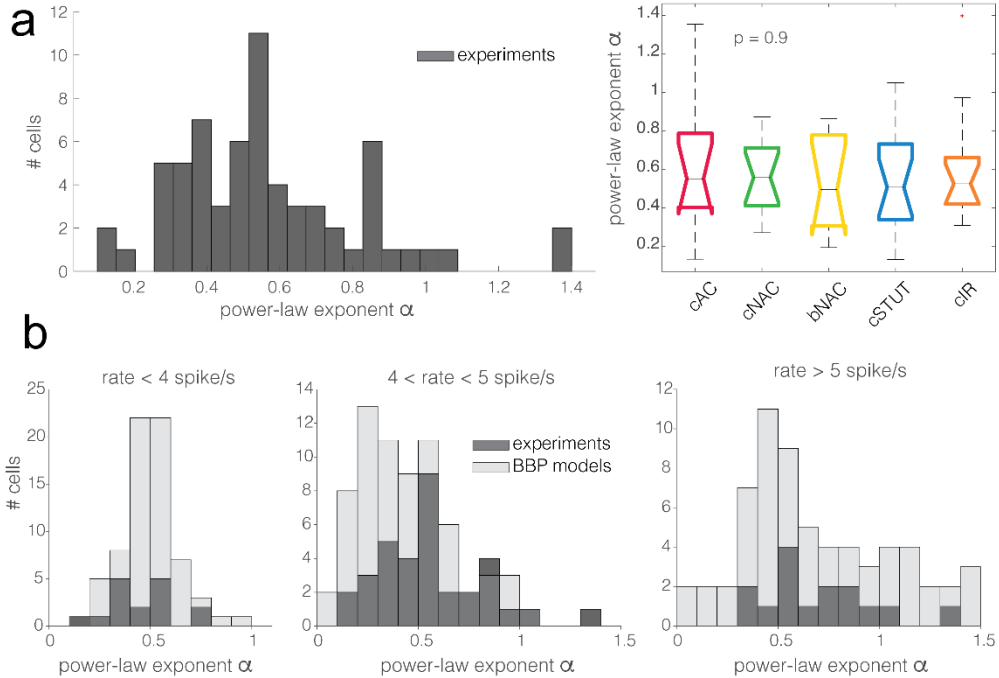


Figure 5.5. The distribution of the power-law exponent at high spectral frequencies. Almost all the cells recorded in this work had a power-law exponent lower than 1, for high spectral frequencies (a). Concerning the cell subtypes, as for Figure 5.3b the Kruskal-Wallis statistical test failed to reject at 1% significance level the null hypothesis that the cutoff frequencies come from the same distribution (b). The same trend was quantitatively confirmed *in silico*, for the BBP models (c). Numerical simulations and experimental data were compared over three distinct ranges of experimental firing rates, where models were set to fire at precisely: 3, 5, and 7 *spike/s* (c, from left to right). The histogram overlay displays the model predictions of the horizontal span of cutoff frequencies, over the three distinct firing rates.

These observations were confirmed *in silico*, where L1 interneuron models were characterised by α in the range 0.2 – 1.5, with the majority below 1 (0.51 ± 0.14 , 0.44 ± 0.24 , and 0.74 ± 0.43 , at a firing rates of 3, 5 and 7 *spike/s*, respectively), matching the values obtained in the experiments (Figure 5.5b).

5.6 Discussion

In this work, we have examined the dynamical signal transfer properties of L1 cortical interneurons. These cells are likely to play a major role in cortical computation, as they receive several afferents from a variety of brain regions while establishing synapses downstream in several cortical columns. Their function of gating and filtering the output spike trains of pyramidal cells in other layers appears clear, although its careful spectral characterisation remained so far unexplored. When an established protocol (Figure 5.1) was used to quantify the encoding properties of L1 interneurons, a markedly lower bandwidth (Figure 5.2) but a gentler attenuation at high spectral frequencies were observed (Figure 5.5), compared to L2/3 and L5 pyramidal cells. Thus, while rapidly varying frequency component of their inputs can be tracked, i.e. up to 200 – 300 *cycle/s*, the large majority of L1 interneurons possesses much lower *cutoff* values, below 100 *cycle/s*. This might indicate that L1 outputs may be well suited to filter incoming information and relay it to pyramidal cells, especially in the centre of their own bandwidth (Goriounova et al., 2018; Ilin et al., 2013; Linaro et al., 2018), particularly where the phase introduced by the pyramidal cell’s transfer function is minimal (Linaro et al., 2018).

The markedly lower *cutoff* frequencies and smaller power-law attenuation coefficient α in L1 interneurons might therefore indicate their specialisation at keeping track of slower *top-down* input modulations (Jiang et al., 2013; Larkum and Phillips, 2016), compared to *bottom-up* inputs reaching directly pyramidal cells in L2/3 and L5, while attenuating less rapidly the components at higher spectral frequencies. Despite the limited size of our data set, we successfully sampled all the known electrical subtypes of L1 cells and found no significant differences in their spectral responses (Figure 5.3). This finding is backed up by an extensive database of accurate multicompartmental models (Markram et al., 2015) that contains *a priori* an extensive diversity in cell response properties.

Our choice of the *in vitro* protocol and the limited cell viability during long experimental conditions did not allow us a systematic exploration of the modulatory effect of the cell’s mean firing rate on the neuronal bandwidth. Nonetheless, we could establish that a significant correlation exists between the *cutoff* frequency and the cell’s firing rate (Figure 5.4), as anticipated by

the theory (Brunel et al., 2001; Fourcaud-Trocmé et al., 2003) but not previously reported for pyramidal cells (Linaro et al., 2018). This suggests that an increase in the mean firing rate of L1 interneurons can expand their filtering capabilities, perhaps relating to the dendritic compartment of pyramidal cells distinct spectral information during different cortical firing regimes. The simulations also suggest that some neuronal types should be more susceptible for the firing rate modulation, such as cAC, bNAC and cIR types.

As opposed to previous reports in pyramidal cells, when we characterised the AP waveform and its relevance for the tracking of fast input spectral components, we did not observe any correlation with the values of the *cutoff* frequency, both *in vitro* and *in silico*. Therefore we suggest that the emerging mechanisms for spike initiation of L1 interneurons might have some quantitative differences when compared to those of excitatory neurons (Ilin et al., 2013; Linaro et al., 2018). In contrast with other studies (Goriounova et al., 2018), we found a negative correlation between the total dendritic length and the cutoff frequency, *in silico*. This might be a consequence of the smaller dendritic length in L1 models than L5 PCs (i.e. 500 – 5400 μm versus 8000 μm and up to 15000 – 20000 μm), although the values of AP onset speed were in a similar range as for L5 PCs, both in experiments and simulations. No correlation was found between the AP onset speed and total dendritic length in the models. However, as the AP slope factor Δ_T was measured, we found similar values as those obtained for other neocortical types. *In silico* an (expected) negative correlation was found between Δ_T and the AP onset rapidity (Badel et al., 2008a, 2008b), but not *in vitro*. A correlation between Δ_T and the *cutoff* frequency clearly was detected *in vitro*, but not *in silico*. We speculate that such a mismatch between theory and experiments might be a consequence of the reduced repertoire of active membrane mechanism models (i.e. sodium and potassium currents kinetics), which are shared by all BBP cortical model neurons (Markram et al., 2015). While using the same biophysical models for describing all cell types is a convenient strategy for automated parameters constraining (Druckmann et al., 2007), we wonder whether L1 interneurons might be even better described with “custom” kinetic parameters for sodium and potassium currents. In addition, we think that the excitability of L1 interneurons has been investigated partially and in less details when compared to L5

pyramidal cells. The latter have been widely studied as a “reference” cortical neuron by many investigators over the last decades. Lastly, BBP L1 models have been identified automatically while extracting only a limited set of features from the experimental data (e.g. time-to-first AP, width of the AP, AP frequency, etc.) (Druckmann et al., 2008) and wonder whether the use of additional protocols, such as the probing of the dynamical transfer function, might have increased the faithfulness of theory-experiments matching. Taken together, all these results call for further investigation of the AP initiation mechanisms in L1 interneurons, both experimentally and numerically.

Finally, as we characterised the transfer properties at high spectral frequencies, we observed a power-law decay although with unexpectedly low absolute values of the exponent α , both *in vitro* and *in silico*. According to (Fourcaud-Trocmé et al., 2003) different reduced models of excitability are associated to distinct, characteristic values of α . In particular, while the exponential Integrate-and-Fire unit seem to be more appropriate to describe pyramidal cells, the leaky Integrate-and-Fire excitability (i.e. $\alpha = 0.5$) seems closer to explain the data, both *in vitro* (i.e. $\alpha = 0.57$ on average) and *in silico* (i.e. in the range $\alpha = 0.44 - 0.74$). This suggest that L1 interneurons might have indeed distinct spike initiation dynamics, when compared to pyramidal cells.

In conclusion, we believe that our results contribute with timely and relevant observations to the series of efforts, world-wide, to describe and classify the excitable properties of neocortical neurons. The spectral characterisation of the bandwidth of spike initiation thus revealed to be more informative than standard methods to quantify neuronal excitability and the present study extends such characterisation to the population of L1 interneurons.

5.7 Acknowledgements

We thank Mrs. G. Van de Vijver for her valuable technical assistance. Financial support from the European Union's ERASMUS program and Horizon 2020 Framework Program for Research and Innovation, under the Specific Grant Agreement n. 785907 (Human Brain Project SGA2), the Research Foundation - Flanders (grant n. G0F1517N), is kindly acknowledged. Access to high-performance computing was generously provided by the VSC (Flemish Supercomputer Center), funded by the Research Foundation - Flanders (FWO) and the Flemish Government – department EWI. The funders had no role in study design, data collection and analysis, decision to publish, or preparation of the manuscript.

5.8 References

- Arsiero M, Lüscher HR, Lundstrom BN, Giugliano M. 2007. The impact of input fluctuations on the frequency-current relationships of layer 5 pyramidal neurons in the rat medial prefrontal cortex. *J Neurosci* **27**:3274–3284. doi:10.1523/JNEUROSCI.4937-06.2007
- Ascoli GA, Alonso-Nanclares L, Anderson SA, Barrionuevo G, Benavides-Piccione R, Burkhalter A, Buzsáki G, Cauli B, DeFelipe J, Fairén A, Feldmeyer D, Fishell G, Fregnac Y, Freund TF, Gardner D, Gardner EP, Goldberg JH, Helmstaedter M, Hestrin S, Karube F, Kisvárdy ZF, Lambolez B, Lewis DA, Marin O, Markram H, Muñoz A, Packer A, Petersen CCH, Rockland KS, Rossier J, Rudy B, Somogyi P, Staiger JF, Tamas G, Thomson AM, Toledo-Rodriguez M, Wang Y, West DC, Yuste R. 2008. Petilla terminology: Nomenclature of features of GABAergic interneurons of the cerebral cortex. *Nat Rev Neurosci*. doi:10.1038/nrn2402
- Badel L, Lefort S, Brette R, Petersen CCH, Gerstner W, Richardson MJE. 2008a. Dynamic I-V Curves Are Reliable Predictors of Naturalistic Pyramidal-Neuron Voltage Traces. *J Neurophysiol* **99**:656–666. doi:10.1152/jn.01107.2007
- Badel Laurent, Lefort Sandrine, Berger Thomas K, Carl · , Petersen CH, Gerstner W, Richardson Magnus J E, Badel L, Gerstner · W, Berger T K, Lefort S, Petersen · C C H, Richardson M J E. 2008b. Extracting non-linear integrate-and-fire models from experimental data using dynamic I-V curves. *Biol Cybern* **99**:361–370. doi:10.1007/s00422-008-0259-4
- Boucsein C, Tetzlaff T, Meier R, Aertsen A, Naundorf B. 2009. Brief Communications Dynamical Response Properties of Neocortical Neuron Ensembles: Multiplicative versus Additive Noise. doi:10.1523/JNEUROSCI.3424-08.2009
- Brette R, Piwkowska Z, Monier C, Rudolph-Lilith M, Fournier J, Levy M, Frégnac Y, Bal T, Destexhe A. 2008a. High-Resolution Intracellular Recordings Using a Real-Time Computational Model of the Electrode. *Neuron* **59**:379–391. doi:10.1016/j.neuron.2008.06.021
- Brette R, Piwkowska Z, Monier C, Rudolph-Lilith M, Fournier J, Levy M, Frégnac Y, Bal T, Destexhe A. 2008b. High-Resolution Intracellular Recordings Using a Real-Time Computational Model of the Electrode. *Neuron* **59**:379–391. doi:10.1016/j.neuron.2008.06.021

- Brunel N, Chance FS, Fourcaud N, Abbott LF. 2001. Effects of synaptic noise and filtering on the frequency response of spiking neurons. *Phys Rev Lett* **86**:2186–2189. doi:10.1103/PhysRevLett.86.2186
- Carnevale NT, Hines ML. 2006. The NEURON book, The NEURON Book. Cambridge University Press. doi:10.1017/CBO9780511541612
- Couto J, Linaro D, De Schutter E, Giugliano M. 2015. On the Firing Rate Dependency of the Phase Response Curve of Rat Purkinje Neurons In Vitro. *PLOS Comput Biol* **11**:e1004112. doi:10.1371/journal.pcbi.1004112
- Cox DR, Miller HD. 1977. The Theory of Stochastic Processes (Science Paperbacks). Chapman and Hall/CRC.
- D'Souza RD, Burkhalter A. 2017. A laminar organization for selective cortico-cortical communication. *Front Neuroanat* **11**. doi:10.3389/fnana.2017.00071
- Dayan P, Abbott LF. 2005. Theoretical Neuroscience. MIT Press (MA).
- Destexhe A, Rudolph M, Paré D. 2003. The high-conductance state of neocortical neurons in vivo. *Nat Rev Neurosci* **4**:739–751. doi:10.1038/nrn1198
- Druckmann S, Banitt Y, Gidon A, Schürmann F, Markram H, Segev I. 2007. A novel multiple objective optimization framework for constraining conductance-based neuron models by experimental data. *Front Neurosci* **1**:7–18. doi:10.3389/neuro.01.1.1.001.2007
- Druckmann S, Berger TK, Hill S, Schürmann F, Markram H, Segev I. 2008. Evaluating automated parameter constraining procedures of neuron models by experimental and surrogate data. *Biol Cybern* **99**:371–379. doi:10.1007/s00422-008-0269-2
- Eyal G, Mansvelder HD, de Kock CPJ, Segev I. 2014. Dendrites Impact the Encoding Capabilities of the Axon. *J Neurosci* **34**:8063–8071. doi:10.1523/jneurosci.5431-13.2014
- Fourcaud-Trocmé N, Hansel D, van Vreeswijk C, Brunel N. 2003. How spike generation mechanisms determine the neuronal response to fluctuating inputs. *J Neurosci* **23**:11628–11640. doi:23/37/11628 [pii]
- Gentet LJ. 2012. Functional diversity of supragranular GABAergic neurons in the barrel cortex. *Front Neural Circuits*. doi:10.3389/fncir.2012.00052

- Gillespie DT. 1996. Exact numerical simulation of the Ornstein-Uhlenbeck process and its integral. *Phys Rev E - Stat Physics, Plasmas, Fluids, Relat Interdiscip Top* **54**:2084–2091. doi:10.1103/PhysRevE.54.2084
- Goriounova NA, Heyer DB, Wilbers R, Verhoog MB, Giugliano M, Verbist C, Obermayer J, Kerkhofs A, Smeding H, Verberne M, Idema S, Baayen JC, Pieneman AW, de Kock CP, Klein M, Mansvelder HD. 2018. Large and fast human pyramidal neurons associate with intelligence. *Elife* **7**. doi:10.7554/eLife.41714
- Hestrin S, Armstrong WE. 1996. Morphology and physiology of cortical neurons in layer I. *J Neurosci* **16**:5290–5300. doi:10.1523/jneurosci.16-17-05290.1996
- Higgs MH, Spain WJ. 2009. Conditional bursting enhances resonant firing in neocortical layer 2-3 pyramidal neurons. *J Neurosci* **29**:1285–1299. doi:10.1523/JNEUROSCI.3728-08.2009
- Hines ML, Carnevale NT. 2001. NEURON: a tool for neuroscientists. *Neuroscientist* **7**:123–35. doi:10.1177/107385840100700207
- Ilin V, Malyshev A, Wolf F, Volgushev M. 2013. Fast computations in cortical ensembles require rapid initiation of action potentials. *J Neurosci* **33**:2281–2292. doi:10.1523/JNEUROSCI.0771-12.2013
- Jiang X, Wang G, Lee AJ, Stornetta RL, Zhu JJ. 2013. The organization of two new cortical interneuronal circuits. *Nat Neurosci* **16**:210–218. doi:10.1038/nn.3305
- Köndgen H, Geisler C, Fusi S, Wang XJ, Lüscher HR, Giugliano M. 2008. The dynamical response properties of neocortical neurons to temporally modulated noisy inputs in vitro. *Cereb Cortex* **18**:2086–2097. doi:10.1093/cercor/bhm235
- Larkum ME. 2013. The yin and yang of cortical layer 1. *Nat Neurosci*. doi:10.1038/nn.3317
- Larkum ME, Phillips WA. 2016. Does arousal enhance apical amplification and disamplification? *Behav Brain Sci* **39**:e215. doi:10.1017/S0140525X15001867
- Larkum ME, Zhu JJ. 2002. Signaling of Layer 1 and Whisker-Evoked Ca²⁺ and Na⁺ Action Potentials in Distal and Terminal Dendrites of Rat Neocortical Pyramidal Neurons *In Vitro* and *In Vivo*. *J Neurosci* **22**:6991–7005. doi:10.1523/JNEUROSCI.22-16-06991.2002

- Linaro D, Biró I, Giugliano M. 2018. Dynamical response properties of neocortical neurons to conductance-driven time-varying inputs. *Eur J Neurosci* **47**:17–32. doi:10.1111/ejn.13761
- Linaro D, Couto J, Giugliano M. 2015. Real-time electrophysiology: Using closed-loop protocols to probe neuronal dynamics and beyond. *J Vis Exp* **2015**. doi:10.3791/52320
- Linaro D, Couto J, Giugliano M. 2014. Command-line cellular electrophysiology for conventional and real-time closed-loop experiments. *J Neurosci Methods* **230**:5–19. doi:10.1016/j.jneumeth.2014.04.003
- Linaro D, Ocker GK, Doiron B, Giugliano M. 2019. Correlation Transfer by Layer 5 Cortical Neurons Under Recreated Synaptic Inputs In Vitro. *J Neurosci* **39**:7648–7663. doi:10.1523/JNEUROSCI.3169-18.2019
- Markram H, Muller E, Ramaswamy S, Reimann MW, Abdellah M, Sanchez CA, Ailamaki A, Alonso-Nanclares L, Antille N, Arsever S, Kahou GAA, Berger TK, Bilgili A, Buncic N, Chalimourda A, Chindemi G, Courcol JD, Delalondre F, Delattre V, Druckmann S, Dumusc R, Dynes J, Eilemann S, Gal E, Gevaert ME, Ghobril JP, Gidon A, Graham JW, Gupta A, Haenel V, Hay E, Heinis T, Hernando JB, Hines M, Kanari L, Keller D, Kenyon J, Khazen G, Kim Y, King JG, Kisvarday Z, Kumbhar P, Lasserre S, Le Bé JV, Magalhães BRC, Merchán-Pérez A, Meystre J, Morrice BR, Muller J, Muñoz-Céspedes A, Muralidhar S, Muthurasa K, Nachbar D, Newton TH, Nolte M, Ovcharenko A, Palacios J, Pastor L, Perin R, Ranjan R, Riachi I, Rodríguez JR, Riquelme JL, Rössert C, Sfyraakis K, Shi Y, Shillcock JC, Silberberg G, Silva R, Tauheed F, Telefont M, Toledo-Rodriguez M, Tränkler T, Van Geit W, Díaz JV, Walker R, Wang Y, Zaninetta SM, Defelipe J, Hill SL, Segev I, Schürmann F. 2015. Reconstruction and Simulation of Neocortical Microcircuitry. *Cell* **163**:456–492. doi:10.1016/j.cell.2015.09.029
- Marmarelis PZ, Naka KI. 1972. White-noise analysis of a neuron chain: An application of the Wiener theory. *Science (80-)* **175**:1276–1278. doi:10.1126/science.175.4027.1276
- Merino RM, Leon-Pinzon C, Stuehmer W, Moeck M, Staiger JF, Wolf F, Neef A. 2019. Background correlations selectively boost the gamma-sensitivity of cortical GABAergic neurons. *bioRxiv* **5**:2019.12.19.882639. doi:10.1101/2019.12.19.882639

- Muralidhar S, Wang Y, Markram H. 2014. Synaptic and cellular organization of layer 1 of the developing rat somatosensory cortex. *Front Neuroanat* **7**. doi:10.3389/fnana.2013.00052
- Naundorf B, Wolf F, Volgushev M. 2006. Unique features of action potential initiation in cortical neurons. *Nature* **440**:1060–1063. doi:10.1038/nature04610
- Press WH. 2007. Numerical Recipes 3rd Edition: The Art of Scientific Computing. Cambridge University Press.
- Schuman B, Machold RP, Hashikawa Y, Fuzik J, Fishell GJ, Rudy B. 2019. Four unique interneuron populations reside in neocortical layer 1. *J Neurosci* **39**:125–139. doi:10.1523/JNEUROSCI.1613-18.2018
- Tchumatchenko T, Wolf F. 2011. Representation of dynamical stimuli in populations of threshold neurons. *PLoS Comput Biol* **7**:e1002239. doi:10.1371/journal.pcbi.1002239
- Testa-Silva G, Verhoog MB, Linaro D, de Kock CPJ, Baayen JC, Meredith RM, De Zeeuw CI, Giugliano M, Mansvelder HD. 2014. High Bandwidth Synaptic Communication and Frequency Tracking in Human Neocortex. *PLoS Biol* **12**:e1002007. doi:10.1371/journal.pbio.1002007
- Tuckwell H. 1988. Introduction to Theoretical Neurobiology: Volume 2, Nonlinear and Stochastic Theories. Cambridge University Press.
- Wang XJ. 2010. Neurophysiological and computational principles of cortical rhythms in cognition. *Physiol Rev*. doi:10.1152/physrev.00035.2008
- Zhu Y, Zhu JJ. 2004. Rapid Arrival and Integration of Ascending Sensory Information in Layer 1 Nonpyramidal Neurons and Tuft Dendrites of Layer 5 Pyramidal Neurons of the Neocortex. *J Neurosci* **24**:1272–1279. doi:10.1523/JNEUROSCI.4805-03.2004

CHAPTER 6

Conclusion

Some pioneers advanced the field of Neuroscience greatly, names as Hodgkin, Huxley, Lapicque, Markram, and Ramon y Cajal come to mind. However, a large amount of the workings of the brain still needs to be elucidated. In recent years several large-scale, long-term, international research programs have tried to fill this void in knowledge. Among them, we mention BRAIN, an American initiative; the China Brain Project; MINDS, a Japanese project; and the Human Brain Project (HBP), a European initiative. As members of the HBP, we focused our attention on how neurons process information and which parameters influence this property of the neuron.

In **chapter 3** we explored the human brain. We were fortunate to enter in a collaboration with a research group from the *vrije Universiteit Amsterdam*, their research lab is in close proximity to a hospital which puts them in a unique position to be able to study human neurons. They obtained healthy cortical brain tissue that was removed to gain access to the deeper located diseased part of the brain. Once taken to the research lab the neocortical tissue was sliced to be able to perform slice patch clamp recordings and 3D reconstructions of the neurons. From the patch clamp experiments the rise speed of action potentials was determined at several firing frequencies. A reconstruction of the neurons was obtained by inject biocytin in the neurons, using the avidin-biotin-peroxidase method and reconstructing the neurons in the NeuroLucida software. After making sure that the reconstructed neurons were consistent in their morphology, they were handed digitally over to us. These morphological models could be loaded into the NEURON simulator and populated with the “classical HH channels”. We probed the neurons’ ability to process fast varying information by using the *transfer function*, determining a cut off frequency. It’s shown that there is a strong correlation between the AP onset rapidity and the total size of the dendritic tree, as well as a correlation between the cut off frequency and the total dendritic length. Taking into consideration that there is a positive correlation between the total dendritic length and the IQ of the individuals, we can conclude that the cut-off frequency is indeed a good representation for the IQ. Furthermore, the rise speed of APs when increasing the instantaneous firing rating, decreases slower for individuals with a higher IQ. This means that they could keep a high cut off frequency when the instantaneous firing rate is increased, since the AP rising speed is indirectly correlated with the cut off frequency.

Our investigation in how neurons transfer information continued in **chapter 4**. We took a large public repository consisting of reconstructed rat neocortical neurons across all layers. In this chapter we focus ourselves on the excitatory neurons. We start from a theoretical theory first proposed by Brette, this theory attributes the steepness of the onset of APs to the precise location of the AIS with respect to the soma. In this special section, in the axon, APs are initiated and propagate from here throughout the neuron. According to the theory, when the AIS is moved further away from the soma, APs will become steeper at their onset and the threshold for spike generation at the soma will decrease as well. This is mainly due to the size difference between the axon, on one hand, and the somatodendritic compartment, on the other hand, which causes the soma to act as a current sink. Our simulations, with the neuron models from the BBP repository which are both morphologically and biophysically detailed, confirm this theory. Our hypothesis that APs with a faster onset would result in a better transfer of fast varying information still needed to be tested. Making use of the *transfer function* we were able to quantify how well a neuron can transfer fast varying information. The hypothesis we posed at the beginning of our research was confirmed by the simulations. Indeed, the cut-off frequency increases when the AIS is moved further away from the soma. In other words, when APs become steeper at their onset the neuron will be better equipped at transferring fast varying information. Lastly, we wanted to confirm that a higher cut-off frequency indeed has a functional meaning. To prove this we employed, with the help of our collaborators from the Graz University of Technology, network simulations, more specifically using the Liquid State Machine framework. We performed separate network simulations for each unique AIS distance, populating each network with an EIF reduction of the *ball-and-stick* models with a particular AIS distance. After training the network, it was presented with a simple classification task. Indeed, a higher success rate was found when the network consisted of neurons with a greater AIS distance. Thus, confirming that indeed a higher cut off frequency also has a functional meaning.

The first two chapters only considered excitatory neurons. In **chapter 5** we investigated inhibitory neurons from layer 1. This chapter combines experimental results with computational results. When one injects a DC into a neuron the firing pattern displays some unique features. In layer 1 there are

5 of these unique firing types that can be found; cAC, cNAC, bNAC, cSTUT, and cIR. We investigated how these layer 1 neurons would respond to the *transfer function* protocol, since this was never investigated in literature. Furthermore, given the fact that these firing types are well separable, we wondered whether we could cluster neurons according to these types with just their *transfer function*. Experimentally this was done by patch-clamp experiments in slices, first characterizing the neuron with DC current pulses, determining their firing type, and subsequently obtaining the *transfer function*. Computationally, we took layer 1 interneurons from the BBP database, the same repository used in chapter 3, and obtained the *transfer function*. Characterizing these neurons wasn't necessary since their firing type is defined a priori. These layer 1 interneurons unexpectedly had a much lower cut-off frequency than the layer 5 excitatory neurons, which can be seen in both *in vitro* and *in silico* results. This means that layer 1 neurons cannot process fast-varying information as well as their excitatory layer 5 counterparts. Furthermore, no clear separation could be found in the cut-off frequencies as the firing type was considered. However, simulation showed that some firing types are more susceptible to a change in mean firing rate. For example, cAC, bNAC, and cIR neurons increased their cut off frequency the most when they're firing at a higher frequency. Lastly, the *transfer function* for layer 1 neurons decays slower at high frequencies than layer 5 excitatory neurons, this is characterized by the slope parameter α . It is shown, both *in vitro* and *in silico*, that layer 1 neurons have an α coefficient corresponding to LIF models, while layer 5 excitatory neurons have an α coefficient that corresponds to EIF models. This is a first indication that spike initiation mechanisms might be different for layer 1 interneurons.

In conclusion, throughout this work we have successfully investigated how neurons process information and what influences their ability to do so. We used a novel method to investigate and characterize neurons, the *transfer function*, which stands closer to the biological input neurons would experience *in vivo*. It is clear, from our work, that by using this method new, biologically relevant behaviour of neurons can be found, see chapter 5 where we find a different spike initiation mechanism for layer 1 interneurons. Furthermore, this work shows that there is a need for a more biophysical way of probing neurons, rather than using DC pulses which have been the golden standard for electrophysiology for so long. Future work could focus on the

BBP repository and the use of their single cell models to further improve these models. As we can see from our work in chapter 5, where *in vitro* work is compared with *in silico* work using these models, some disagreement was found, suggesting lower accuracy of these layer 1 interneurons. When we go back to chapter 3, it would be valuable to investigate a wider diversity in cell types, across different layers, to see if the differences found across layers, in chapter 4 and 5, are also present in the human brain. This could revolutionize the way we look at network simulations.

CHAPTER 7

Scientific curriculum vitae

Christophe Verbist

Contact info: christophe.verbist@outlook.be

Education

09/2016 – 09/2020: PhD in Neuroscience

Lab for Molecular, Cellular and Network Excitability, University of Antwerp

Thesis Title: Dynamics of neuronal responses in silico and in vitro

09/2013 – 06/2016: Master Fysica

Graduation: Distinction

University of Antwerp

Thesis title: Study of CZTSe solar cell with an electron microscope

09/2010 – 06/2014: Bachelor Fysica

Graduation: Distinction

University of Antwerp

Thesis titles:

- Dichtheidsfluctuaties in een Bose-Einsteincondensaat van fotonen
- CIGS zonnecellen

Publications

High-bandwidth information transfer in reduced multi-compartmental model neurons

Verbist C., Salvadè S., Giugliano M.

Poster presentation: 12th congress of the Belgian society for neuroscience 2017, Ghent, Belgium. Abstract published in Front. Neurosci.

DOI: 10.3389/conf.fnins.2017.94.00082

The site of initiation of action potentials in the axon determines the maximal information transfer bandwidth in cortical neurons in silico

Salvadè S., **Verbist C.**, Giugliano M.

Poster presentation: 12th congress of the Belgian society for neuroscience 2017, Ghent, Belgium. Abstract published in Front. Neurosci.

DOI: 10.3389/conf.fnins.2017.94.00096

The dynamical response properties of in silico neurons from the Blue Brain Project digitally reconstructed neocortical microcircuitry

Verbist C., Salvadè S., Giugliano M.

Poster presentation: CNS 2017, Antwerpen, Belgium.

Abstract published in BMC Neuroscience as 26th Annual Computational Neuroscience Meeting (CNS*2017): Part 2.

DOI: 10.1186/s12868-017-0371-2

The Dynamical Response Properties of Cortical Neurons in Silico

Verbist C., Giugliano M.

Poster presentation: 1st human brain project student conference 2018, Vienna, Austria.

Abstract published in Frontiers as Book of abstracts: 1st HBP Student Conference.

DOI: 10.3389/978-2-88945-421-1

Large and fast human pyramidal neurons associate with intelligence

Goriounova N.A., Heyer D.B., Wilbers R., Verhoog M.B., Giugliano M., **Verbist C.**, Obermayer J., Kerkhofs A., Smeding H., Verberne M., Idema S., Baayen J.C., Pieneman A.W., de Kock C.P.J., Klein M., Mansvelder H.D.

eLife, 2018 Dec

DOI: 10.7554/eLife.41714

Homogeneous and narrow bandwidth of spike initiation in rat L1 cortical interneurons

Borda Bossana S., **Verbist C.**, Giugliano M.

Front. Cell. Neurosci. - Cellular Neurophysiology, 2020 May

DOI: 10.3389/fncel.2020.00118

The location of the axon initial segment affects the bandwidth of spike initiation dynamics

Verbist C., Müller M.G., Mansvelder H., Legenstein R., Giugliano M.

PLoS Computational Biology, 2020 July

DOI: 10.1371/journal.pcbi.1008087

CHAPTER 8

Acknowledgments

So here we are, at the end, not only of this work but also of the four years that comprised my PhD. When I started at university I would never have thought I'd end up here. It was a tough four years, with highs, lows and plateaus, but in the end I am happy that I took on this journey. It gave me the opportunity to learn a lot in a whole range of fields, not only scientific but also some real life trades. While this part maybe mandatory the thank you's here are from the hearth and without the help of everyone mentioned here this wouldn't have been possible.

First of all I would like to thank the people in the lab, the people who welcomed me with open arms on that first day, which I still remember like it was yesterday. Thank you to Gerda, Pat, Paz, Sebastiaan, Ellen, Mike, Anastasiya for not only that first day but for the whole four years of support. Gerda who was there almost every day, while she may not have assisted me on a scientific front she did on a mental level, keeping me sane during those four years. Pat and Paz, the dynamic duo, that was always there to help you not only on an administrative level but also on a psychological level. Ellen, the master student of the first hour, we had many laughs and moments I will never forget. I am happy you found your way in the UK with your own PhD. Mike, for all the helpful (non-)technical discussion that always led to new ideas and strides of progress. Anastasiya, who was always there to help you with the science or to gossip. You never had a dull conversation when Anastasiya was there. Sebastiaan was probably the most fundamental part of the lab, always at the ready to help and assist everyone with, and I would never say this to his face, his expertise in so many fields. I have the utmost respect for the coding abilities he developed as a biochemist. But most of all I am proud to call him my friend, all our trips and vacations together are fond memories I will never forget and I can't wait to plan the next one.

Of course those aren't all the people that contributed to me being able to finish this work. Along the way there were some interesting stops. Stefano S., who started his master thesis at the same time as I started my PhD, thank you for all the help and interesting discussions in starting both our projects. Sara, Kawtar, Meriam, Ish, Samuel, Robin, Alessio, thank you for all the good times in the short time that you were present in the lab. Antonella, the only other physicist in a sea of biologists, the beautiful light in the darkness. If Ellen was the master student of the first hour, then Stefano B.B. was the

master student of the last hour. In a few months' time we became very good friends, thank you for an unforgettable time both here in Belgium and in Italy. I'm looking forward to your PhD defence, reserve me a seat because I will be there.

This work would never have been possible without my promotor Prof. Michele Giugliano. I am forever grateful for the opportunity he gave me. Also thank you to my last minute co-promoter Prof. Alain Labro, thank you for helping me in those last moments. I would also like to thank all the members of the jury, who's comments undoubtedly made this work much better.

Of course there are numerous friends that made life that much easier by providing some time to clear my head. Whether it was through mountainbiking, boardgames or just some drinks and talking, it all kept me sane and functioning these four years. I hope there are many more mtb trips, boardgame evenings (nights) and drinks in the future.

An integral part of the puzzle is family and I couldn't be more thankful to them for all their support. Especially to my parents who made this possible by putting their own needs aside and putting my dreams first. It is a debt I can never repay, I will be forever thankful, it is the true definition of family.

There is a final piece of the puzzle that has been added not too long ago. So if you complete me, when I am with you there is no room for sadness, only happiness. Thank you for putting up with my grumpiness that was inevitable at the end of my PhD. Also thank you for correcting my English and putting comma's everywhere they should be. Here's to a long and happy life together, you know, we'll see.

To all the people I mentioned, and those that I forgot (my apologies), one last big thank you from the bottom of my hearth